Study of rectangular pulses in Er : Yb co-doped fiber laser

Meriem Kemel

THESE DE DOCTORAT DE

L'UNIVERSITE D'ANGERS
COMUE UNIVERSITE BRETAGNE LOIRE

ECOLE DOCTORALE N° 596
Matière Molécules et Matériaux
Spécialité : *Physique*

Par
« Meriem KEMEL »

« Study of rectangular pulses in Er :Yb co-doped fiber laser »

Thèse présentée et soutenue à « Angers », le « 05/09/2023 »
Unité de recherche : LphiA-EA 4464
Thèse N° : 10

Rapporteurs avant soutenance :

Philippe Grelu Professeur, Université de Bourgogne
Ammar Hideur Professeur, Université de Rouen Normandie

Composition du Jury :

Stéphane Chaussedent Professeur, Université d'Angers
Philippe Grelu Professeur, Université de Bourgogne
Ammar Hideur Professeur, Université de Rouen Normandie
Mathieu Laroche MCF HDR , ENSICAEN
François Sanchez Professeur, Université d'Angers
Directeur de thèse
Mohamed Salhi MCF, Université d'Angers
Co-encadrant de thèse

Contents

1 Introduction **1**

1.1 A brief history of fiber lasers 1

1.2 Thesis Motivation 2

1.3 Thesis outline 3

2 Basics of fiber optics **5**

2.1 Optical fibers 5

2.1.1 Key characteristics of optical fibers 5

2.1.2 Fiber losses 7

2.1.3 Chromatic dispersion 7

2.1.4 Fiber nonlinearities 9

2.2 Light propagation in fibers 10

2.2.1 Maxwell's equations 10

2.2.2 Wave equation 11

2.2.3 Fiber modes 12

2.3 Er-Yb co-doped fiber amplifier 13

2.4 Mode-locking 14

2.5 Conclusion 16

3 Dissipative soliton resonance in passively mode-locked fiber lasers **17**

3.1 Dissipative soliton resonance 18

3.2 Review of recent experimental results 20

3.2.1 Dual-pump figure-of-eight laser-based DSR pulses . . . 21

3.2.2 Multi-pulsing instabilities 29
3.3 Rectangular pulses in a ring laser cavity based on NPE mode-locking mechanism 32
3.3.1 Experimental setup: all-fibered ring laser cavity 32
3.3.2 Single-mode fiber-based laser cavity 33
3.3.3 Dispersion-shifted fiber-based laser cavity 36
3.3.4 Spectrum optimization 38
3.3.5 Conclusion 41
3.4 Conclusion 42

4 Coherence characterization of nanosecond rectangular pulses using Mach-Zehnder interferometer 44
4.1 Principle of Mach-Zehnder Interferometer 45
4.1.1 Interference of light 46
4.1.2 Quasi-monochromatic interference 47
4.1.3 Mach-Zender interferometer 47
4.2 Coherence characterization with an All-fibered Mach-Zehnder interferometer 48
4.2.1 All-fibered Mach-Zehnder interferometer setup 48
4.2.2 Validation of MZI with DFB semiconductor laser 49
4.2.3 Direct modulation of the DFB semiconductor laser . . . 51
4.2.4 Coherence characterization of rectangular pulses 55
4.2.5 Conclusion 61
4.3 Coherence characterization with an MZI including free space collimators 61
4.3.1 Experimental setup 61
4.3.2 Coherence measurement of rectangular pulses with MZI 62
4.3.3 Conclusion 64
4.4 Conclusion 65

5 Multi-wavelength composite-state soliton generation in double-clad Er:Yb co-doped fiber laser 67

5.1 Experimental setup 69
5.2 Build-up of triple lobe spectrum 69
5.3 Intracavity linear loss effect 71
5.4 Pump power effect 73
5.5 Wavelength-resolved measurement 76
5.6 Harmonic generation 78
5.7 Conclusion 80

6 Polarization-color domain wall in fiber ring laser cavity 81
6.1 Experimental setup 83
6.2 Dual-Wavelength generation regime 84
6.3 Wavelength-resolved measurement 86
6.4 Polarization-resolved measurement 88
6.5 Conclusion 89

7 Conclusion 92

Appendices 95

A Effect of the group-velocity dispersion on nanosecond rectangular pulses 96
A.1 GVD effect on DSR-like rectangular pulses using 30 km of SMF 97
A.1.1 Experimental results 97
A.1.2 Simulation results: 99
A.1.3 Broadening factor 104
A.2 GVD effect on DSR-like rectangular pulses using 60 km of SMF 106
A.2.1 Experimental setup 106
A.2.2 Experimental results 107
A.2.3 Simulation results 111
A.3 Conclusion 113

Abbreviation list

EDFA . . . . . Erbium-Doped Fiber Amplifier

Er:Yb . . . . . Erbium:Ytterbium

DSR . . . . . Dissipative Soliton Resonance

MZI . . . . . Mach-Zehnder Interferometer

DCF . . . . . Double-clad Fiber

SMF . . . . . Single-Mode Fiber

MMF . . . . . Multi-Mode Fiber

FWM . . . . . Four-Wave Mixing

GVD . . . . . Group Velocity Dispersion

PDW . . . . . Polarization Domain Wall

CDW . . . . . Color (wavelength) Domain Wall

SPM . . . . . Self-Phase Modulation

XPM . . . . . Cross-Phase Modulation

SRS . . . . . Stimulated Raman Scattering

SBS . . . . . Stimulated Brillouin Scattering

SA . . . . . Saturable Absorber

SESAM . . . . . Semiconductor Saturable Absorber Mirror

NPE . . . . . Nonlinear Polarization Evolution

NALM . . . . . Nonlinear Amplified Loop Mirror

NOLM . . . . . Nonlinear Optical Loop Mirror

PC . . . . . Polarization Controller

CPA . . . . . Chirped Pulse Amplification

CGLE . . . . . Complex Ginzburg-Landau Equation

PI-ISO . . . . . Polarization-Insensitive Isolator

PS-ISO . . . . . Polarization-Sensitive Isolator

DSF . . . . . Dispersion Shifted Fiber

OPD . . . . . Optical Path Difference

DFB . . . . . Distributed FeedBack

Chapter 1

Introduction

1.1 A brief history of fiber lasers

The first 'laser', or more specifically 'maser' which is a laser operating in a microwave range, was demonstrated in 1955, by Gordon, Zeiger, and Townes [1]. A few years later, in 1958, Schawlow and Townes extended the principle of the maser to the infrared and optical range of the electromagnetic spectrum thus introducing the concept of the laser [2]. The acronym 'laser' stands for 'light amplification by stimulated emission of radiation'. Compared to other light sources, laser light is nearly monochromatic and highly directional. Moreover, a laser emits light with high brightness and degree of coherence.

In 1960, Maiman has demonstrated the first working laser in doped solid-state material—chromium-doped aluminum oxide (Cr: Al2 O3) – the famous Ruby laser [3]. Since then, various lasers based on rare earth–doped glasses have been demonstrated in the 1960s [4–7], among which the first doped fiber laser (flashlamp-pumped neodymium-doped fiber laser) was experimentally demonstrated by Koester and Snitzer [5]. In 1973, Stone and Burrus reported the first diode laser-pumped Nd-doped fiber laser [8]. Despite all these studies on rare-earth-doped fiber amplifiers and lasers, their potential was only recognized in the late 1980s, after demonstrating a very low threshold fiber amplifier [9, 10]. The message of these publications was particularly well received by the optical communication community which developed the Erbium-doped fiber

amplifiers for fiber communication applications. Thus, the first undersea fiber optic link using an amplifier chain starts to operate in the mid-1990s.

Since then, even if many rare earth dopants have been studied and developed for many applications, erbium, ytterbium, neodymium, and thulium-doped glasses continue to be investigated.

Among their numerous applications, optical fiber amplifiers are used as an amplifier in fiber optic communication systems, where Er-doped optical amplifiers (EDFA) are most commonly used because of their low-loss transmission in optical fibers at wavelengths near 1550 nm. Moreover, the EDFA is used as a preamplifier for increasing the receiver sensitivity, as a signal amplifier in long-distance transmission systems, and as a replacement for repeaters in long-distance undersea fiber optic transmission systems.

Nd-doped optical amplifiers and lasers have been demonstrated for space communication applications and high-power operation. Yb-doped amplifiers are important for high-power applications because high Yb doping without any loss process (such as up-conversion) is feasible for Yb-doped fiber lasers using a large area fiber. These lasers emit near 1000 nm. Er-Yb co-doping has been used to make higher-power amplifiers and lasers emitting near 1550 nm. In this case, the existing Yb ions transfer their energy to Er, allowing for lower concentration and hence reduced concentration quenching which would otherwise happen in high-doped Er fibers.

1.2 Thesis Motivation

In this thesis, I use an Er:Yb co-doped fiber amplifier to explore various rectangular-shaped pulses in a passively mode-locked fiber ring laser cavity. Based on the previous work of my group, I continued to explore the concept of dissipative soliton resonance pulses, whose energy grows indefinitely with increasing pump power. The experimental rectangular pulses seem to fulfill all requirements of the DSR pulses, however, I completed the study by investigating the temporal coherence. Indeed, studying the temporal coherence of

these pulses is crucial in order to differentiate between real DSR and noise-like square pulses which have similar experimental characteristics. For this, I used two different methods: The Mach-Zehnder interferometer (MZI) and the group velocity dispersion (GVD) effect using a long fiber coil (30 km SMF28). With the MZI, I characterized the coherence locally while the GVD effect-based study gives a more global coherence measurement. Note that the GVD effect-based coherence characterization is presented in the appendix and requires further investigation. Nevertheless, the coherence exploration contributed to a better understanding of the DSR-like square pulses in Er:Yb codoped fiber laser. Another study was devoted to multi-wavelength generation characterized by square-shaped temporal profiles. These regimes are associated with color and polarization domain walls.

1.3 Thesis outline

The outline of this manuscript is as follows. Chapter 2 is devoted to the basics of fiber optics. In the first part, I recall the basic concepts such as optical fiber properties, characteristics, and fiber non-linearities. In the second part, I draw a fast picture of pulse propagation in fibers. In the third part, I briefly recall the principle of the Er:Yb co-doped fiber-based amplifier. Finally, I present the nonlinear polarization evolution-based mode-locking, which is used in my experiments.

Chapter 3 is devoted to the dissipative soliton resonance regime. I start by briefly defining this phenomenon based on the first theoretical reports. Then I review the previous work of my group. I finally present my work where I tried to optimize the experimental parameters for more stable DSR-like square pulses.

In chapter 4, I study the temporal coherence of rectangular pulses which are usually considered to be dissipative soliton resonance pulses. As the studied pulses are in the range of a few ns to a few tens of ns, I study their temporal coherence, locally, using the Mach-Zehnder interferometer.

For more investigation of rectangular-shaped pulses in the fiber laser cavity, I study in chapter 5, a multi-wavelength regime that is characterized by three-wavelength lobes and each lobe corresponds to a different temporal pulse. This regime is a color domain regime with triple wavelength operation.

As an extension of the previous chapter, chapter 6 is devoted to the polarization-color domain wall regime. Indeed, we show that the regime is a color domain such as in the double wavelength operation regime, each wavelength corresponds to a different temporal profile. Moreover, this same regime is the polarization domain wall as each wavelength is characterized by a different polarization state. Chapter 7 concludes the results of the thesis work.

Additionally to the coherence characterization of rectangular pulses performed in chapter 4, I attempt to study the coherence in a more global way, based on the group velocity dispersion effect. The dispersive medium consists of a 30 km single-mode fiber coil. The results are presented in the appendix A.

Chapter 2

Basics of fiber optics

2.1 Optical fibers

Although the properties of optical fibers as optical waveguides have been known since the 19th century, the field of fiber optics was born only in the 1950s with the introduction of the cladding layer. Since then, the field of fiber optics has been actively developing and drastically improved since 1979, when the losses have been reduced from more than 1000 dB/km to 0.2 dB/km at 1.55 μm. The latter loss value is essentially due to the Rayleigh scattering phenomenon. In this section, I briefly recall fiber characteristics and nonlinearities.

2.1.1 Key characteristics of optical fibers

The most basic form of an optical fiber is a step-index fiber which consists of a central core with a refractive index n_1 and an outer cladding with a slightly lower index n_2 compared to n_1, (see figure 2.1). The guiding effect in optical fiber results from total internal reflection induced by the core-cladding index difference, (see figure 2.2). The relative core-cladding index difference is defined as:

$$\Delta = \frac{n_1 - n_2}{n_1} \tag{2.1}$$

The total internal reflection (thus the guiding of the light) occurs when the incidence angle α which is measured against the normal direction on the core-

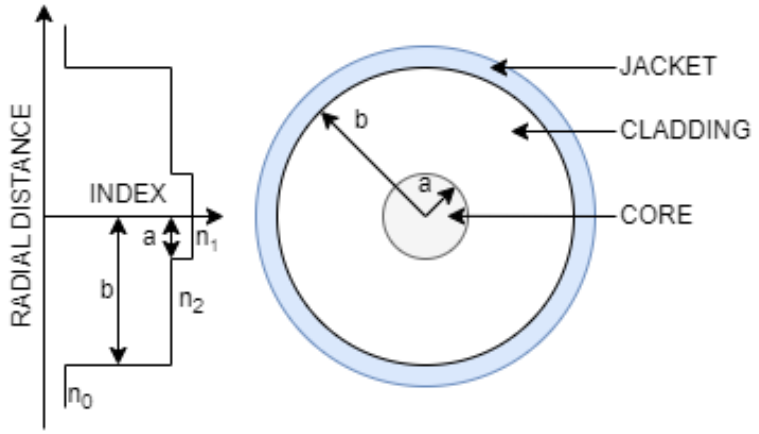

Figure 2.1: Illustration of the optical fiber cross-section and the refractive index change along the radial distance

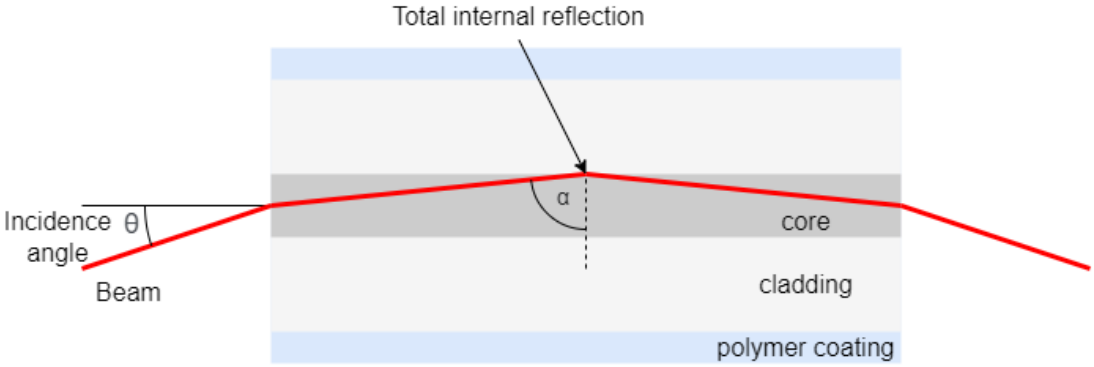

Figure 2.2: Guidance of a light beam in a step-index optical fiber via total internal reflection at the core-cladding interface.

cladding interface, is large enough. For this criterion to be satisfied, the incidence angle θ of the beam (hitting the fiber core from the outside) has to be lower than a certain maximum. That maximum value is the sine of the so-called numerical aperture (NA) defined as:

$$NA = \sqrt{n_1^2 - n_2^2} \tag{2.2}$$

Another important parameter of the optical fiber is the so-called V-parameter:

$$V = k_0 a \sqrt{n_1^2 - n_2^2}, \tag{2.3}$$

where $k_0 = 2\pi/\lambda$, a is a core radius, and λ is wavelength. The V-parameter (also called V-number) determines the number of modes allowed in the fiber.

Depending on the size of the fiber core, it can support only one mode or many modes. For example, the step-index fiber supports one mode if $V < 2.405$. Thus, it is called single-mode fiber (SMF). In contrast, when $V > 2.405$, the fiber supports several modes and it is called multi-mode fiber (MMF). The typical core radius of SMF is about 5 μm, while it is about $25 - 30$ μm for MMF.

2.1.2 Fiber losses

During its propagation inside the fiber, the optical signal experiences a power loss. The attenuation constant α of an optical fiber estimates how much the input power P_0 is attenuated when passing through an optical fiber of length L according to the formula:

$$P_T = P_0 exp(-\alpha L), \tag{2.4}$$

where P_T is the transmitted power at the other end of the fiber. The attenuation constant α measures the entire fiber losses of all sources, such as material absorption, fiber impurities which can lead to significant absorption, Rayleigh scattering which is an intrinsic loss, bending of the fiber, scattering of light at the core-cladding interface, and splice and cabling. The fiber losses α are usually expressed in units of dB/km using the formula:

$$\alpha_{dB} = -\frac{10}{L} \log\left(\frac{P_T}{P_0}\right) = 4.343\alpha \tag{2.5}$$

Fiber losses are wavelength-dependent. In the case of silica fibers, according to the measured loss spectrum of an SMF, the losses are about 0.2 dB/km at 1.55 μm and are mainly resulting from Rayleigh scattering.

2.1.3 Chromatic dispersion

When a lightwave interacts with bound electrons of a dielectric (for example fused silica fiber), the response of the latter depends on the wavelength. This property is called chromatic dispersion and manifests by means of frequency

dependence of the refractive index $n(\omega)$. Thus, chromatic dispersion plays a crucial role in the propagation of short pulses as different wavelengths propagate at different speeds $c/n(\omega)$.

The fiber dispersion can be expressed by expanding the mode-propagation constant β in a Taylor series about the central frequency ω_0:

$$\beta(\omega) = n(\omega)\frac{\omega}{c} = \beta_0 + \beta_1(\omega - \omega_0) + \frac{1}{2}\beta_2(\omega - \omega_0)^2 + \dots \tag{2.6}$$

The parameters β_1 and β_2 are related to the refractive index n through the formulas:

$$\beta_1 = \frac{1}{v_g} = \frac{n_g}{c} = \frac{1}{c}\left(n + \omega\frac{dn}{d\omega}\right) \tag{2.7}$$

$$\beta_2 = \frac{1}{c}\left(2\frac{dn}{d\omega} + \omega\frac{d^2n}{d\omega^2}\right) \tag{2.8}$$

where n_g and v_g are the group index and the group velocity, respectively. Note that in the case of waveguides such as optical fibers, one uses the so-called effective refractive index (n_{eff}) rather than the ordinary refractive index, since the dispersion of the waveguide has to be taken into account. The effective refractive index depends not only on the wavelength but also on the propagation mode. The group velocity represents the pulse envelope velocity while traveling in the medium. The parameter β_2 represents the dispersion of the group velocity. It is responsible for the pulse broadening through the phenomenon of the group velocity dispersion (GVD) and β_2 is referred to as the GVD parameter. Instead of β_2 it is common to use the dispersion parameter D related by:

$$D = \frac{d\beta_1}{d\lambda} = -\frac{2\pi c}{\lambda^2}\beta_2 \tag{2.9}$$

The GVD parameter can be negative or positive. Indeed, there exists a wavelength for which $\beta_2 = 0$, and this wavelength is referred to as the zero-dispersion wavelength, noted λ_D. In fused silica, $\lambda_D \approx 1.27\mu m$. For wavelengths such that $\lambda < \lambda_D$, the GVD parameter $\beta_2 > 0$, so the fiber is said to exhibit normal dispersion. In contrast, for $\lambda > \lambda_D$, the GVD parameter $\beta_2 < 0$, so the fiber is said to exhibit anomalous dispersion. In the nonlinear regime, the combination of nonlinearity and dispersion in the fiber can lead to different nonlinear effects, and the sign of the GVD plays an important role.

2.1.4 Fiber nonlinearities

In linear optics, the polarization of the material (dipole moment per unit volume) is linearly proportional to the applied electric field $\mathbf{E}(t)$:

$$\mathbf{P}(t) = \epsilon_o \chi^{(1)} \mathbf{E}(t) \tag{2.10}$$

where $\chi^{(1)}$ is linear susceptibility and ϵ_o is the permittivity of free space. The effect of linear susceptibility $\chi^{(1)}$ manifests through the refractive index n and the attenuation constant α. However, the response of optical fibers (or any dielectric medium) to light becomes nonlinear under an intense electromagnetic field as the latter causes an anharmonic motion of bound electrons in the medium. In this case, the total polarization becomes nonlinear and satisfies the more general relation:

$$\mathbf{P}(t) = \epsilon_o[\chi^{(1)}\mathbf{E}(t) + \chi^{(2)}\mathbf{E}^2(t) + \chi^{(3)}\mathbf{E}^3(t) + \ldots] = \mathbf{P}^{(1)}(t) + \mathbf{P}^{(2)}(t) + \mathbf{P}^{(3)}(t) + \ldots \tag{2.11}$$

where $\chi^{(2)}$ and $\chi^{(3)}$ are second- and third-order susceptibility, respectively. In the case of silica optical fibers, as the silica molecule is symmetrical, the second-order susceptibility $\chi^{(2)} = 0$. However in case of imperfections, and lack of symmetry, $\chi^{(2)} \neq 0$, and can be responsible for nonlinear effects such as second-harmonic generation and sum frequency generation. The third-order susceptibility is responsible for other nonlinear effects in optical fibers like nonlinear refraction, third-harmonic generation (THG), and four-wave mixing (FWM). Nonlinear effects from nonlinear refraction are anyway more likely to manifest rather than THG and FWM.

Nonlinear refraction is the phenomenon that refers to the intensity dependence of the refractive index, as expressed through the relation:

$$\tilde{n}(\omega, I) = n(\omega) + n_2 I \tag{2.12}$$

where $n(\omega)$ is a constant part of the refractive index, I is optical intensity in the fiber and $n_2 = \frac{3}{8n} Re(\chi^{(3)})$ is the nonlinear-index coefficient.
Nonlinear refraction causes numerous nonlinear effects such as self-phase modulation (SPM) and cross-phase modulation (XPM). Self-phase modulation is a

self-induced phase shift of the optical field while propagating in optical fiber. SPM induces, for example, spectral broadening of ultrashort pulses, and the generation of solitons in a laser cavity with an anomalous dispersion regime. Cross-phase modulation is a nonlinear phase shift of an optical field induced by another field with a different wavelength, direction, or polarization state. XPM causes for example asymmetric spectral broadening of copropagating pulses.

There exist other nonlinear effects resulting from stimulated inelastic scattering in which the lightwave transfers part of its energy to the medium. The most important of such effects in the silica fibers are stimulated Raman scattering (SRS) and stimulated Brillouin scattering (SBS). The SRS manifests through vibrations of optical phonons of the crystal lattice of the silica, while the SBS manifests through vibrations of acoustic phonons.

Finally, silica fiber provides a variety of nonlinear effects at low power levels, despite the intrinsically small values of their nonlinear coefficients. For example, the nonlinear index coefficient n_2 is in the range of $2.2 - 3.4 \times 10^{-20}\ m^2/W$ which is relatively small compared to other nonlinear media.

2.2 Light propagation in fibers

2.2.1 Maxwell's equations

The propagation of light in optical fiber is governed by Maxwell's equations:

$$\vec{\nabla} \times \vec{H} = \vec{j} + \frac{\partial \vec{D}}{\partial t} \tag{2.13}$$

$$\vec{\nabla} \times \vec{E} = -\frac{\partial \vec{B}}{\partial t} \tag{2.14}$$

$$\vec{\nabla} \cdot \vec{B} = 0 \tag{2.15}$$

$$\vec{\nabla} \cdot \vec{D} = \rho \tag{2.16}$$

where $\vec{E}$ and $\vec{H}$ are electric and magnetic field, $\vec{D} = \epsilon_0 \vec{E} + \vec{P}$ is dielectric flux, $\vec{B} = \mu_0 \vec{H} + \vec{M}$ is the magnetic flux, ρ is the free charge density and $\vec{j}$ is density of free carries. $\vec{P}$ is polarization, $\vec{M}$ is magnetization, ϵ_0 is vacuum permittivity and μ_0 is the vacuum permeability.

The first equation is Ampere's law, which defines the magnetic field created by a current with density $\vec{j}$ or induced by an alternating electric field. Maxwell's second equation is Faraday's law. It defines the electric field that arises when the magnetic field strength changes. Maxwell's third equation (Gauss' theorem) states that there are no monopole magnetic charges. Maxwell's fourth equation (Poisson's equation) states that there is an electric field around electric charges. This equation is analogous to Coulomb's law.

2.2.2 Wave equation

Wave equation describes light propagation in optical fibers. By taking the curl of both sides of Faraday's Law equation and considering $\nabla \times \nabla \times \vec{E} = \nabla\left(\nabla \cdot \vec{E}\right) - \nabla^2 \vec{E}$, we obtain the wave equation:

$$\left(\Delta - \frac{1}{c_0^2}\frac{\partial^2}{\partial t^2}\right)\vec{E} = \mu_0\left(\frac{\partial \vec{j}}{\partial t} + \frac{\partial^2}{\partial t^2}\vec{P}\right) + \frac{\partial}{\partial t}\vec{\nabla} \times \vec{M} + \vec{\nabla}(\vec{\nabla} \cdot \vec{E}) \tag{2.17}$$

where $c_0 = \sqrt{1/\mu_0\epsilon_0}$ is the speed of light in vacuum. In optical fiber as a dielectric non-magnetic medium, the current density $\vec{j} = \vec{0}$, no free charges $\rho = 0$, and the magnetization $\vec{M} = \vec{0}$. With $\vec{D} = \epsilon(\vec{r})\vec{E} = \epsilon_0\epsilon_r(\vec{r})\vec{E}$ we have $\vec{\nabla} \cdot (\epsilon(\vec{r})\vec{E}) = 0$. Additionally, for a homogeneous medium, $\vec{\nabla} \cdot \vec{E} = 0$, so the wave equation simplifies:

$$\nabla^2 \vec{E} - \frac{1}{c_0^2}\frac{\partial^2 \vec{E}}{\partial t^2} = \mu_0 \frac{\partial^2 \vec{P}}{\partial t^2} \tag{2.18}$$

Thus, the wave equation is driven by the polarization in the medium.
To complete the description, a relation between $\vec{P}$ and $\vec{E}$ is necessary. If only the third-order nonlinear effects governed by $\chi^{(3)}$ are included, one can write the induced polarization as:

$$\vec{P}(r,t) = \vec{P}_L(r,t) + \vec{P}_{NL}(r,t) \tag{2.19}$$

Because of the complexity of equation 2.18, it is necessary to use several approximations. One of them is to treat nonlinear polarization contribution $\vec{P}_{NL}$ to be a small perturbation, so $\vec{P}_{NL} = 0$. With additional simplifications

and assumptions, the wave equation in the frequency domain is written:

$$\nabla^2 \vec{E}(\omega) + n^2(\omega)\frac{\omega^2}{c^2}\vec{E}(\omega) = 0 \tag{2.20}$$

where the refractive index is $n(\omega) = 1 + \frac{1}{2}Re[\chi^{(1)}(\omega)]$. In the following part, the wave equation 2.20 is solved to introduce fiber modes.

2.2.3 Fiber modes

Optical fiber supports a finite number of guided modes with spatial distribution $\tilde{E}(r, \omega)$ as a solution that satisfies the wave equation. Due to cylindrical symmetry of fibers, the equation 2.20 is easier to solve in cylindrical coordinates ρ, ϕ, and z:

$$\frac{\partial^2 \tilde{E}(r,\omega)}{\partial \rho^2} + \frac{1}{\rho}\frac{\partial \tilde{E}(r,\omega)}{\partial \rho} + \frac{1}{\phi}\frac{\partial^2 \tilde{E}(r,\omega)}{\partial \phi^2} + \frac{\partial^2 \tilde{E}(r,\omega)}{\partial z^2} + n^2 k_0^2 \tilde{E}(r,\omega) = 0 \tag{2.21}$$

where $k_0 = \frac{\omega}{c} = \frac{2\pi}{\lambda}$, and $\tilde{E}(r, \omega)$ is Fourier transform of $\vec{E}(r, t)$. Using Maxwell's equations, the component $\tilde{E}_z$ is taken as independent and the other components $\tilde{E}_\rho$ and $\tilde{E}_\phi$ are expressed as a function of $\tilde{E}_z$. The reasoning is the same for the magnetic field, but let us focus on the electric field only. Thus, using the method of separation of variables, the wave equation for $\tilde{E}_z$ is solved:

$$\tilde{E}_z(r, \omega) = A(\omega)J_m(\kappa\rho)exp(\pm im\phi)exp(i\beta z) \tag{2.22}$$

where A is a normalization constant, m is an integer, β is propagation constant, J_m is Bessel function, and $\kappa = \sqrt{n_1^2 k_0^2 - \beta^2}$ for $\rho \leq a$. In the cladding region ($\rho > a$), the solution has to be such that it decreases exponentially for large ρ, and the modified Bessel function $K_m(\gamma\rho)$, with parameter $\gamma = \sqrt{\beta^2 - n_2^2 k_0^2}$, represents such a solution.

After applying some boundary conditions, an eigenvalue equation, whose solution provides the propagation constant β for the fiber modes is determined. For each integer value m, there exist several solutions for β. They are noted β_{mn} (m and n are integers) and each eigenvalue β_{mn} corresponds to one specific mode supported by the fiber. There are two types of fiber modes: HE_{mn} and EH_{mn}. A single-mode fiber supports only the HE_{11} mode (fundamental

mode). The rest of the modes are beyond cut-off if the parameter $V < V_c$, with $V_c \approx 2.405$.

2.3 Er-Yb co-doped fiber amplifier

The first Erbium-doped (Er-doped) glass laser was demonstrated in 1965. It operates near the wavelength region of 1550 nm, a wavelength of interest for optical communication applications. However, Erbium-Ytterbium (Er-Yb) co-doped fiber is the most used material for high-power lasers emitting near 1.55 μm. Indeed, for high-power operation, it is needed to use high Erbium concentration in the fiber for high gain. Though, the ion-ion interactions causing pair-induced up-conversion deplete the Er metastable level and lower the efficiency above a certain level of Er concentration. One of the ways to solve this problem is co-doping the Er-doped fiber with Yb which reduces the formation of Er clusters and their consequences. This way, it is possible to have highly Er-doped fibers for high-gain amplifiers.

The Er-Yb co-doped fiber amplifiers usually have a double-clad fiber (DCF) design. The DCF amplifier has a core of 4 to 5 μm diameter for single mode, inner cladding (100 to 400 μm depending on output power), and outer cladding. The pump light propagates in the inner cladding and excites the Ytterbium ions to higher energy levels. Then, the energy transfer from Yb to Er occurs. Finally, the Erbium transition from the upper to lower energy level emits 1550 nm laser.

In figure 2.3 the energy level diagram of the Er-Yb laser is shown. The Yb ion absorbs pumping radiation (1) and releases it through spontaneous emission (2) and non-radiative transfer of the energy to the Er ion (3). The Er ion experiences nonradiative transition (4), lasing radiation absorption (5), and finally produces lasing radiation (6) and spontaneous emission (7) to the ground level.

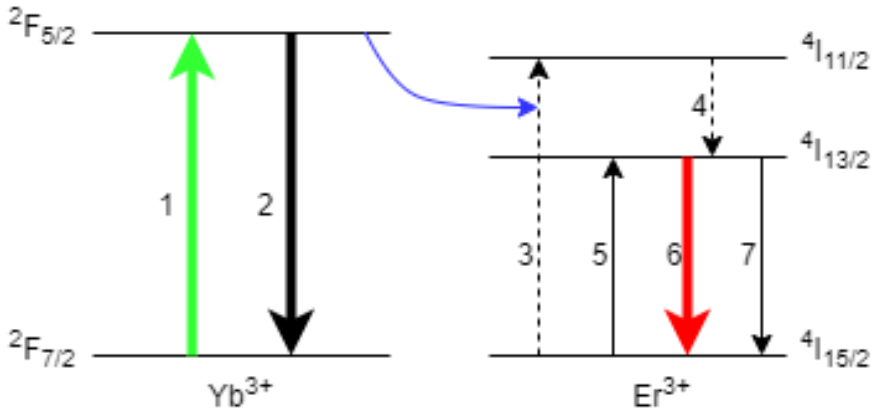

Figure 2.3: Energy level diagram of Er-Yb-doped laser.

2.4 Mode-locking

Mode-locking is a method of producing ultrashort laser pulses. It is achieved by using a specific device in the laser cavity. There exist active and passive mode-locking. The active mode-locking is implemented through a periodic modulation of the cavity losses or of the round-trip phase change, using different devices such as an acousto-optic or electro-optic modulator, Mach-Zehnder integrated-optic modulator, or a semiconductor electroabsorption modulator.

Passive mode-locking allows achieving much shorter pulses (fs range) using saturable absorbers (SA). This occurs because an SA can modulate cavity losses much faster than active mode-locking-based modulators can do. A SA is an optical component with a reduced absorption level at high optical intensities. There exist real and artificial SAs. Real SAs include nanomaterials (such as graphene, transition-metal dichalcogenides, topological insulators, and fullerene), and semiconductor saturable absorber mirrors (SESAMs). The SESAMs are widely used in solid-state and fiber lasers. The so-called artificial SAs exploit the intensity-dependent nonlinear effects to generate mode-locking. The most used are nonlinear optical loop mirrors (NOLM), nonlinear amplifying loop mirrors (NALM), Kerr-lens mode-locking, and nonlinear polarization evolution (NPE). The NPE is used as an artificial saturable absorber in my experiments.

Nonlinear polarization evolution

NPE is a nonlinear (intensity-dependent) change in the polarization state that can occur when a high-intensity optical pulse propagates in a non-polarization-maintaining optical fiber.

To illustrate the process of mode-locking with NPE, let us consider a ring laser cavity as depicted in figure 2.4. Between the two polarization controllers, PC1 and PC2, a polarization-dependent isolator is inserted. Together they act as a mode-locking element.

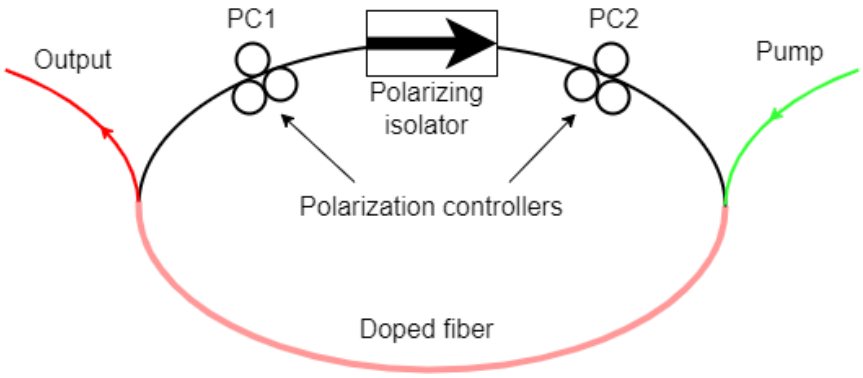

Figure 2.4: Schema of the fiber laser cavity passively mode-locked through nonlinear polarization evolution

Let us consider a linearly polarized pulse right after the isolator. A polarization controller positioned PC2 after the isolator changes the polarization state to elliptical. The polarization state evolves nonlinearly during pulse travel due to SPM- and XPM-induced phase shifts. As the dependence of the phase shift intensity is nonlinear, the polarization state is not uniform along the pulse length. The polarization controller PC1 in front of the isolator is tuned in such a way that it forces the polarization to be linear in the central part of the pulse. This way we achieve the maximum transmission of the polarizer for the biggest optical intensity because the polarization isolator allows the central intense part of the pulse to pass through, but blocks the low-intensity sides of the pulse. As a result, the pulse is shortened after passing one round in the ring cavity - the effect is the same as that created by a fast saturable absorber. As a result, a polarization-dependent isolator, when working in conjunction with a

birefringent fiber, can generate intensity-dependent losses that are essentially identical to those generated by a fast saturable absorber.

2.5 Conclusion

In this chapter, I recalled concisely some basics of fiber optics. I started with the key parameters of optical fibers (mainly single-mode fibers (SMF)) such as fiber losses, chromatic dispersion, and fiber nonlinearities. Then, I presented the pulse propagation in fibers, from Maxwell's equations to fiber modes, passing through the wave equation. After that, I briefly introduced the functioning of Er:Yb co-doped fiber amplifier. Finally, I presented the mode-locking technique based on NPE, the technique of mode-locking that I used in experiments of this thesis work. The next chapter presents the phenomenon of dissipative soliton resonance (DSR).

Chapter 3

Dissipative soliton resonance in passively mode-locked fiber lasers

Over the past decades, the demand for high-energy lasers has steadily increased in various fields such as medicine, defense, security, and industry [11–17]. Until recently, chirped pulse amplification (CPA) [18], which won the Nobel Prize in physics in 2018, was the most common and efficient technique to generate ultrashort high-energy pulses in mode-locked lasers. However, the implementation of this technique requires several amplifiers at the oscillator output. As a step forward, Fernandez et al. reported in 2004 the concept of chirped-pulse oscillators as a new route to high-energy femtosecond pulses in solid-state lasers without external amplification [19]. The principle was to use chirped multilayer mirrors in the oscillator to produce a net positive dispersion over a broad spectral range. Afterward, the output chirped pulses are compressed, using a dispersive delay line at the output of the laser cavity. Also in fiber lasers, the principle of dispersion management and pulse shaping, have been widely investigated in this regard [20–22]. Since then, several alternatives have been proposed, offering a multitude of solutions for more and more compact, efficient, and energetic lasers. In this context, the concept of dissipative soliton resonance (DSR) was introduced by Chang et al. [23]. Based on the cubic-quintic complex Ginzburg-Landau equation (CGLE), they numerically found that for particular values of the system parameters, the energy of the pulses

increases indefinitely. Furthermore, they demonstrated that the DSR regime can exist in normal and anomalous dispersion regimes [24]. Building on these early reports, the generation of high-energy square pulses has been extensively investigated numerically [25–30], and experimentally [31–40], in various configurations of passively mode-locked fiber lasers.

In the experimental literature, rectangular pulses are thought to be DSR pulses when they manifest a certain behavior with the variation of the pump power. It is characterized by a linear increase of the pulse width and energy, a clamped peak power, no wave-breaking, and an invariant optical spectrum. In this chapter, I begin with a brief definition of the so-called dissipative soliton resonance (DSR) based on early theoretical reports on this concept. Then I will present the experimental state of the art by summarizing the previous studies of our group. I will mainly present a laser architecture based on a figure-of-eight laser cavity allowing to reach extremely high energies as well as the multi-pulse DSR operation based on a ring laser cavity. In the last section, I give my experimental results of square pulses based on nonlinear polarization evolution laser cavity by exploiting two different types of fiber, single mode fiber (SMF28), and dispersion-shifted fiber (DSF) coils.

3.1 Dissipative soliton resonance

Dissipative solitons are self-organized and self-localized structures that occur under the condition of continuous energy supply from an external source. The continuous supply of the energy is dissipated in the medium where solitons occur. The energy supplied and lost has to be in a constant balance for the solitons to exist. In [23] Chang et al. showed that for certain values of the system parameters governing the dissipative solitons, the soliton energy can increase indefinitely so the process resembles the resonance phenomenon in the theory of oscillators. Thus, the authors called this concept “dissipative soliton resonance”. In the reference [23], the authors have found an approximate relation between the parameters of the cubic-quintic Ginzburg-Landau equation

(CGLE) where the resonance occurs, by using the method of moments.

Let us consider the occurrence of dissipative soliton resonance (DSR) in the laser cavity as given in [23]. The cubic-quintic Ginzburg-Landau equation (CGLE) is the basic equation for modeling passive mode-locked lasers [23]:

$$i\psi_z + \frac{D}{2}\psi_{tt} + |\psi|^2\psi = -\nu|\psi|^4\psi + i\delta\psi + i\epsilon|\psi|^2\psi + i\beta\psi_{tt} + i\mu|\psi|^4\psi \tag{3.1}$$

Where ψ is normalized field envelope, z is propagation variable and t is time in frame linked with the group velocity of the solution, D is dispersion, δ is linear loss, ϵ is nonlinear gain, μ is nonlinear gain saturation, β correspond to spectral filtering or gain dispersion, and ν is quintic reactive Kerr nonlinearity.

As the CGLE has various localized solutions, and to simplify the problem, the authors have chosen a higher-order Gaussian as a trial function to approximate the stationary localized solution of the CGLE:

$$\psi(t,z) = A.exp(-\frac{t^2}{w^2} - \frac{t^4}{w^4}).exp(ict^2) \tag{3.2}$$

where A is soliton amplitude, w is spectral width and c is a chirp. Using the method of moments for the solution of CGLE, the evolution equations for soliton energy Q, spectral width w, and chirp c were found to be[23]:

$$Q_z = Q\Big(2\delta - \frac{3.738\beta}{w^2} - 1.158c^2w^2\beta + \frac{1.433Q\epsilon}{w} + \frac{1.146Q^2\mu}{w^2}\Big), \tag{3.3}$$

$$w_z = w\Big(2cD + \frac{2.142\beta}{w^2} - 0.874c^2w^2\beta - \frac{0.290Q\epsilon}{w} - \frac{0.325Q^2\mu}{w^2}\Big), \tag{3.4}$$

$$c_z = \frac{1}{w^2}\Big(-2c^2w^2D + \frac{6.453D}{w^2} - \frac{1.237Q}{w} - \frac{1.319Q^2\nu}{w^2} - 19.624c\beta\Big), \tag{3.5}$$

where $Q = 1.051A^2w$.

Near the resonance curve, the energy and spectral width of the gaussian becomes infinite and the chirp tends to zero ($Q \to \infty, w \to \infty, c \to 0$). Also, near the resonance curve, the values Q/w and cw approach to constant with chirp c being negative. Using these properties and the assumption that linear loss is very small, the following expressions are obtained:

$$\frac{Q}{w} = \frac{-1.152\epsilon}{\mu} \tag{3.6}$$

$$cw = -0.336\frac{\epsilon}{\sqrt{-\beta\mu}} \tag{3.7}$$

Then, the analytical expression for the resonance curve is the following:

$$D = \left(\frac{7.778\nu}{\mu} - \frac{6.333}{\epsilon}\right)\beta \tag{3.8}$$

Hence, near the resonance, the soliton increases its width and its energy indefinitely while keeping its amplitude constant. The fact that the pulse width increases while its spectrum does not become narrower come from the fact that the pulses are not transform-limited. While approaching the resonance, the chirp tends to zero, but the Fourier integral is over an ever-widening range. By some analytical calculations, the authors show that these factors compensate, thus, the spectral width tends to be a constant.

To conclude, in [23], the authors have presented a trial function approximation for the dissipative soliton resonance phenomenon and have found an analytic expression of the resonance curve. The latter shows that the resonance occurs in the region of normal dispersion but can be shifted to the region of anomalous dispersion. This observation is confirmed later in the reference [24], where the authors found that in the case of negative quintic reactive nonlinearity ν, the resonance occurs with positive dispersion. Hence, there is a possibility to generate high-energy pulses by lasers that work in the anomalous dispersion regime. Later studies [26] explicitly show that DSR can exist in a wide range of parameters in both normal and anomalous dispersion regimes.

In the reference [27] it is shown that DSR is observable in a real ring laser resonator using nonlinear polarization evolution as a mode-locking mechanism. So the DSR is achievable with realistic laser settings. In the following sections of this chapter, I will consider experimental studies of the DSR-like square pulses.

3.2 Review of recent experimental results

In the following sections, I will present the previous work of our group on DSR pulses. Section 3.2.1 summarizes the experimental results of the DSR regime

based on the figure-of-eight laser cavity where the authors studied the effect of different parameters to optimize the laser cavity and thus the DSR pulses. Section 3.2.2. is a summary of other experimental results on the multi-pulsing of the DSR regime.

3.2.1 Dual-pump figure-of-eight laser-based DSR pulses

Using a passively mode-locked, dual-pump figure-of-eight fiber laser consisting of a nonlinear amplifying loop mirror (NALM) and a nonlinear optical loop mirror (NOLM), Mei et al. demonstrated the generation of square-wave pulses [41] whose width and amplitude can be independently tuned by adjusting the gain of the two loops separately. Indeed, while the amplifier of the NALM is set constant, the gain of the unidirectional loop (NOLM) only affects the peak power by keeping the duration of the pulse constant. Inversely, while the amplifier of the NOLM is turned off, the gain of the NALM loop allows the increase of the pulses' duration without changing the peak power level. To better understand and control the pulse duration and peak power of the rectangular pulses of the DSR regime, our group studied the same cavity studied by Mei et al. [41] by introducing double-clad amplifiers instead of the standard fiber amplifiers in each loop of the figure-of-eight fiber laser. Various cavity parameters, such as the gain of each amplifier alone, the coupling ratio of the two loops, and the fiber dispersion, were examined to study their effect on the square pulses.

(a) Experimental setup of figure-of-eight laser

The figure-of-eight laser cavity configuration is shown in figure 3.1. It consists of a unidirectional ring cavity (UR) connected to a nonlinear amplifying loop mirror (NALM) by a central optical coupler (OC) with a coupling ratio of k. The UR cavity consists of a C-band double-clad 30 dBm Er:Yb co-doped fiber amplifier (A1) containing 2.45 m double-clad fiber with a second-order dispersion $\beta_2 = -0.021\ ps^2/m$; a polarization-insensitive isolator (PI-ISO) to

ensure the unidirectional sense of the light; a coupler with 99% output ratio, and an additional fiber coil L1. A1 emits 1.2 W of output power under 3 W of pump power. The NALM consists of another C-band double-clad 30 dBm Er:Yb co-doped fiber amplifier (A2) containing 8 m of double-clad fiber, and a fiber coil L2. A2 emits 1.2 W of output power under 5 W of pump power. Both the UR and NALM loops contain a polarization controller (PC1 and PC2) to adjust the polarization states and enhance the mode-locking in the cavity. The fiber coil lengths L1 and L2 and the central coupling ratio are carefully chosen to optimize the characteristics of the pulse.

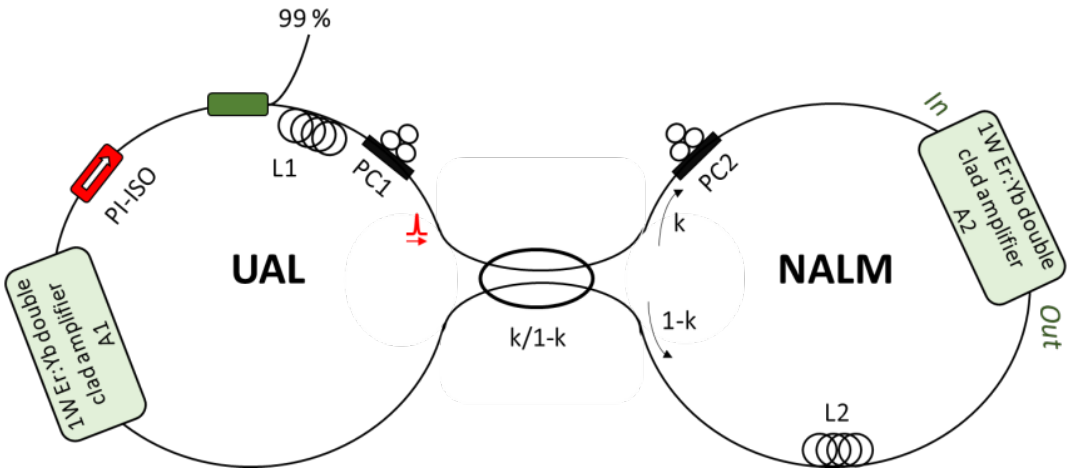

Figure 3.1: Experimental configuration of dual-pump figure-8 fiber laser

To start, the coupling ratio is set to $k = 0.5$. The total cavity length is about 1536 m, including SMF coils $L1 = 1000\ m$ and $L2 = 500\ m$, with a second-order dispersion $\beta_2 = -0.022\ ps^2/m$ and the double-clad fiber of the amplifiers with second-order dispersion $\beta_2 = -0.021\ ps^2/m$. The net cavity dispersion is about $\beta_2 L = -33.23\ ps^2$ and the round-trip time is $T_{cavity} = 7.65\ \mu s$ corresponding to a free spectral range of $FSR = 133\ kHz$. The output signal is extracted with a 99% output coupler, which allows a maximum output power when the pump power on both sides is high.

(b) Influence of the pump power of amplifiers A1 and A2

After setting the polarization controllers' position to generate the square-wave mode-locking state, the authors studied the influence of the pump power of each amplifier A1 and A2, on the pulse duration and peak power.

Influence of the A1 pump power

To study the effect of the A1 pump power on the rectangular pulses, the A2 pump power has been set to a fixed value of 1.8 W, and the pump power of A1 is tuned from 500 mW to 3 W. The resulting square pulses are shown in figure 3.2 and one can note that the output pulse duration is nearly constant at about 416 ns, while their intensity increases versus the pump power of A1. Considering the laser output power, its repetition rate, and the pulse width, the authors show that the peak power and pulse energy of the square pulses increases linearly according to the formula $P_{peak} = E_{pulse}/T_{pulse}$. This result is in agreement with previous theoretical work [42] and experimental results of Mei et al. [41] where the authors reported that when the gain is increased in the UR, the peak power of the pulses increases without modifying the pulse width of the generated square-pulses.

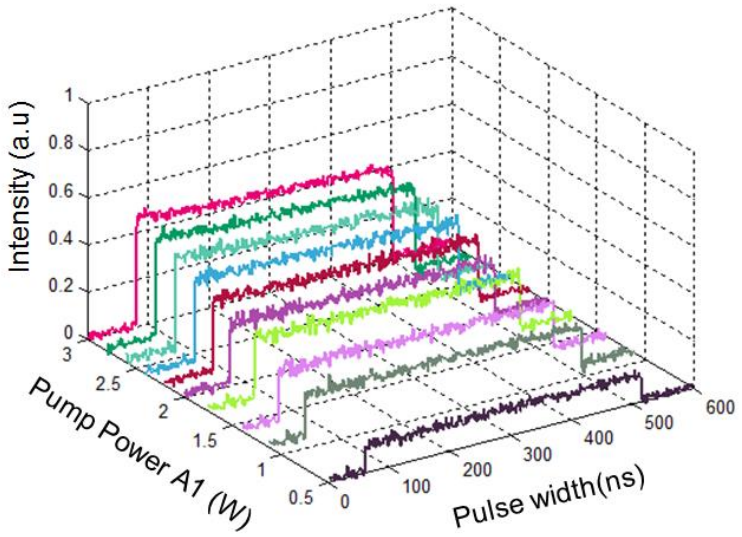

Figure 3.2: Temporal profile of the generated square-wave pulses with a pump power of A2 fixed at 1.8 W and A1 tuned from 0.5 W to 3 W.

Influence of the A2 pump power

The same measurements have been performed by fixing the pump power of amplifier A1 to its maximum of 3 W and tuning the pump power of the amplifier A2 from 150 mW to 1.7 W. The resulting pulses are shown in figure 3.3. The pulse width and the pulse energy increase linearly with the pump power. However, as the energy per pulse is slowly increasing compared to the fast increase of the duration, the pulse peak power is decreasing. This is in contrast with the results of [41] where the peak power is constant. However, in [41] A1 was completely turned off after generating a stable square-pulse regime, which enables demonstrating the independence of amplifiers A1 and A2. To

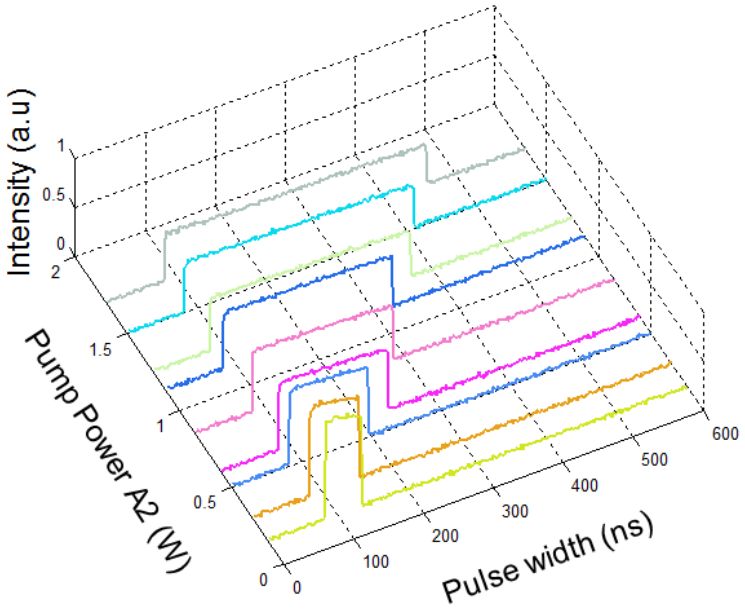

Figure 3.3: Temporal trace of the generated Square-wave pulses with a pump power of A1 fixed at 3 W and A2 tuned from 120 mW to 1.7 W.

conclude, by setting A2 to a constant value and tuning A1, the pulses keep the same duration while the peak power is increased. On the other hand, when the pump power of A1 is fixed and A2 is tuned, the duration of the pulses has increased. However, since the A1 is not turned off, the peak power of the pulses decreased instead of being constant. Nevertheless, the pulse energy of the resulting pulses achieved high values in this configuration, reaching nearly 10 μJ as the record energy for DSR-like square pulses.

In order to optimize the experimental configuration to obtain high-energy square pulses, the influence of the central coupling ratio of the cavity and its total dispersion on the pulse characteristics was also studied.

(c) Influence of the central coupling ratio k

The influence of the coupling ratio k is studied both when the pump power A2 is constant and A1 varies and when the pump power of A1 is constant and A2 varies. Three different values of k are tested: $k = 0.5, 0.6, 0.7$. Figure 3.4 shows the results when the pump power of A2 is fixed to 1.8 W and the pump power of A1 varies from 0.5 W to 3.5 W. As shown in Figures 3.4a and 3.4b, the pulse energy and peak power increase linearly with the pump power of A1. For $k = 0.5$, when the pump power of A1 increases from 0.5 W to 3.5 W the pulse peak power increases linearly from 6 W to about 33 W. similarly, the energy increases linearly from 1.6 μJ to 9.5 μJ. Figure 3.4c shows a constant value of the pulse duration of about 288 ns. The same measurements have been recorded for $k = 0.6$. The peak power of the pulse increases from 9 W to 41.3 W. The energy increases from 2 μJ to 10.1 μJ. The duration, which equals 245 ns, remains invariable with the pump power. Finally, for k= 0.7, the pulse duration remains constant, around 416 ns. The peak power increases from 5 W to approximately 24.3 W. Consequently, the energy increases from 2 μJ to 10.1 μJ which represents the record energy ever achieved for the square pulses in the DSR regime [39]. Similarly, figure 3.5 shows the evolution of the square pulse in the case where the power of A1 is fixed to 3 W and the power of A2 varies from 0.2 W to 1.8 W, for the different values of the coupling ratio k. With the increasing pump power of A2, the pulse duration increases linearly while the peak power decreases. Therefore, the energy of the rectangular pulse $E_{pulse} = P_{peak} \times T_{pulse}$ increases very slightly with increasing pulse duration. More specifically, for $k = 0.5$, the pulse peak power shown in figure 3.5a, decreases from 141 W to 33 W. As the pulse duration increases from 59 ns to about 288 ns, (cf. figure 3.5c), the energy increases slightly from 8.3 μJ to 9.5 μJ (cf. figure 3.5b). For $k = 0.6$, the pulse duration increases from 48 ns to

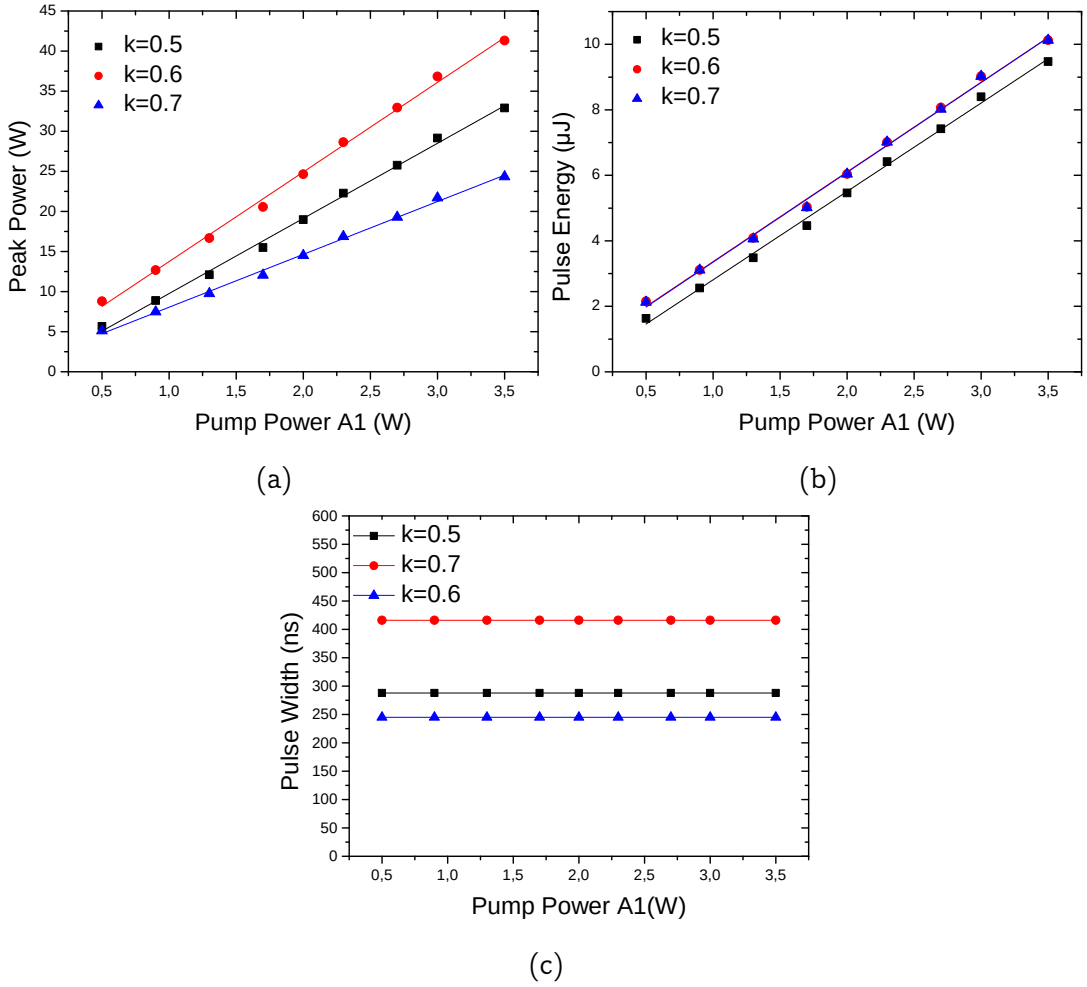

Figure 3.4: Variation of (a) the pulse peak power (b) the pulse energy (c) and the pulse duration as a function of the pump power of the amplifier A1.

245 ns. The energy varies from 8.7 μJ to 10.1 μJ. The peak power decreases from 181 W to 41.3 W. Finally, for the coupling coefficient $k = 0.7$, the pulse duration increases from 84 ns to 416 ns. The peak power of the pulse goes from 102 W to approximately 24.3 W, and the energy increases from 8.5 μJ to 10.1 μJ.

In the studied laser configuration, it was concluded that $k = 0.7$ gives the best performance in terms of pulse duration and energy. This observation is confirmed in the next section, by studying the effect of the dispersion in the laser cavity.

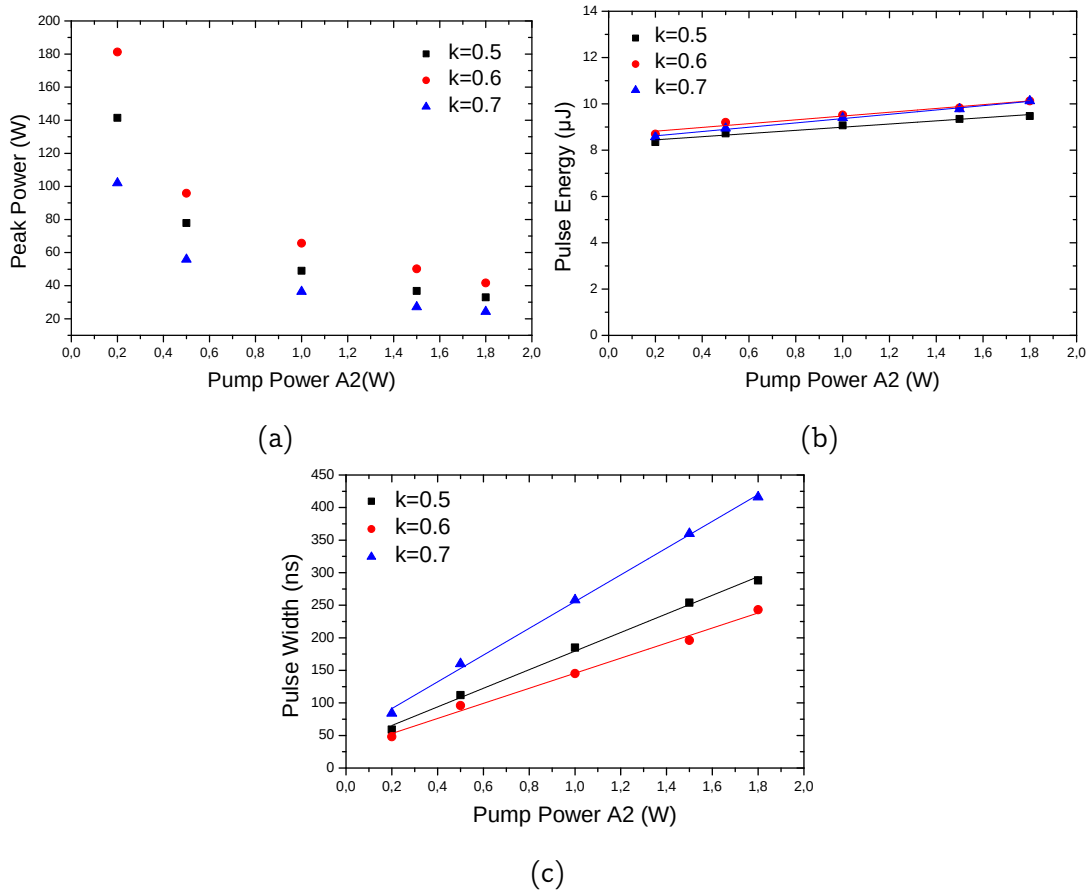

Figure 3.5: Variation of (a) the pulse peak power (b) the pulse energy (c) and the pulse duration as a function of the pump power of A2.

(d) Influence of the fiber coil lengths L1 and L2

To study the influence of the dispersion, and the effect of L1 and L2 fiber coils in the cavity, different lengths of L1 and L2 were tested in the UR and NALM loops. As shown in Figs. 3.6a and 3.6b, both the pulse energy and the pulse width are larger for L1 = 1000 m and L2 = 500 m. Furthermore, for a net cavity dispersion set at -33 ps^2, inserting L1 = 1000 m rather than L2 = 1000 m permits a stable square pulse regime. In addition, the position of the SMF28 fiber coil in the NALM loop is another key parameter that strongly modifies the characteristics of the pulse. Inserting the L2 coil at the output of amplifier A2 generates a larger pulse duration than inserting it at the input. To summarize, figure 3.7 shows the variation range of the energy and the pulse duration as a function of the total dispersion of the cavity for the three values

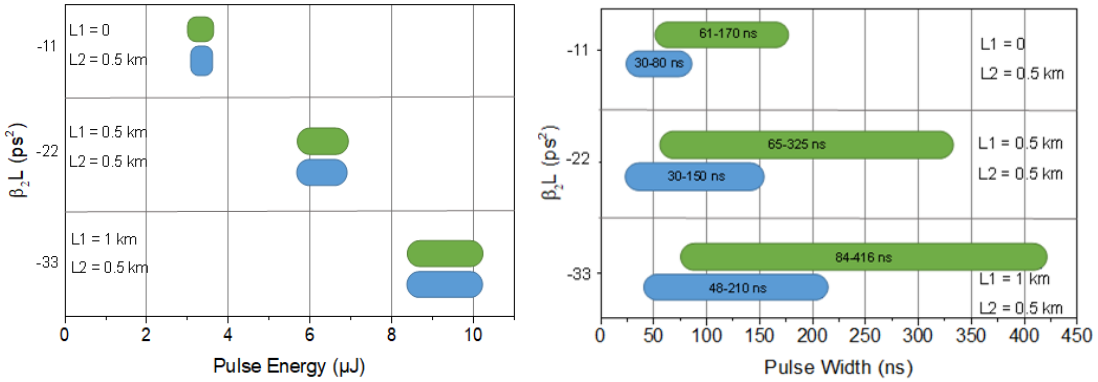

(a) (b)

Figure 3.6: Variation as a function of L2 position of (a) energy and (b) pulse duration for different values of total cavity dispersion.

of the central coupling rate $k = 0.5$, $k = 0.6$, and $k = 0.7$. Figures 3.7a and 3.7b show that the choice of $k = 0.7$ is the best in terms of pulse duration. This choice of k is valid for all the values of the cavity total dispersion used in the experiment. The figures also demonstrate that the best performance is obtained for the highest dispersion values.

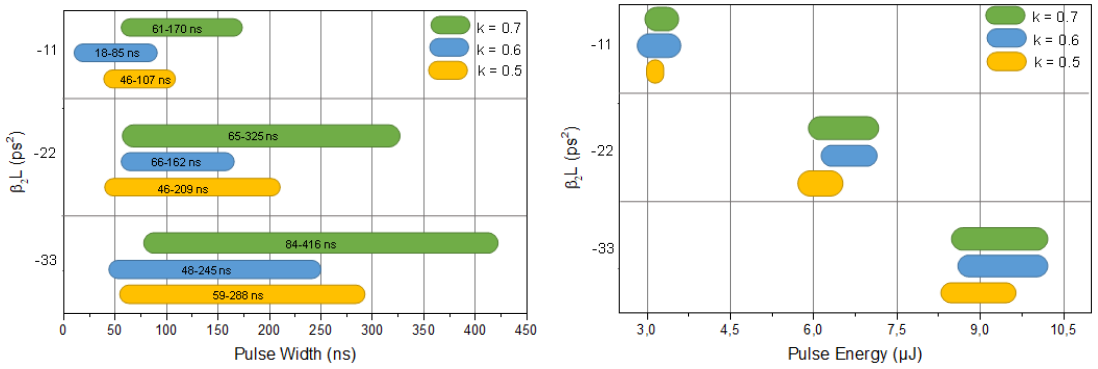

(a) (b)

Figure 3.7: Variation of (a) pulse-width (b) and pulse energy as a function of the cavity dispersion for different values of the central coupling ratio k

(e) Conclusion

The dual amplifier figure-of-eight fiber laser is characterized by high-energy pulses and adjustable pulse duration. First, it has been shown that with the

pump power of each amplifier A1 and A2 separately, it is possible to tune the duration and the peak power of the pulses. Also, it has been found that the coupling ratio $k = 0.7$ gives the best performance in terms of pulse duration. Finally, under optimal conditions such as inserting the SMF28 coil L2 at the output of amplifier A2, or setting $L1 > L2$, with high net cavity dispersion, the double-amplified figure-of-eight laser delivers rectangular pulses with pulse width between 84 and 416 ns and pulse energy varying between 8.5 and 10.1 μJ [39]. In the next part, I present another study that was performed to investigate the harmonic operation of the DSR-based square pulses obtained by adjusting the polarization controllers.

3.2.2 Multi-pulsing instabilities

This section is devoted to the study of multi-pulsing instabilities in the so-called DSR regime. These instabilities manifest in a harmonic distribution of the square wave pulses [40].

Experimental setup

The square-wave pulse experimental setup, shown in figure 3.8, is based on an all-fiber ring cavity. The mode-locked regime is achieved by exploiting the nonlinear polarization evolution mechanism. The laser cavity is composed of a double-clad Er:Yb fiber amplifier with a set of polarization controllers and a high-power polarization sensitive isolator PS-ISO to form an artificial saturable absorber. A polarization-insensitive isolator is used to ensure the unidirectional path of the signal. The latter is extracted with a 30 % fiber coupler. An additional 250-m coil of SMF-28 is spliced considering the interest of a large anomalous dispersion for the generation of square wave pulses. Thus, the total cavity length is 300 m, including 295-m of SMF with a second order dispersion of $-0.022\ ps^2/m$ leading to a net dispersion of about $-6.6\ ps^2$. The round-trip time of the cavity is 1.488 μs which corresponds to a free spectral range of 672 kHz.

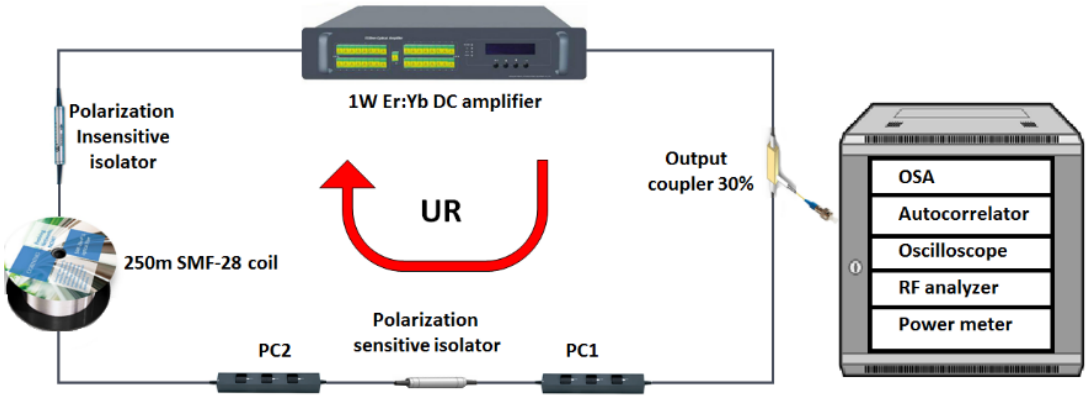

Figure 3.8: Experimental setup of the ring cavity.

Harmonically distributed square wave pulses

The so-called DSR pulses are generated at the threshold pump power of 400 mW and operate at the fundamental repetition rate. By fixing the polarization controller's position and progressively increasing the pump power from 1.2 W to the maximum value of 3 W, the duration of the square pulses widens to reach about 270 ns while the peak power remains nearly constant. Under these conditions, the pulses do not suffer from wave-breaking. However, when the pump power is fixed and the polarization controllers are adjusted, the square pulse can split into many shorter square pulses with the same shape and width. Thus, the laser operates at high harmonic DSR mode locking as depicted in figure 3.9. Thus, for a pump power value of 1.18 W, it was possible to generate up to the 4th harmonic order, by adjusting the position of the polarization controllers. The corresponding signals are depicted in red in figure 3.9. At 1.6 W of pump power, and by adjusting the PCs, the 6th harmonic order was generated as plotted in the blue curve in figure3.9. Further increase of the pump power to 2.2 W allows the generation of higher harmonics up to the 13th order as depicted in green in figure 3.9 representing the 9th, the 11th, and the 13th order. No higher harmonic order has been generated for a higher value of the pump power.

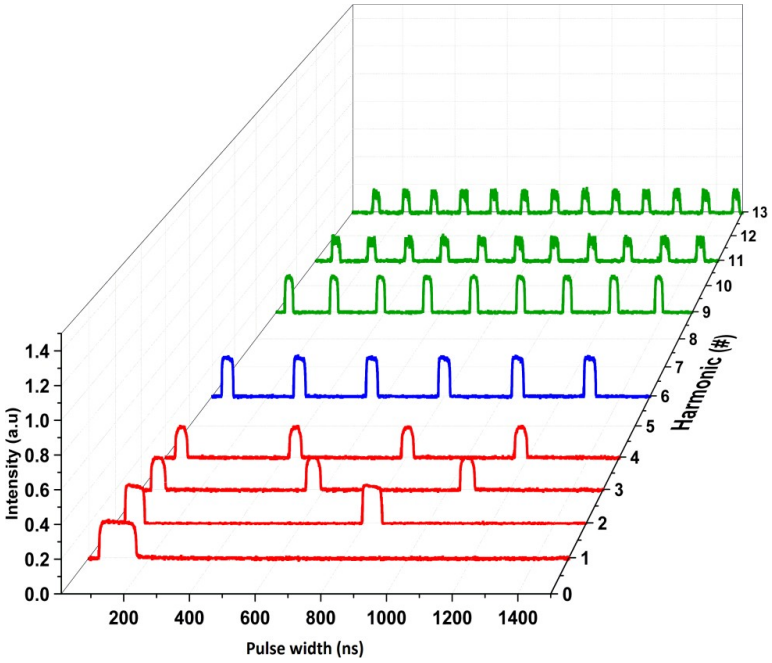

Figure 3.9: Harmonic mode-locked DSR square pulses train of different orders achieved by adjusting the PC. Each color is assigned to different pumping power (red for 1.18 W, blue for 1.6 W, and green for 2.2 W).

Conclusion

In this study, the authors have experimentally demonstrated harmonic square wave pulses with a mode-locked fiber laser operating in the DSR regime [40]. Thus, by adjusting the polarization controller's position, the fundamental square pulse can evolve into a stable high harmonic mode-locking of DSR square pulses. For the pump power of 2.2 W, it was possible to generate the 13th harmonic order of the square pulse.

In the next part of this chapter, I experimentally study rectangular pulses using a ring laser cavity. The aim is to optimize the pulse characteristics, especially in terms of pulse stability while increasing the pump power. This optimization will allow a further study of temporal coherence, which I present in the next chapters.

3.3 Rectangular pulses in a ring laser cavity based on NPE mode-locking mechanism

In this section, a characterization of rectangular pulses, generated by the passively mode-locked fiber laser, is performed. A single-mode fiber (SMF) and dispersion-shifted fiber (DSF) are utilized as a fiber coil in the laser cavity. These different types of fiber are used to investigate better conditions for producing DSR rectangular pulses.

3.3.1 Experimental setup: all-fibered ring laser cavity

Figure 3.10 shows the experimental setup. The laser cavity is a unidirectional ring (UR) enabling the generation of mode-locked rectangular pulses using the nonlinear polarization evolution mechanism [43]. The cavity includes a C-band double-clad co-doped Er:Yb 30 dBm fiber amplifier (EYDFA) from Lumibird company (KPS-BT2-C-30-BO-FA), a set of polarizer and polarization controllers (PC1 and PC2), a polarization-insensitive isolator (PI-ISO) ensuring the unidirectional propagation of light and an additional coil of single-mode fiber (SMF 28). An optical coupler (OC) is used to extract 20% of the signal to study the characteristics of the rectangular pulses. The laser is adjusted to deliver rectangular pulses in the nanosecond range, typically a few tens of ns.

The laser output measurements are monitored by a 13-GHz oscilloscope (Agilent infiniium DSO8130B) combined with two 12-GHz photo-detectors (TTI, Model TIA1200 O/E Converter), an optical spectrum analyzer (Anritsu MS9740A, 0.6 μm - 1.7 μm, 30 pm resolution bandwidth), and an electronic spectrum analyzer (Rohde & Schwarz FSP Spectrum Analyzer 9 kHz to 13.6 GHz) to investigate the temporal trace, the optical spectrum, and the radio-frequency signal, respectively. Finally, a high-power integrating sphere (Thorlabs S146C) is used to measure the average power of the laser.

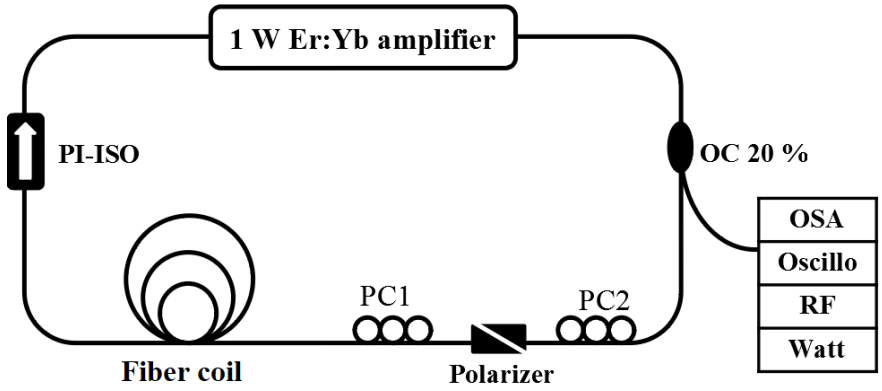

Figure 3.10: Experimental setup. EYDFA: Erbium-Ytterbium co-doped fiber Amplifier, OC: optical coupler, PC1,2: polarization controller, PI-ISO: polarization-insensitive isolator.

3.3.2 Single-mode fiber-based laser cavity

Herein, an SMF coil is used in the laser cavity. The total cavity length is about 304 m, including 5 m-long double-clad fiber with second-order dispersion $\beta_2 = -0.021\ ps^2/m$ and 299 m of SMF-28 with $\beta_2 = -0.022\ ps^2/m$. The total net cavity dispersion is estimated at $-6.683\ ps^2$. The round-trip time corresponds to 1.52 μs. After stabilizing the laser cavity, a rectangular pulse regime occurs. Figure 3.11, shows the resulting signal. The temporal trace, depicted in figure 3.11a, represents one pulse per cavity round-trip time corresponding to 1.52 μs. As shown in the inset figure, the pulse width reaches 60.6 ns at the pump power of 5.06 W. The pulse rise and fall times are very short, however, the top profile of the pulse is not completely flat. The corresponding optical spectrum depicted in figure 3.11b, is centered at 1568 nm and has a bandwidth of 9.25 nm, but its pedestal is relatively large. The inset figure represents the linear evolution of the spectrum. This representation may be interesting to better resolve the top of the central wavelength or other wavelengths. The RF spectrum of figure 3.11c shows the signal-to-noise ratio which is around 50 dB. For additional information, figure 3.12 shows the evolution of the regime with the pump power which is increased from 2.26 W to 5.21 W. The temporal traces corresponding to each pump power value is depicted in

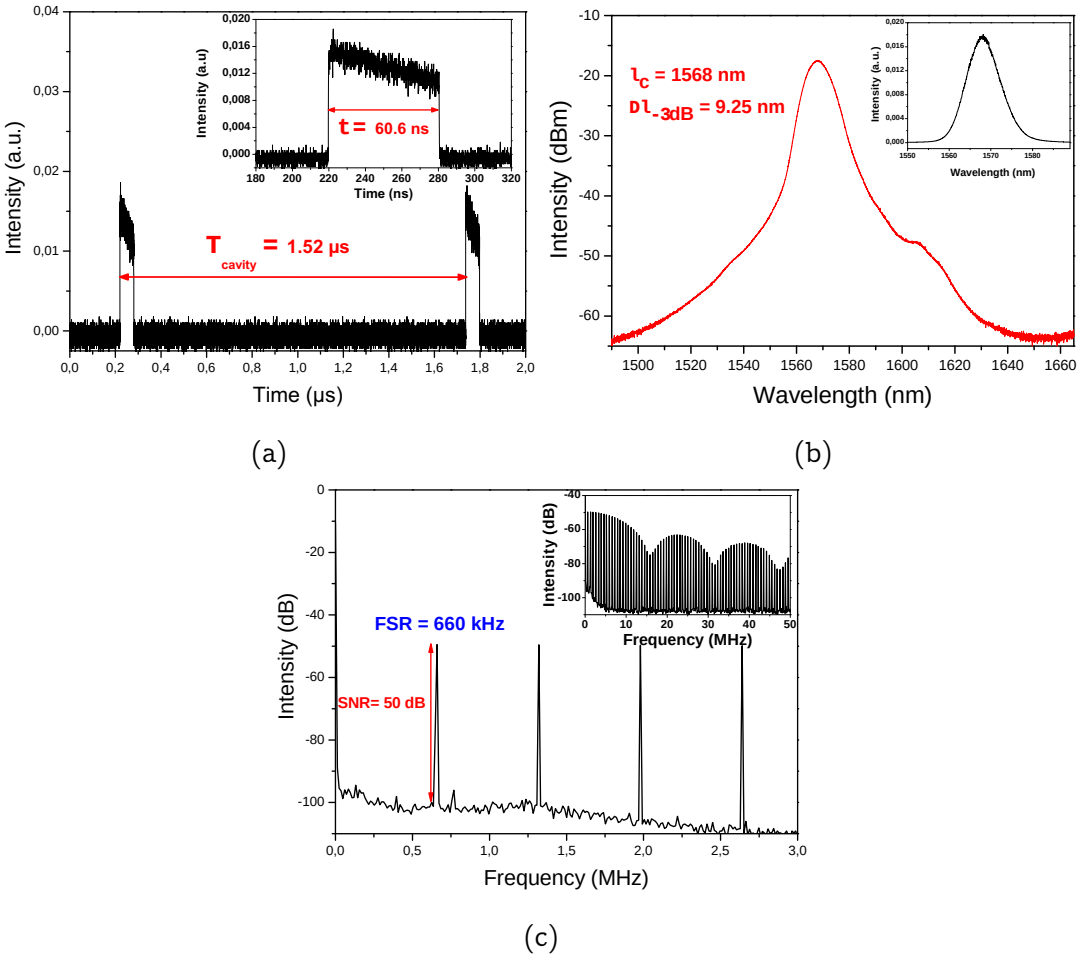

Figure 3.11: (a) Temporal trace of rectangular pulses, (b) the corresponding optical spectrum, and (c) the radio-frequency trace, at the pump power of 5.06 W.

figure 3.12a. The regime is stable and no wave-breaking occurred. Instead, the pulse width increases with the increase of the pump power. Figure 3.12b and the inset figure, show the corresponding evolution of the optical spectrum, in logarithmic and linear scales. The optical spectrum remains unchanged, except for the signal intensity which increases with increasing pump power.

In figure 3.13, the common features of DSR pulses are verified. Figure 3.13a represents the measured pulse width in red stars. The red curve is a linear fit and confirms that the pulse width is linearly increasing with the pump power. The blue dots represent the measured peak power, which is linearly fitted with the blue curve. The peak power remains constant with the pump power, as

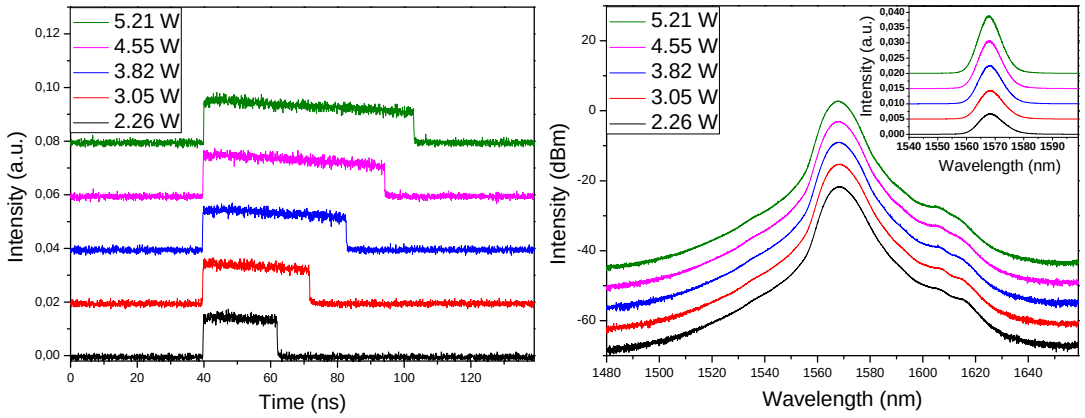

(a) (b)

Figure 3.12: (a) Temporal trace of rectangular pulses for pump power ranging from 2.26 W to 5.21 W. (b) The corresponding optical spectra for the same range of pump power in dBm scale (and in linear scale represented in the inset figure).

expected for a DSR pulse. Figure 3.13b represents the measured pulse energy in red dots, which are fitted by a linear red curve.

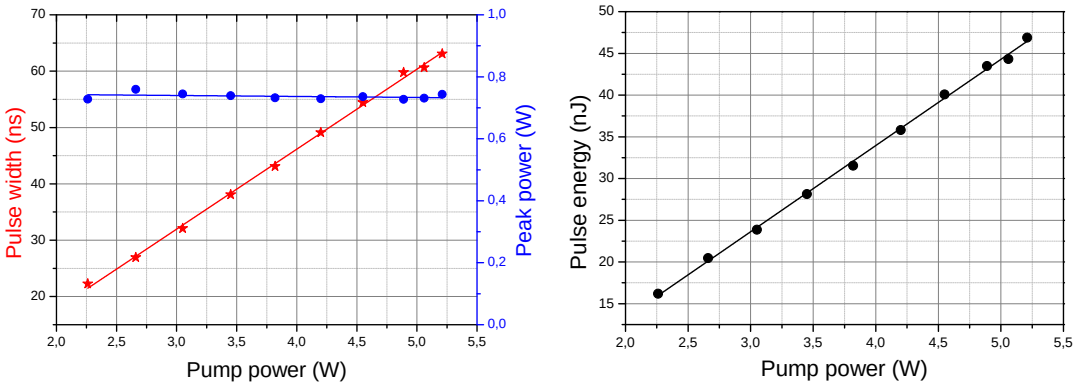

(a) (b)

Figure 3.13: Characteristics of rectangular pulses. Evolution of the (a) pulse width (red stars linearly fitted by red curve), the peak power (blue dots fitted by linear blue curve), and (b) the pulse energy (red dots with a linear fit curve) with pump power ranging from 2.26 W to 5.21 W.

Finally, these characteristics are as expected for DSR pulses. Indeed, the

regime is stable while increasing the pump power, and there is no wave-breaking. Both the pulse width and the pulse energy increase linearly, while the peak power remains constant. Also, one can note that the optical spectrum remains unchanged versus the pump power.

In the next section, another regime of rectangular pulses is studied with a different type of fiber coil in the laser cavity. Thus, a dispersion-shifted fiber is used instead of single-mode fiber.

3.3.3 Dispersion-shifted fiber-based laser cavity

In this section, the rectangular pulses regime is studied with a slightly different laser cavity. The aim is to search for a more stable regime. Here, a dispersion-shifted fiber (DSF) with different dispersion characteristics than the SMF is used. The total cavity length is about 216 m including a 200 m DSF coil with a second-order dispersion of $\beta_2 = -0.00369\ ps^2/m$, 5 m-long double-clad fiber, and 11 m-long SMF fiber. The total net dispersion is estimated to be -0.39 ps^2. Note that the net dispersion, in this case, is very low compared to previous experiments. As studied in the previous section, the characteristics of the rectangular pulses are verified. These characteristics are depicted in figure 3.14, and are measured at a pump power of 5.06 W. Figure 3.14a shows the temporal profile. There is one pulse per cavity round-trip time and can reach up to 25 ns of pulse width as shown in the inset figure. The optical spectrum is presented in figure 3.14b. The signal is centered at 1564.7 nm and is characterized by a bandwidth of 11 nm. Here also, we can see that the optical spectrum trace has a wide pedestal. The radio-frequency trace is shown in figure 3.14c and displays a high signal-to-noise ratio of about 66 dB, so the regime is relatively stable. Similarly to the previous section, figure 3.15 shows the evolution of the regime with pump power ranging from 2.26 W to 5.21 W. Figure 3.15a shows the temporal trace, which keeps the rectangular shape and grows in width without wave-breaking. Figure 3.15b represents the optical spectra in the log scale where the inset represents the linear scale. Even if the pedestal of the optical spectrum is wide, this latter stays unchanged with the

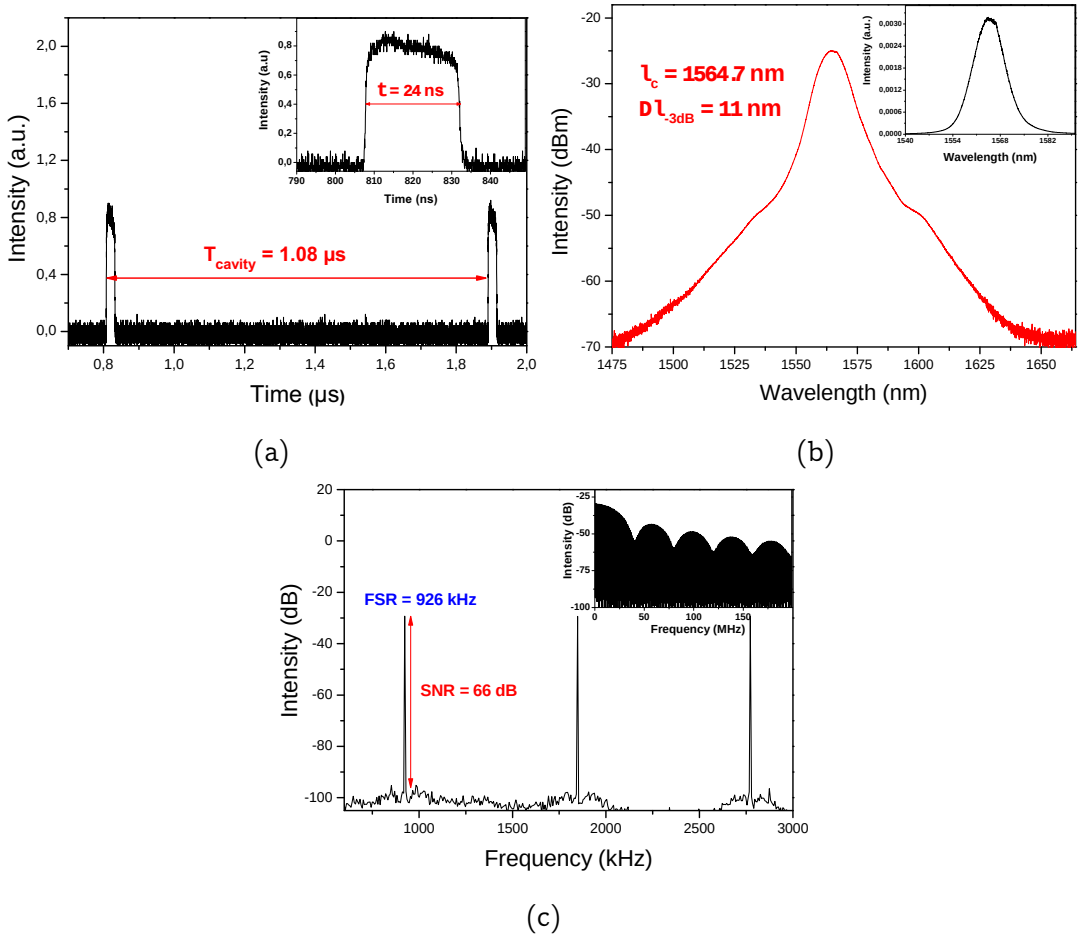

Figure 3.14: Temporal trace of rectangular pulses (a), the corresponding optical spectrum (b), and the radio-frequency trace (c).

pump power. The pulse width and the peak power are represented in figure 3.16a. The pulse width is linearly increasing, while the peak power remains clamped at a constant value. Figure 3.16b represents linearly increasing pulse energy. This evolution with the pump power is as expected for DSR pulses.

Consequently, in this section, it is shown that the studied rectangular pulses regime seems to fulfill all the characteristics of the DSR regime. However, the optical spectrum exhibits a wide pedestal. This can be a manifestation of a noise-like regime. In the next part, cavity optimization is performed. The goal is to search for a rectangular regime with better optical spectrum characteristics so that there is no pedestal.

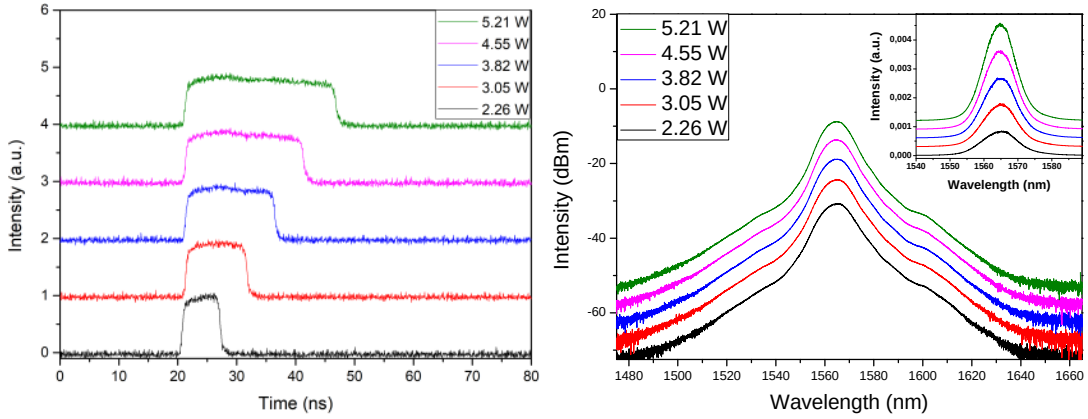

(a) (b)

Figure 3.15: (a) Temporal trace of rectangular pulses for pump power ranging from 2.26 W to 5.21 W. (b) The corresponding optical spectra for the same range of pump power in dBm, and in linear scale represented in the inset.

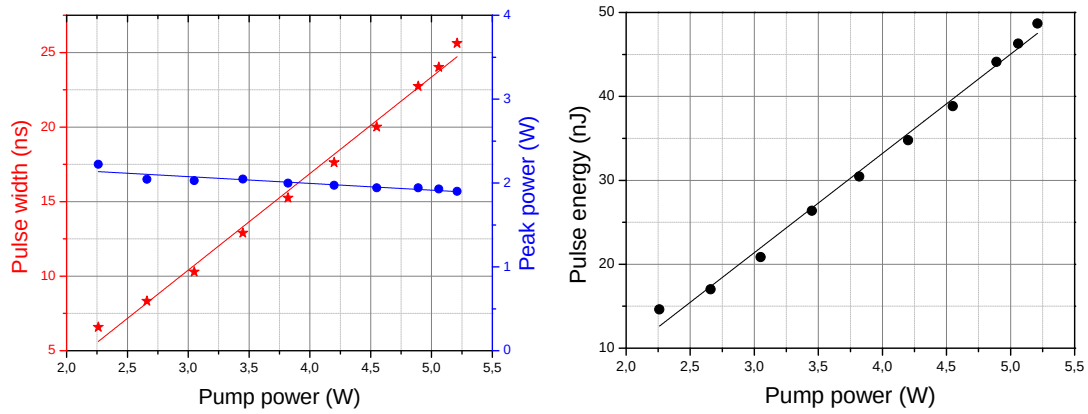

(a) (b)

Figure 3.16: Characteristics of rectangular pulses. Evolution of the (a) pulse width (red stars linearly fitted by red curve), the peak power (blue dots fitted by linear blue curve), and (b) the pulse energy (red dots with a linear fit curve) with pump power ranging from 2.26 W to 5.21 W.

3.3.4 Spectrum optimization

The same characteristics of rectangular-shaped pulses as previously are studied. The fiber coil is consisting of SMF-28. The total cavity length is about 290 m, corresponding to a round-trip time of 1.45 μs. The total net cavity dispersion

is estimated at $-6.375\ ps^2$.

The pulse temporal trace is given in figure 3.17a, obtained at a pump power of 2 W. There is one pulse per cavity round-trip, with a pulse width of 35.4 ns, as shown in the inset of figure 3.17a. The corresponding optical spectrum is centered at a wavelength of 1612 nm as shown in figure 3.17b. The spectral 3 dB bandwidth is 9.2 nm. Figure 3.17c represents the RF spectrum trace with a signal-to-noise ratio of 68 dB, indicating high signal stability. The inset depicts a sinc-function modulated signal corresponding to the Fourier transform of a rectangular pulse.

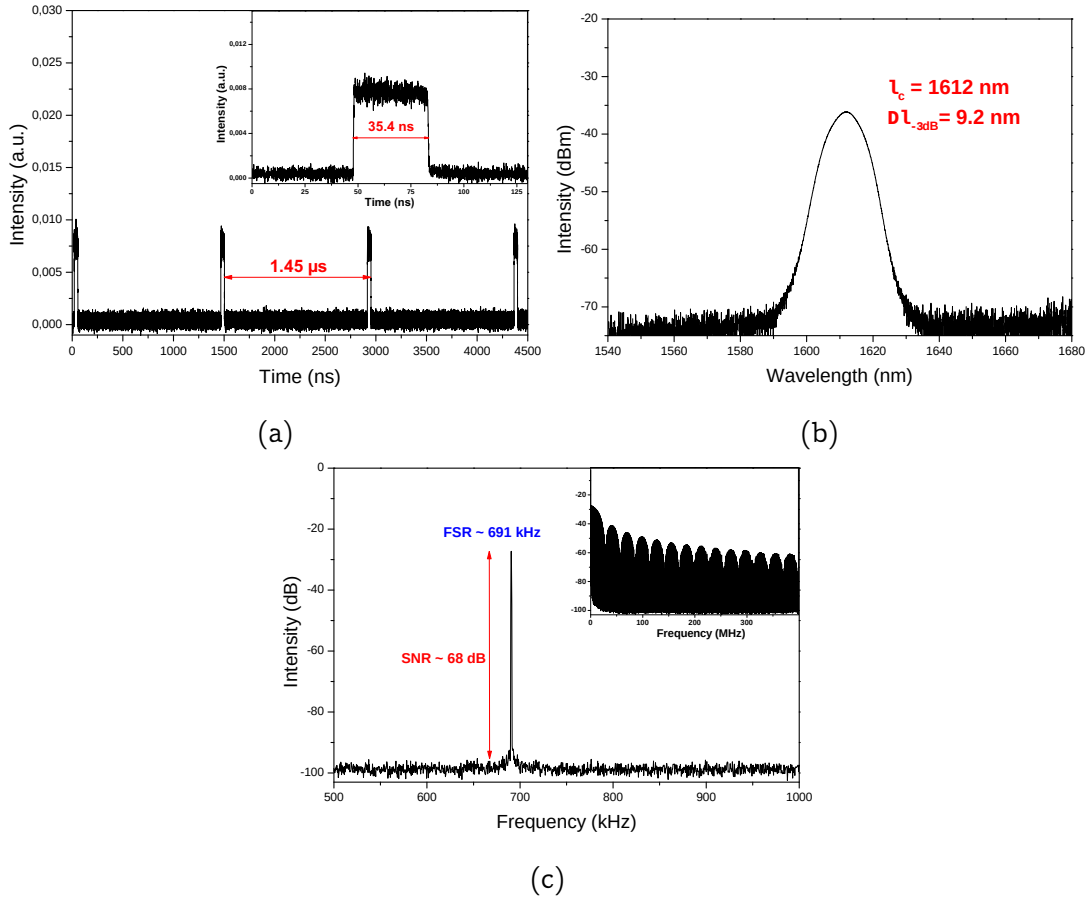

Figure 3.17: Temporal trace of rectangular pulses (a), the corresponding optical spectrum (b), and the radio-frequency trace (c).

By increasing the pump power from 0.8 W to 4.02 W without any PC readjustment, the pulse remains perfectly rectangular without suffering from

any wave-breaking as illustrated in figure 3.18a. The same observation is made concerning the optical spectrum, which also keeps its initial shape, as shown in figure 3.18b, by holding the spectral bandwidth at -3 dB around the same value of 9 nm as depicted in figure 3.18c.

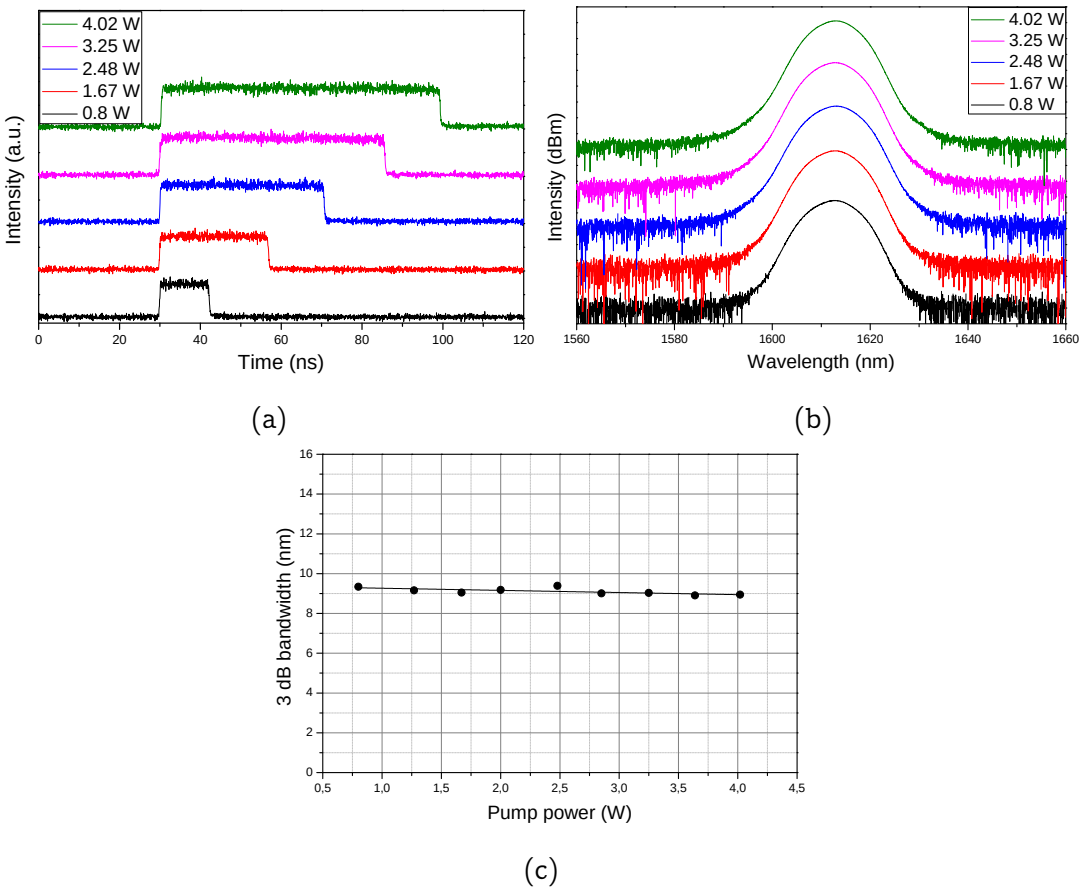

Figure 3.18: (a) Temporal trace of rectangular pulses for pump power ranging from 0.8 W to 4.02 W. (b) The corresponding optical spectrum for the same range of pump power. (c) 3-dB bandwidth of the spectrum as a function of pump power.

The other characteristics required to study the eventual DSR nature of these pulses are also studied and shown in figure 3.19. In figure 3.19a, the pulse width (red stars fitted with a linear red curve) increases linearly with the pump power, whereas the peak power (blue dots fitted with a linear blue curve) remains nearly constant. Pulse energy also follows the increasing linear evolution with the pump power, as shown in figure 3.19b.

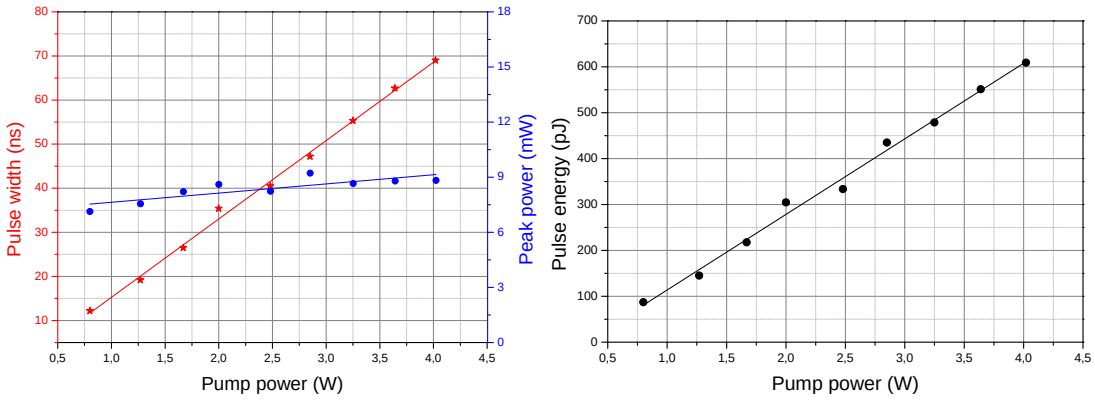

(a) (b)

Figure 3.19: Characteristics of rectangular pulses. Evolution of the (a) pulse width (red stars linearly fitted by red curve), the peak power (blue dots fitted by linear blue curve), and (b) the pulse energy (black dots with a linear fit curve) with pump power ranging from 0.8 to 4.02 W.

Finally, these characteristics are as expected for a DSR pulse. We also note a better optical spectrum with no large pedestal and a better signal-to-noise ratio in terms of radio frequency compared to the regimes studied in sections 3.3.2 and, 3.3.3.

3.3.5 Conclusion

To conclude, in section 3.3, I studied the DSR-like rectangular pulses in a ring laser cavity. I have used two different fiber coils: SMF and DSF, for which I got approximately similar results despite the difference in the net dispersion. Also, I tried to optimize the optical signal and I noticed that, for a narrower optical bandwidth, around 4 nm, as obtained in previous studies of my group, it was necessary to slightly adjust the polarization controllers while I increased the pump power. Taking into account this observation, when I get the rectangular pulse regime, I hold the PCs at the same position during the experiment while I increase the pump power. With this method, the signal optical bandwidth is wider and is around 9 nm, but the polarization state is not modified, which allows a more accurate measurement of the pump power influence on the laser

regime.

3.4 Conclusion

In this chapter, I introduced the concept of dissipative soliton resonance. In the first section, I gave a brief review of early theoretical reports on the phenomenon. In the second and third sections, I gave an overview of the previous work of my group where they studied different laser cavity parameters to optimize the square pulse laser regime. Thus, by using a dual-amplifier figure-of-eight fiber laser they generated very high-energy square pulses up to 10 μJ, which is the record value ever achieved with this regime. They also obtained high-harmonic square pulses using a ring fiber laser cavity by adjusting the polarization controllers. In the fourth section, I presented my first experimental studies of the DSR-like square pulses, where I also attempted to optimize the ring laser cavity for a more stable regime. I also tested a laser cavity with a very low net dispersion by using a dispersion-shifted fiber (DSF). The resulting regime seems to exhibit similar characteristics compared to that for higher net negative dispersion.

Based on these experimental reports and the experimental literature on the DSR-like regime, the question of the temporal coherence of these square pulses, which seem to be DSR pulses, is not completely solved. In many experimental reports, the coherence of the pulses is not rigorously studied. Usually, the authors provide an autocorrelation trace of the pulse, however, in our case, for example, the autocorrelation trace may not be sufficient to conclude whether the square pulse is coherent or not, i.e. if the square pulse is unique or if it is an envelope of thinner pulses. In parallel, there have been many studies on the noise-like square pulses [44–46] for which the characteristics are similar to those of the DSR pulses. Indeed, a noise-like square pulse manifests as a square envelope whose pulse width increases linearly with the pump power and whose optical spectrum remains invariable as expected for the DSR pulses. Also, the noise-like pulses get higher energy with constant peak power. In the

next chapter, I investigate the temporal coherence of the experimental square pulses, using a Mach-Zehnder interferometer to circumvent eventual artifacts of the autocorrelation apparatus. We will then be able to determine whether the obtained square pulses are DSR or noise-like pulses.

Chapter 4

Coherence characterization of nanosecond rectangular pulses using Mach-Zehnder interferometer

The dissipative soliton resonance (DSR) phenomenon [23, 24] is a recent concept of pulse generation proposed to attain a high-energy mode-locked laser. In a passively mode-locked fiber laser, such pulses have common characteristics, such as flat-top temporal profile, energy scalability, and temporal coherence. In the experimental literature of the DSR regime, rectangular pulses are assumed to be a manifestation of DSR when they exhibit some behavior with the variation of the pump power. It is characterized by a linear increase of the pulse width and energy with a clamped peak power without experiencing any wave-breaking, and with an invariant optical spectrum. Besides, to ensure that these pulses are DSR, they must be temporally coherent, without any fine structure within the envelope. Despite the necessity of the latter feature, only a few researchers have investigated the coherence of such rectangular pulses by providing an autocorrelation trace [25, 47]. It is worth mentioning that they reported on short pulse durations (several hundreds of picoseconds) with high repetition rates (above 1 MHz). However, for higher energy pulses, the configurations of the laser cavities are adjusted and most of the studied DSR square pulses are in the nanosecond regime with low repetition rates, in kHz.

Furthermore, the usual autocorrelators may be limited when the pulse repetition rate is lower than a threshold set by the manufacturer. In our case, the autocorrelation trace is not accurate for repetition rates below 1 MHz. Also, the span limit of the autocorrelator is 200 ps while the studied pulses are in the range of nanosecond of pulse width. In addition, let us mention that even when the repetition rate of the laser is compatible with the optical autocorrelator, the resulting trace is not sufficient to state on the coherence of the pulse. Indeed, in theory, if the pulse is not coherent, a peak appears in the center of the autocorrelation trace whereas it does not occur for a coherent pulse. However, when the experimental setup includes a polarization controller at the entrance of the optical autocorrelator to optimize the signal, the existence of a central peak in the autocorrelation trace depends on the adjustment of the polarization controller. Then, it is impossible to conclude about the coherence of the square pulses since the absence of a central peak can have several origins. To overcome these issues, we present herein a reliable experimental setup to investigate the coherence of large rectangular-shaped pulses in passively mode-locked Er:Yb co-doped double-clad fiber laser [48]. The experimental setup consists of a Mach-Zehnder interferometer (MZI).

In this chapter, I start by reminding the principle of the MZI. In the second section, I will present the interferometry results with an all-fibered MZI. In the third section, I will show an improved MZI study where I inserted free-space collimators, permitting a fine adjustment of the path difference.

4.1 Principle of Mach-Zehnder Interferometer

The Mach-Zehnder interferometer is an amplitude division interferometer. It is consisting of two mirrors and two beam splitters as shown in the schema of figure 4.1. The first beam splitter (BS1) divides the light into two beams which are reflected by the mirrors M1 and M2 and then recombined by the second beam splitter (BS2). The resulting interferometric beam is detected on the photodetectors D1 and D2.

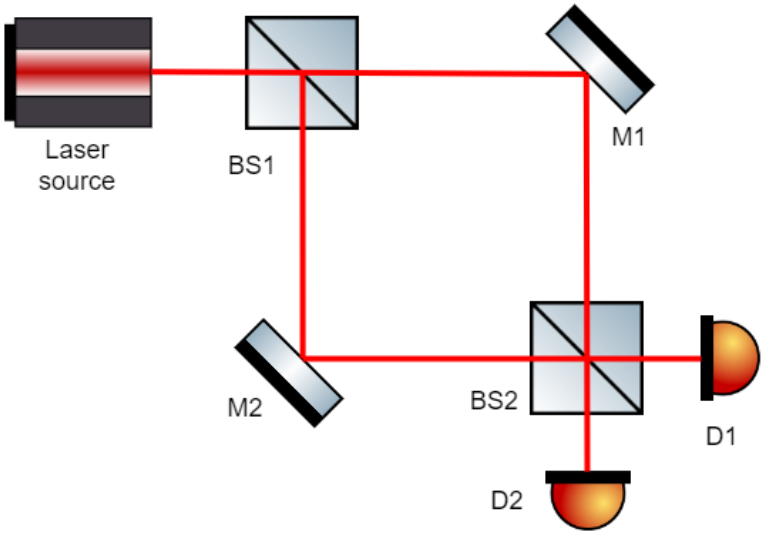

Figure 4.1: Schema of Mach-Zehnder interferometer. BS: beam splitter, M: mirror, D: photo-detector

4.1.1 Interference of light

The electric field of the monochromatic electromagnetic wave is:

$$E = Ae^{i(\vec{k}\vec{r}-\omega t)} \tag{4.1}$$

where A is the amplitude of the wave, $\vec{k}$ is the wave vector and $\vec{r}$ is the position vector, ω is the wave angular frequency and t is time. The modulus of the wave vector is $k = |\vec{k}| = 2\pi/\lambda$, where λ is the wavelength of the electromagnetic wave. The measured quantity is the intensity:

$$I \propto EE^* = |A|^2 \tag{4.2}$$

Let us consider the interference of two electromagnetic waves, that propagate in the same direction z: $E_1 = A_1 e^{i(k_z z-\omega t)}$ and $E_2 = A_2 e^{i(k_z z-\omega t+\Delta\phi)}$, where $\Delta\phi$ is the phase difference between two waves. The resulting field on the detector is the sum of all the fields and the intensity of the interference is:

$$I \propto (E_1+E_2)(E_1+E_2)^* = I_1 + I_2 + 2\sqrt{I_1 I_2}cos(\Delta\phi) \tag{4.3}$$

The expression for interference intensity consists of two terms: baseline – the incoherent sum of two wave intensities and modulation – the coherence term that depends on the phase difference.

The phase difference can be introduced by a delay in propagation between two interfering beams or by the difference in refractive index (difference in speed of propagation inside the material). The phase difference in this case is:

$$\Delta\phi = \frac{2\pi}{\lambda} OPD \tag{4.4}$$

where the optical path difference (OPD) in this case is:

$$OPD = n_1 L_1 - n_2 L_2 \tag{4.5}$$

where n and L are the refractive indexes and optical path of each beam.

4.1.2 Quasi-monochromatic interference

For the quasi-monochromatic light source, the expression of interferometric intensity needs to be modified. The resulting interference, in this case, is the sum of all interference patterns in an infinitely small spectral region $d\lambda$ over the wavelength spectrum:

$$I = \int_0^\infty \Big(I_1 + I_2 + 2\sqrt{I_1 I_2} cos(\Delta\phi(\lambda)) \Big) d\lambda \tag{4.6}$$

The first term is the sum of all incoherent power and the second one is the Fourier transform of the spectrum intensity. So the measured modulation intensity for a wide range of OPD can be used to reconstruct the optical spectrum of the source or, if data is insufficient, to estimate the coherent length in the case of the quasi-monochromatic source.

4.1.3 Mach-Zender interferometer

If the beam splitter at the input of the MZ interferometer divides power into equal parts $I_1 = I_2 = I_0/2$, so the expression above can be simplified:

$$I = \int_0^\infty I_0(\lambda) d\lambda + \int_0^\infty I_0(\lambda) cos(\frac{2\pi}{\lambda} OPD) d\lambda \tag{4.7}$$

In this chapter, I first use an all-fibered MZI, so the OPD is created with different lengths of optical fibers for each arm. The disadvantage of this method

is a coarse step in OPD and the advantage is that it doesn't require any optical alignment. Secondly, I improve the MZI setup and introduce free space collimators so the OPD can be finely adjusted and in real-time of the measurement.

4.2 Coherence characterization with an All-fibered Mach-Zehnder interferometer

In this part, I will present the coherence study of the DSR-like rectangular pulses using an all-fibered MZI. However, the MZI setup is firstly validated with a distributed feed-back laser as reported in the following sections.

4.2.1 All-fibered Mach-Zehnder interferometer setup

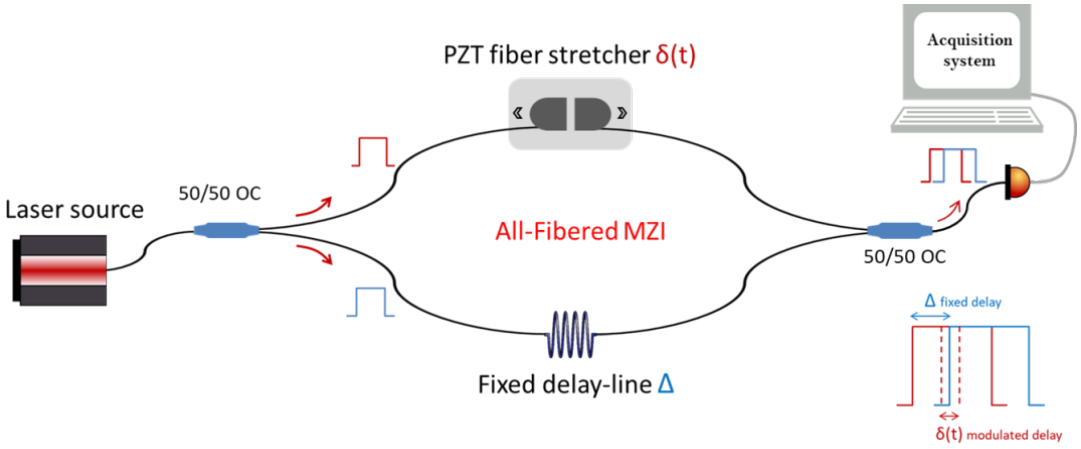

Figure 4.2: All-fibered MZI experimental setup

The experimental setup based on an all-fibered Mach-Zehnder interferometer used to characterize the temporal coherence of DSR-like pulses is illustrated in Figure 4.2. A 50% coupler placed at the output of the laser source splits the beam into two equivalent signals. One part propagates in an arm, which includes a fixed delay line $\Delta = 2\ m$ consisting of a simple SMF fiber. The second part of the signal propagates through a piezoelectric (PZT) fiber stretcher which superposes a modulated delay $\delta(t)$ around the fixed path difference Δ. The total path difference is then $\Delta + \delta(t)$. The path difference between the

arms noted as a fixed delay-line Δ is created with an additional optical fiber that can range from a few cm to a few meters and beyond. However, changing the length requires turning off the laser and splicing the fiber. Thus, the path difference Δ cannot be tuned in real time while the laser is running. The PZT-based fiber stretcher consists of two U-shaped polyethylene resin caps designed to wrap the optical fiber around. One of the caps is at rest while the other is mounted on a PZT translation stage driven by a function generator with a 200 Hz triangular function. Finally, both signals are recombined with a 50 % OC and the local temporal coherence can be studied.

4.2.2 Validation of MZI with DFB semiconductor laser

Before studying the coherence of rectangular pulses, the MZI is tested and validated using a distributed feedback (DFB) laser as a continuous-wave laser source emitting at a wavelength of 1556.5 nm.

DFB laser coherence study with MZI

Figure 4.3(a) represents the optical spectrum of the DFB laser and figure 4.3(b) exhibits the temporal trace of the signal at the output of the MZI.

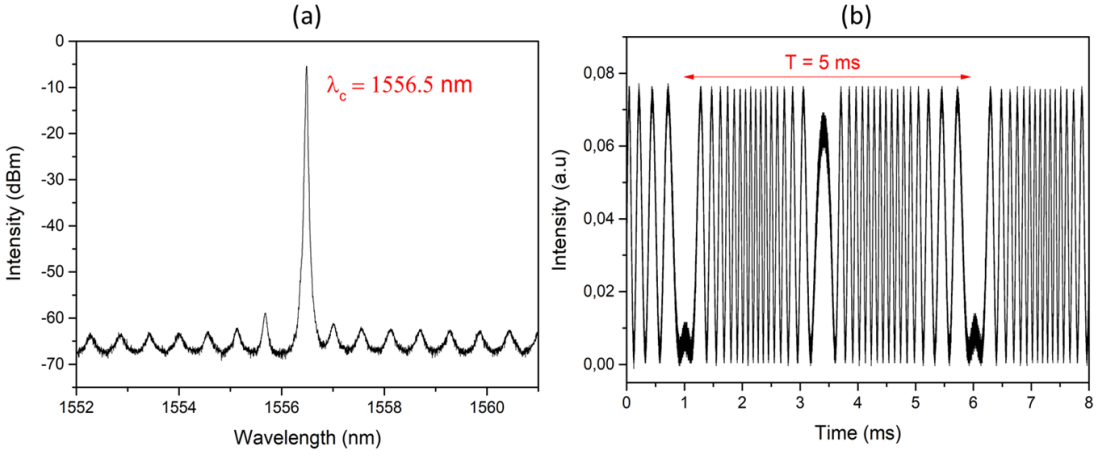

Figure 4.3: (a) Optical spectrum trace of the DFB laser source. (b) Temporal trace of interferometric fringes of the DFB laser at the output of the MZI.

The temporal trace shows the interferometric fringes with high contrast.

The period $T = 5\ ms$ corresponds to the modulation delay $\delta(t)$ performed by the PZT fiber stretcher driven by a 200 Hz triangular function generator. The temporal curve is not a perfect sine as expected for a continuous linear phase variation. Phase changes are localized at every minimum and maximum of the triangular function, at about 1 ms, 3.5 ms, and 6 ms, which causes an inhomogeneous response of the fiber to the PZT fiber stretcher. Except for these phase changes, the MZI is operational and could be used to measure the coherence of more complex laser regimes. From figure 4.3(b) we note about 33 fringes for one period of PZT modulation so that a 2π-phase delay between the two arms of the interferometer corresponds to about 150 μs. The period of the interferometric fringes is about 100 times the round-trip time of the cavity (1.45 μs). Therefore, the interferometric fringes will not be visible along one rectangular pulse but will modulate a large number of pulses. Figure 4.4 is a schematic representation of the expected temporal intensity evolution of the rectangular pulses in the fiber laser at the MZI output, in the case of coherent and incoherent pulses.

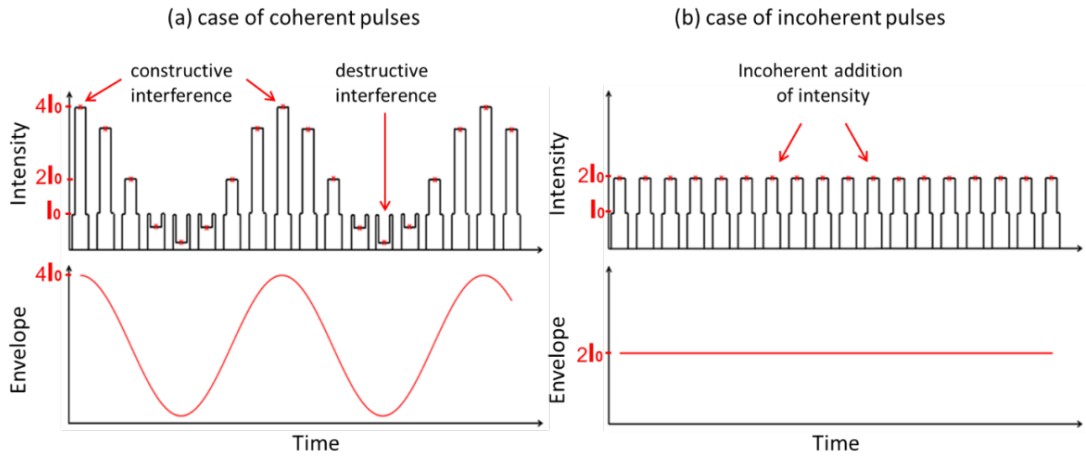

Figure 4.4: Schematic temporal evolution of the pulse intensity and the envelope, in case of (a) coherent pulses and (b) incoherent pulses.

In the case of coherent pulses, it is expected that the intensity of interfering beams will experience a sinusoidal evolution corresponding to constructive and destructive interference, as observed for the DFB laser. So, when we measure

the intensity of the top center of each two interfering pulses (see red crosses in the upper curve of figure 4.4(a)), the resulting curve would be sinusoidal, as shown in the same figure (lower red curve of figure 4.4(a) representing the intensity envelope versus time). Alternatively, in the case of incoherent pulses, the intensity reached by the interfering part of each pulse remains constant, i.e., as the pulses are not coherent, the resulting intensity is merely the sum of intensities of the random interfering pulses, as depicted in figure 4.4(b). In the next section, I try to reproduce coherent square pulses by externally modulated DFB, to have a first approximation of the expected interference signal in the mode-locked fiber laser.

4.2.3 Direct modulation of the DFB semiconductor laser

In this section, the DFB semiconductor laser is modulated with an external function generator. The aim is to create rectangular pulses to imitate DSR pulses in terms of temporal coherence. The MZI is then used to characterize their coherence and visualize real-time interferometric fringes on the oscilloscope. It permits to have a preliminary study of the eventual interferometric temporal trace of the experimental DSR-like rectangular pulses regime.

The experimental setup is the same as in figure 4.2, but with an additional function generator used to externally modulate the DFB laser source. Well-defined square functions are generated with a precise frequency. The modulated DFB signal is then connected to the MZI. The figures below show the temporal and spectral traces of the modulated DFB laser at the output of the laser, and at the output of the MZI, for different modulation frequencies. Figure 4.5a represents the temporal trace of the modulated DFB at the output of the laser. The output pulsed signals represented in black, red, blue, and magenta curves are modulated with 500 Hz, 10 kHz, 40 kHz, and 50 kHz, respectively. As can be observed in the figure, the more the modulation frequency is high, the more the signal is altered. Indeed, comparing the black signal modulated at 500 Hz and the magenta signal modulated at 50 kHz, one can note that the black curve is clearer with higher intensity than the magenta curve. In parallel,

figure 4.5b represents the corresponding optical spectra for each modulation frequency. Even if the spectral trace is not representative of the spectrum of the DFB continuous wave because of the intrinsic limits of the OSA, we can note that after external modulation of the DFB laser, the optical spectrum is altered compared to the initial spectrum (see figure 4.3(a)) and became wider. The signal alteration after external modulation of DFB laser is widely studied since it can cause a spectral broadening, mode-hopping, and frequency shift [49–51].

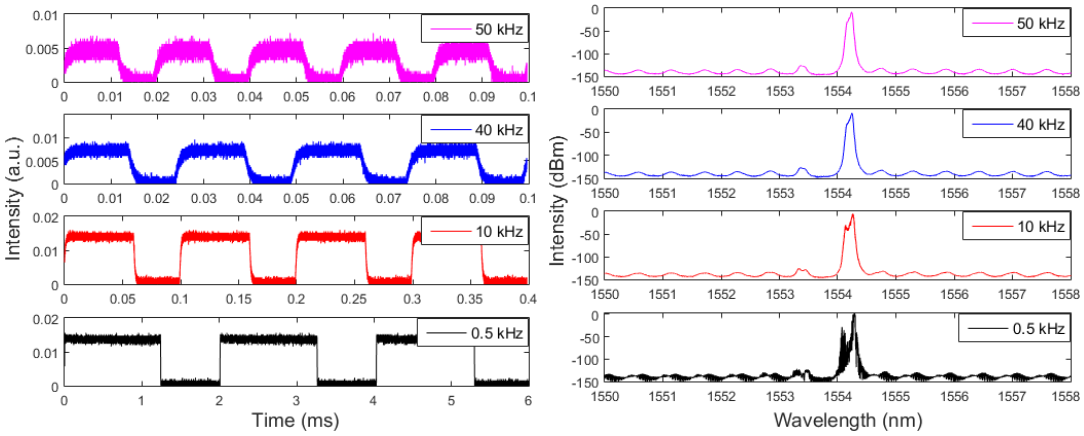

(a) (b)

Figure 4.5: (a)Temporal trace of the modulated DFB laser at the output of the laser, and (b) the corresponding optical spectrum trace, for different modulation frequencies: 0.5 kHz, 10 kHz, 40 kHz, and 50 kHz.

As explained above, modulated DFB aims to imitate the real DSR rectangular pulses which are coherent, and study their coherence with the MZI, to have a comparison reference for an eventual DSR generation in the fiber laser cavity. The signals represented in figure 4.5 are then injected into the MZI. It is worth mentioning that the PZT fiber stretcher is switched OFF, and it behaves like static fiber without any stretching. Hence, the MZI is characterized by a constant optical path delay $\Delta = 2\ m$, and with $\delta(t) = 0$ The interferometric result at the output of the MZI is depicted in figure 4.6.

The temporal trace is shown in figure 4.6a and displays fine modulations within the rectangular pulse envelopes. However, these modulations do not

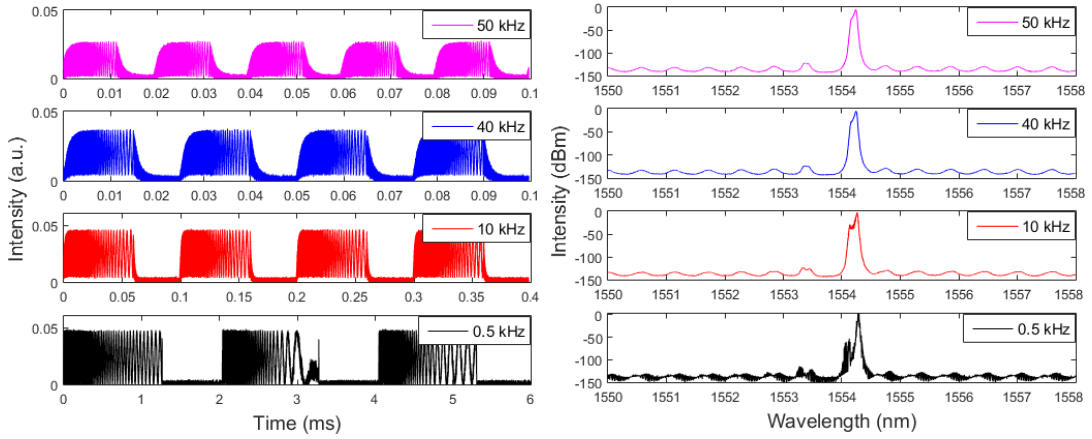

(a) (b)

Figure 4.6: Temporal trace of the modulated DFB laser at the output of the MZI (a), and the corresponding optical spectra (b), for different modulation frequencies: 0.5 kHz, 10 kHz, 40 kHz, and 50 kHz.

correspond to the PZT fiber stretcher-induced interferometric fringes as the PZT is turned-off. Also, one can note that the modulations are very fast in the first half of each rectangular pulse and slower in the second half of the pulse. This is probably due to the switch-on/off transition effect of the laser under the direct modulation, wherein the second half of the square pulse the modulations are slower as the temperature of the laser diode is stabilized. Afterward, the same measurements are made at the output of the MZI, with the PZT fiber stretcher switched on. As predicted in section 3, it is expected to see interferometric fringes as depicted in figure 4.3(b). The result is shown in figures 4.7 and 4.8. The signal is measured first at the output of the laser. The temporal trace and the corresponding optical spectra are depicted in figure 4.7a, and figure 4.7b, respectively, for modulation frequencies of 10 kHz and 50 kHz. The signals are identical to those depicted in figures 4.5a and 4.5b.

Then, the interferometry of the signals is studied with the MZI where the PZT fiber stretcher which is externally modulated at 200 Hz is turned on. The resulting signals are shown in figure 4.8.

The temporal trace, depicted in figure 4.8a, reveals modulations within the rectangular envelope. However, they are not the expected interferometric

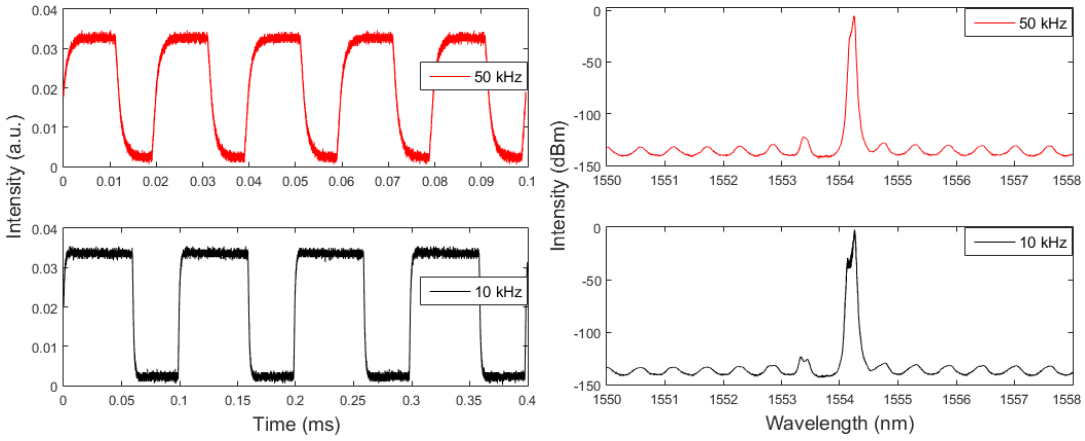

(a) (b)

Figure 4.7: Temporal trace of the modulated DFB laser at the output of the laser (a), and the corresponding optical spectrum trace (b), for modulation frequencies of 10 kHz, and 50 kHz.

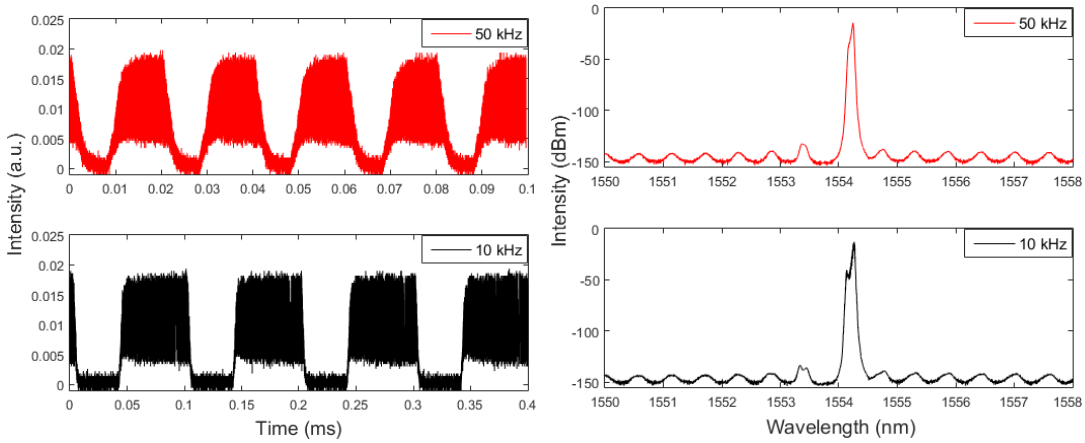

(a) (b)

Figure 4.8: Temporal trace of the modulated DFB laser at the output of the MZI (a), and the corresponding optical spectrum trace (b), for modulation frequencies of 10 kHz, and 50 kHz.

fringes which would be due to the PZT fiber stretcher. Indeed, these modulations are very fast, and even faster than those of figure 4.6a. Hence, the PZT fiber stretcher had just amplified the phenomenon observed in figure 4.6a. Because of these fast modulations, created within each rectangular envelope, it is not possible to see the interferometric fringes induced by the PZT fiber

stretcher as it was aimed in this section. The modulation phenomenon occurs because of the direct modulation of the DFB. By launching the signal into the MZI, this latter amplifies the occurring phenomenon. In a paper published in 1985 [52], Haney et al. measured the temporal coherence of pulsed single-mode laser diode. Under high-speed pulsed modulation, the temporal coherence is affected by instabilities in the lasing wavelength caused by the transient phenomena in the junction region of the laser. These instabilities are identified to be junction heating during the pulse causing a continuous shift in the lasing wavelength with time and mode-hopping in which the laser switches between two adjacent longitudinal modes during the pulse.

Consequently, trying to mimic DSR pulses by direct modulation of the DFB laser was not helpful in our case and didn't permit the expected preliminary study. Nevertheless, in the next section, I will present the coherence characterization results of the DSR-like square pulses generated in a fiber ring laser cavity.

4.2.4 Coherence characterization of rectangular pulses

In this section, a temporal coherence characterization of rectangular pulses, generated by the passively mode-locked fiber laser, is performed. A single-mode fiber (SMF) and dispersion-shifted fiber (DSF) are utilized as a fiber coil in the laser cavity (see figure 4.9 below). Let us note that this regime is studied in section 3.3 of chapter 3, to optimize the conditions for producing DSR rectangular pulses. Here we use the studied pulses to investigate their temporal coherence. This study is conducted in the following parts 4.2.4(a), and 4.2.4(b). In each part, the characteristics of the rectangular pulses are reminded, then the temporal coherence is performed by using the MZI.

(a) Single-mode fiber-based laser cavity

Herein, an SMF coil is used in the laser cavity. The total cavity length is about 304 m corresponding to a round-trip time of 1.52 μs. The temporal

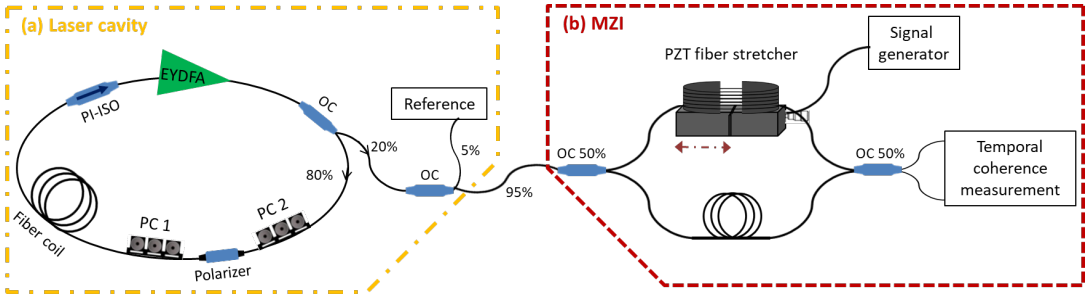

Figure 4.9: Experimental setup. EYDFA, Erbium-Ytterbium co-doped fiber Amplifier; OC, optical coupler; PC, polarization controller; SMF, single-mode fiber; PI-ISO, polarization-insensitive isolator; PZT, Piezoelectric translator; MZI, Mach-Zehnder interferometer

trace, depicted in figure 4.10a, represents one pulse per cavity round-trip time. The corresponding optical spectrum, depicted in figure 4.10b has a bandwidth of 9.25 nm, but its pedestal is relatively large. As mentioned before, in the

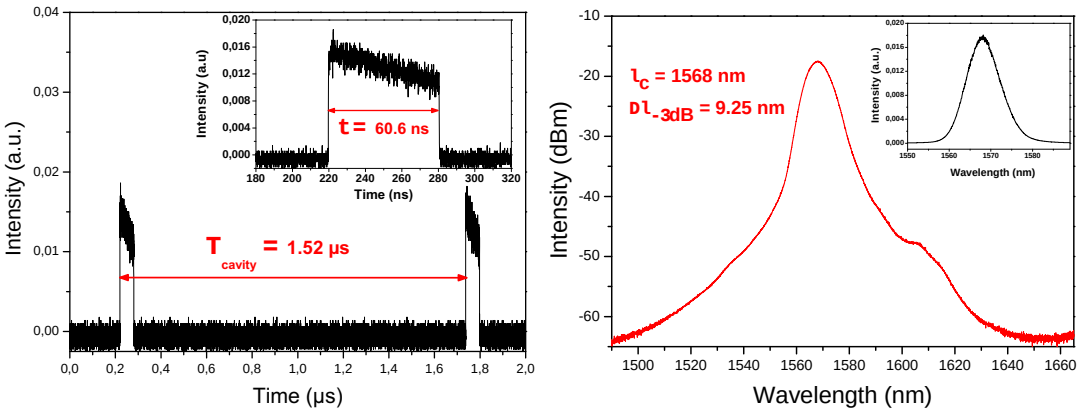

(a) (b)

Figure 4.10: (a) Temporal trace of rectangular pulses, (b) the corresponding optical spectrum, at the pump power of 5.06 W.

literature of the experimental DSR regime, the verification of the features such as a linear increase of pulse width and pulse energy, a constant peak power, and an invariant optical spectrum with the pump power, was sufficient to affirm that the pulses are DSR. However, for a relevant conclusion, it is necessary to verify the temporal coherence of the pulses. The result of MZI is shown in the figures below. Figure 4.11a displays the rectangular pulse at the pump

power of 5.06 W, with a pulse width of 60.6 ns, at the reference output of the laser cavity. This pulse propagates through the MZI which is characterized by a path difference of 2 m, corresponding to a time delay of 10 ns. The resulting pulse interference is shown in figure 4.11b and exhibits an incoherent addition of intensities in the cross-region. However, as the interferometer is modulated with a PZT fiber stretcher at 200 Hz, we need to make a zoom out on many pulses for at least a few ms, to see if there is modulation as displayed in figure 4.3(b) of the temporal interference of DFB. Figure 4.12a

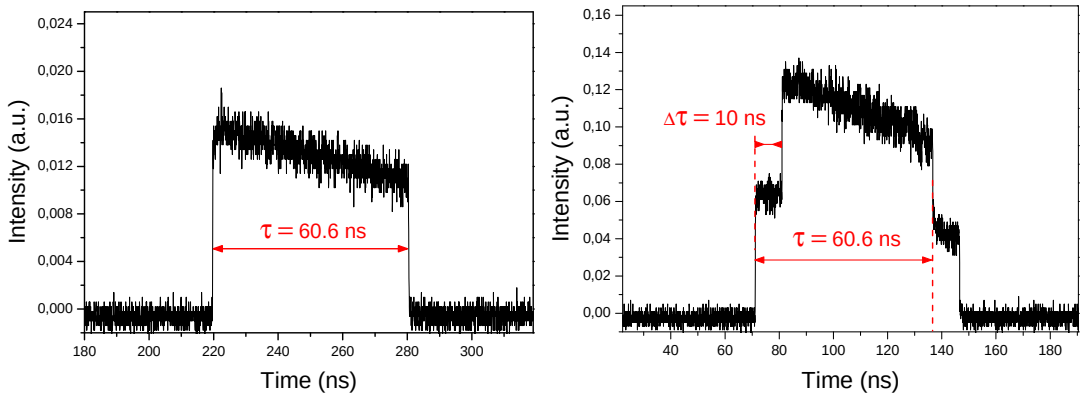

(a) (b)

Figure 4.11: (a) Temporal trace of the initial pulse at the output of the laser for a pump power of 5.06 W, and (b) the corresponding temporal trace at the output of the MZI in which this pulse interferes with itself with 2 m of path difference (corresponding to 10 ns time delay).

shows a zoom out of 4 ms of the rectangular pulses at the output of the MZI. The top envelope of all the pulses seems to have a constant value and no visible sine-evolution as seen in the case of the DFB laser interference. However, to have an accurate measurement, we extract the value of the top center of the interfering region of each pulse (see the scheme of figure 4.4). The result is shown in figure 4.12b and attests of a constant value along all the interfering parts of the pulses, which is an incoherent addition of intensities. The result corresponds to the case of incoherent pulses of figure 4.4(b). Thus, these pulses are temporally incoherent. This demonstrates that each rectangular pulse is just a packet of non-resolved fine structures. Thus, even if most of the features

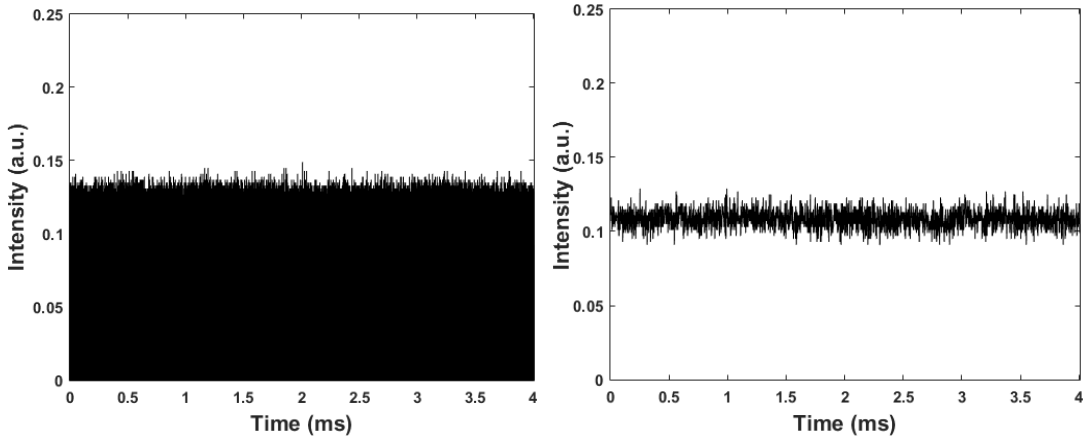

(a) (b)

Figure 4.12: MZI result at the pump power of 5.06 W. (a) Temporal trace of several pulses along 4 ms, at the output of the MZI. (b) The corresponding temporal envelope consists of the top intensity of each interfering part of the pulse.

of the DSR regime are verified, as the pulses are not temporally coherent, this regime cannot be considered as a DSR regime. Besides, although there are many features of DSR which are verified with this regime, there may be few indications that these pulses are not DSR except the coherence study. These indications are the wide pedestal spectrum (see figure 4.10b) which indicates an eventual tendency to a noise-like regime, and the non-flattop temporal profile which may be an indication of different wavelengths with a close group velocity. In the next section, another regime of rectangular pulses is studied with DSF coil in the laser cavity.

(b) Dispersion-shifted fiber-based laser cavity

In this section, the rectangular pulses regime is studied with a slightly different laser cavity. The aim is to look for a more stable regime. Here, a DSF with different dispersion characteristics than the SMF is used. As studied in section 3.3 of chapter 3, the characteristics of the rectangular pulses are verified. The temporal profile is shown in figure 4.13a and the optical spectrum in figure 4.13b. The signal is measured at a pump power of 5.06 W. Here again, we can

see that the optical spectrum trace has a wide pedestal.

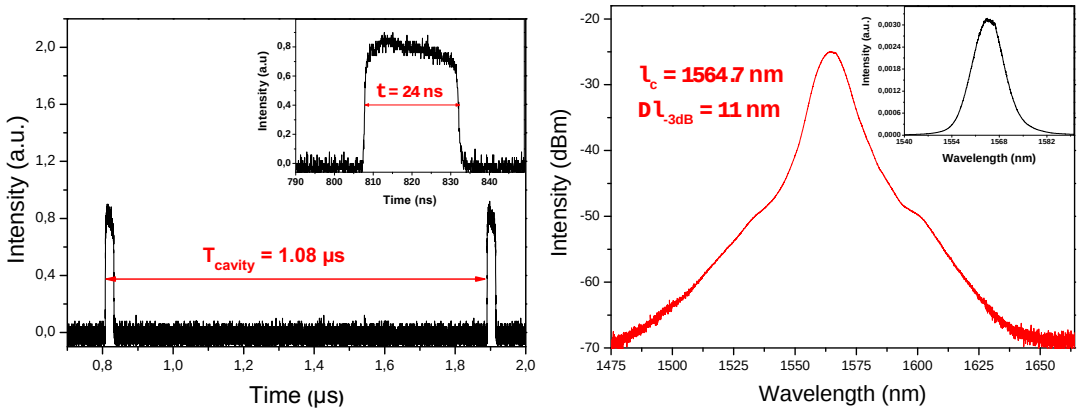

(a) (b)

Figure 4.13: Temporal trace of rectangular pulses (a), and the corresponding optical spectrum (b).

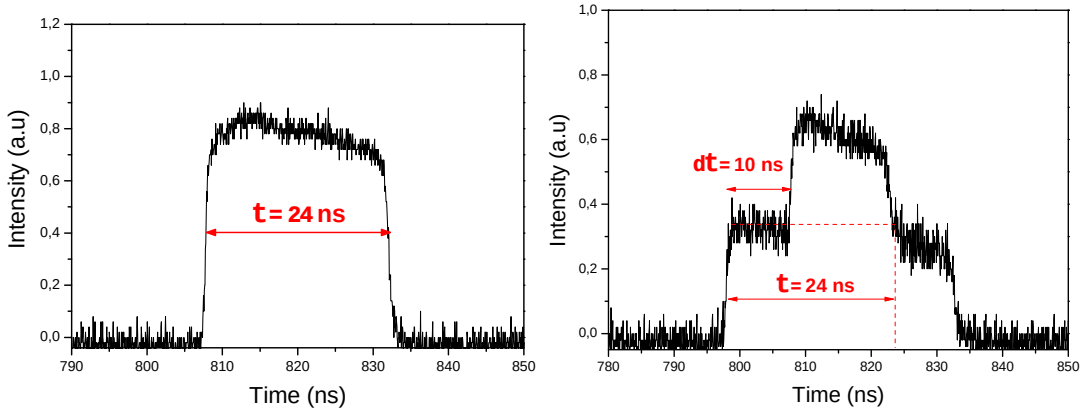

(a) (b)

Figure 4.14: (a) Temporal trace of the initial pulse at the output of the laser for a pump power of 5.06 W, and (b) the corresponding temporal trace at the output of the MZI in which this pulse interferes with itself with 2 m of path difference (corresponding to 10 ns time delay).

The same interferometry measurement is made with these pulses. Figure 4.14a represents the pulse at the output of the laser at 5.06 W of pump power. Figure 4.14b represents the superposition of the pulse with itself at the output of the MZI with a path difference of 2 m which corresponds to 10 ns. The coherence study is performed by measuring the intensity envelope of thousands

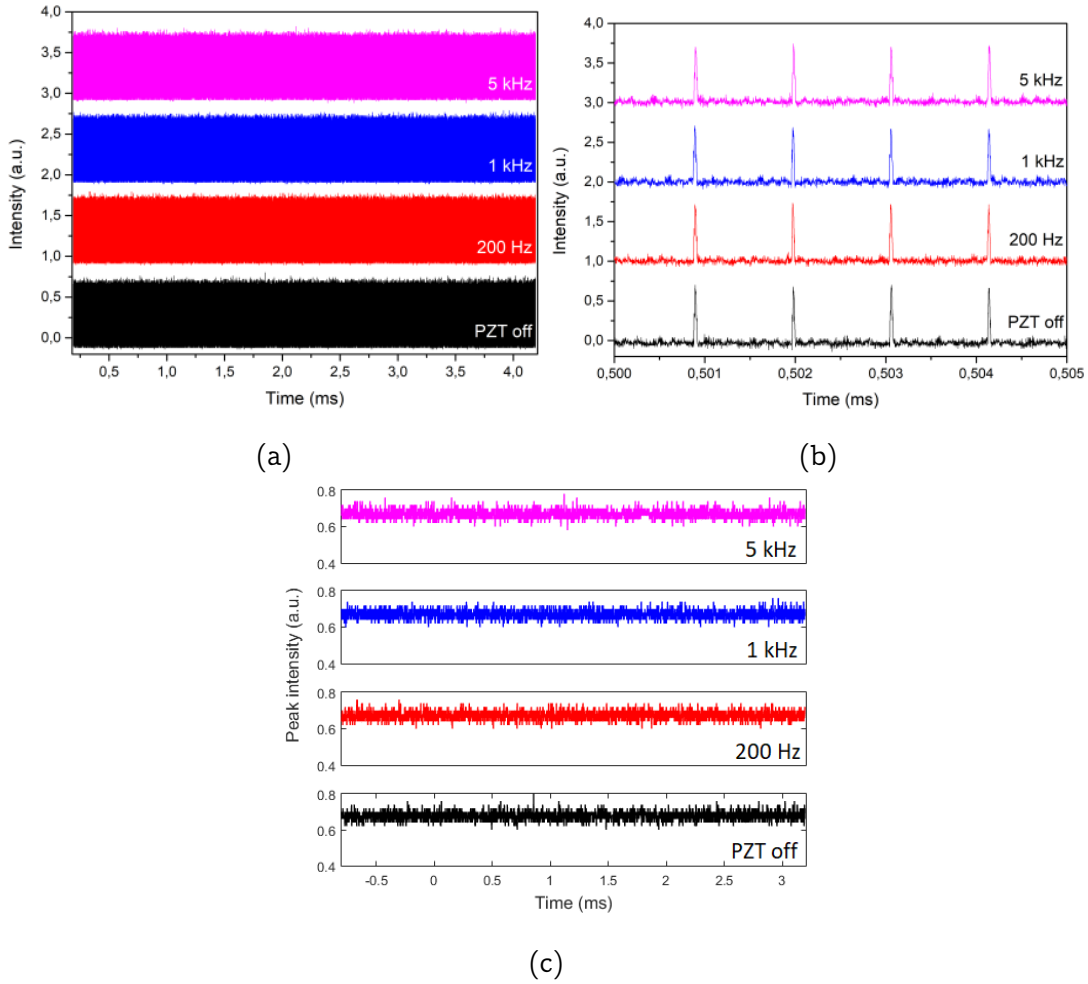

Figure 4.15: (a) Temporal traces of the rectangular pulses at the output of the MZI (b) a zoom-in on the square pulses, (c) the temporal envelope consisting of the top intensity of each interfering part of the pulse..

of pulses at the output of the interferometer. Figure 4.15 shows the interferometry result for different modulation frequencies of the PZT. The interferometric temporal trace is shown in Figure 4.15a. For more precise measurement, the interferometry temporal traces have been recorded while the PZT is turned off and for three different values of the modulation frequency when it is turned on: 200 Hz, 1 kHz, and 5 kHz.

Figure 4.15b represents a zoom-in, from 0.5 ms to 0.505 ms. The corresponding intensity envelopes are depicted in Figure 4.15c and show a constant value for each modulation frequency so the studied rectangular pulses are incoherent.

These previous interferometry studies are performed using an all-fibered MZI. As specified before, it is difficult to make a very short delay between the interferometer arms. In the coming study, the MZI is slightly modified to be able to rich a zero delay and thus make a superposition of one pulse with itself.

4.2.5 Conclusion

In this section, I have studied the temporal coherence of the DSR-like rectangular pulses generated in a passively mode-locked fiber ring laser cavity. At the first glance, the pulses seem to obey to the features of DSR pulses. However, the MZI reveals that the rectangular pulses are not temporally coherent but may consist of multiple random fine structures within the rectangular envelope. It is worth mentioning anyway that the studied pulses are characterized by an optical spectrum that has a large pedestal, even if it is invariant when the pump power is increased.

4.3 Coherence characterization with an MZI including free space collimators

4.3.1 Experimental setup

The optimized MZI setup is shown in Figure 4.16. Free-space collimators L1 and L2 are inserted in one of the arms of the interferometer. Fixed on translation stages (TS), the free-space collimators permit a fine adjustment of the path difference which can be set from zero to a few hundreds of μm while in an all-fibered interferometer, such small path differences are very difficult to reach because of the fiber splice.

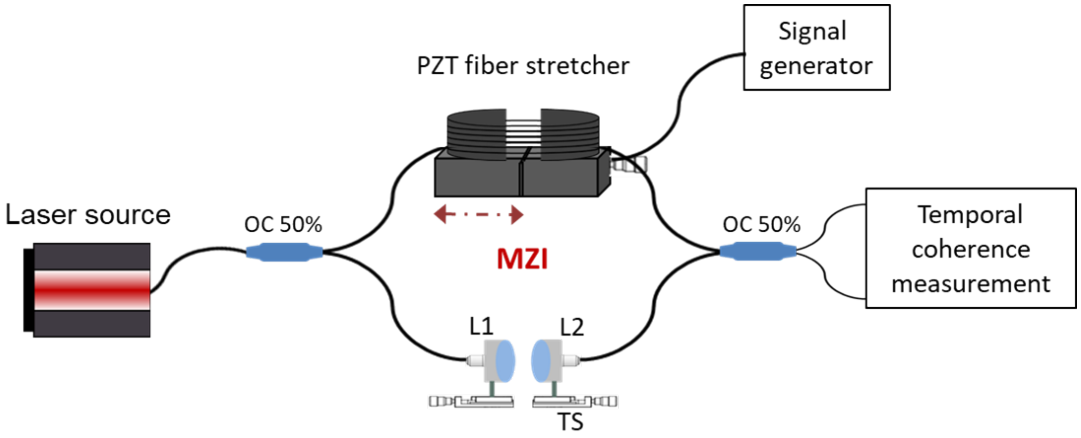

Figure 4.16: MZI. OC: optical coupler, PZT: Piezoelectric translator, L1,2: lens, TS: translation stage.

4.3.2 Coherence measurement of rectangular pulses with MZI

The studied rectangular-shaped pulses are depicted in figure 4.17. It is the same regime studied in section 3.3 of chapter 3. The temporal pulse trace is given in figure 4.17(a), obtained at the pump power of 1.67 W. There is one pulse per cavity round-trip time, with a pulse width of 26.5 ns, as shown in the inset of figure 4.17(a). The corresponding optical spectrum is centered at a wavelength of 1612 nm as shown in figure 4.17(b). The spectral -3 dB bandwidth is 9.2 nm.

Using the MZI in which are inserted the free space collimators, a relevant measurement of the temporal coherence is performed. The results are presented in figures 4.18 and 4.20. Figure 4.18(a) represents the interferometric fringes of the square pulses with 26.5 ns pulse width, obtained at a pump power of 1.67 W, for different fixed optical delays $\Delta(\approx 0, \approx 100, \approx 200$, and $\approx 300\ \mu m)$. For a fixed delay of $\Delta \approx 0\ \mu m$, i.e., when the path difference is nearly zero, the interferometric fringes are visible with relatively high contrast. When Δ increases to 100 μm and 200 μm the contrast of the fringes decreases and disappears for $\Delta \approx 300\ \mu m$. Figure 4.18(b) represents the corresponding peak intensity (envelope) traces for each value of path difference. Considering

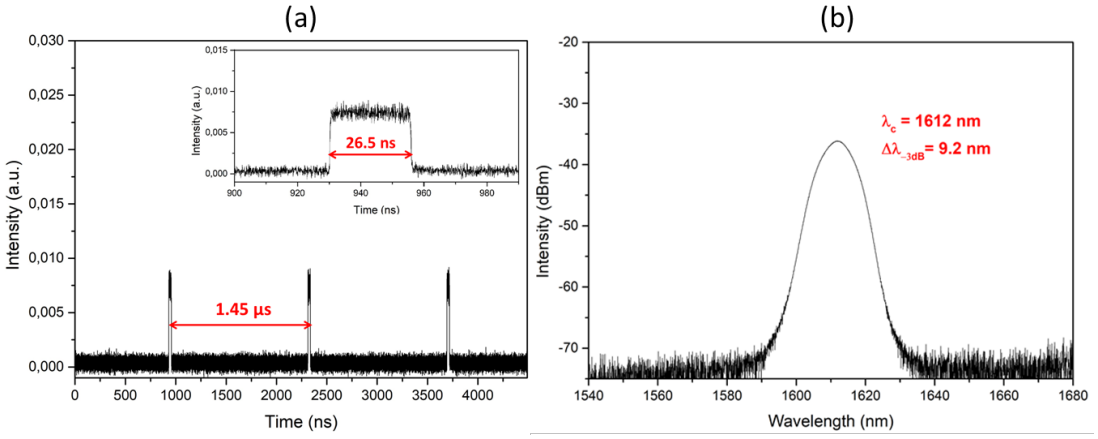

Figure 4.17: (a) Temporal trace of rectangular pulses, and (b) the corresponding optical spectrum at the pump power of 1.67 W.

the discontinuities introduced by the fiber response to the stretching and the discontinuities caused by the triangular function which modulates the PZT fiber stretcher, we can see that for $\Delta \approx 0\ \mu m$, the contrast of the fringes is high and mimics the sine function as it is expected in the schematic of figure 4.4(a). When increases, the contrast of interferometric fringes decreases. For $\Delta \approx 300\ \mu m$, the fringes completely disappear as in the case of incoherent pulses as shown in figure 4.4(b), where the peak intensity is constant versus time.

The same measurements are made for different pulse widths. For example, I plot the results obtained at a pump power of 4.02 W, for a pulse width of 69 ns whose temporal trace is depicted in figure 4.19 below. The interferometric results are shown in figure 4.20. Same as in figure 4.18 we notice a relatively high contrast for $\Delta \approx 0\ \mu m$, but the coherence pattern disappears when Δ is around 300 μm.

From figures 4.18 and 4.20, we conclude that when the path difference $\Delta \geq 300\ \mu m$, corresponding to a time delay of $\tau = 1\ ps$, the interferometric fringes completely disappear. It means that the square pulses are not coherent and consist of picosecond pulses within the square envelope. The duration of these pulses is estimated to be in the order of a ps.

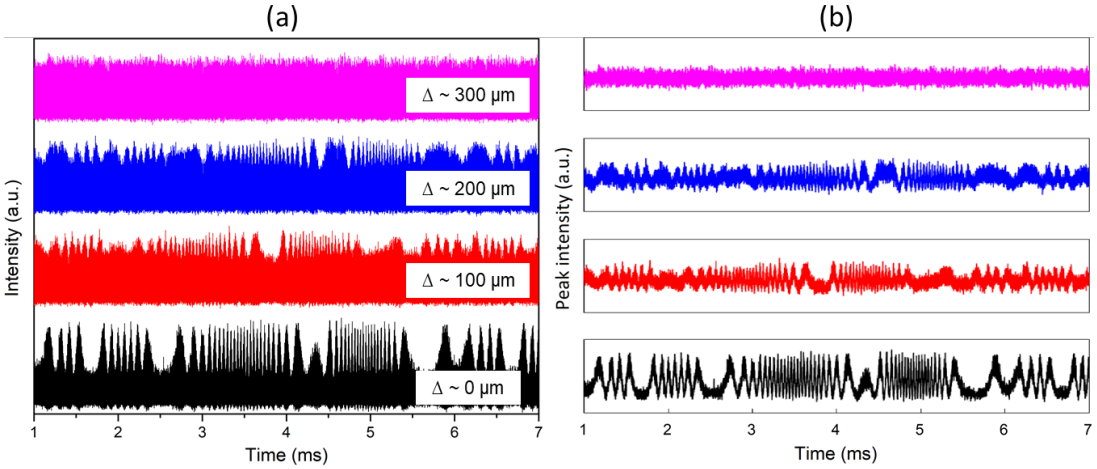

Figure 4.18: (a) Temporal evolution of the interferometry fringes of the 26.5 ns pulses at the pump power of 1.67 W, for different optical delays (ranging from 0 μm – 300 μm), at the output of MZI. (b) The corresponding peak intensity evolution.

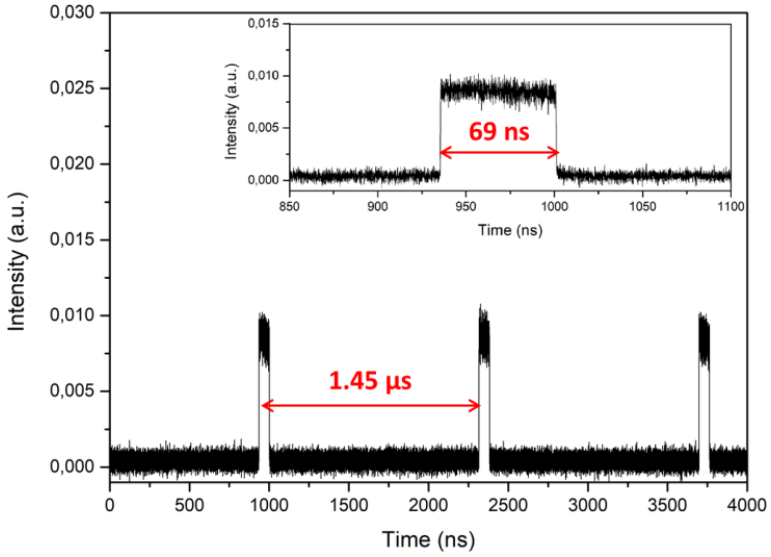

Figure 4.19: Temporal trace of rectangular pulses at the pump power of 4.02 W.

4.3.3 Conclusion

By inserting the free-space collimators in the MZI, it was possible to superpose one pulse with itself with no any delay. Thus, with zero path difference, it was possible to visualize the interferometric fringes. Afterward, the delay is tuned

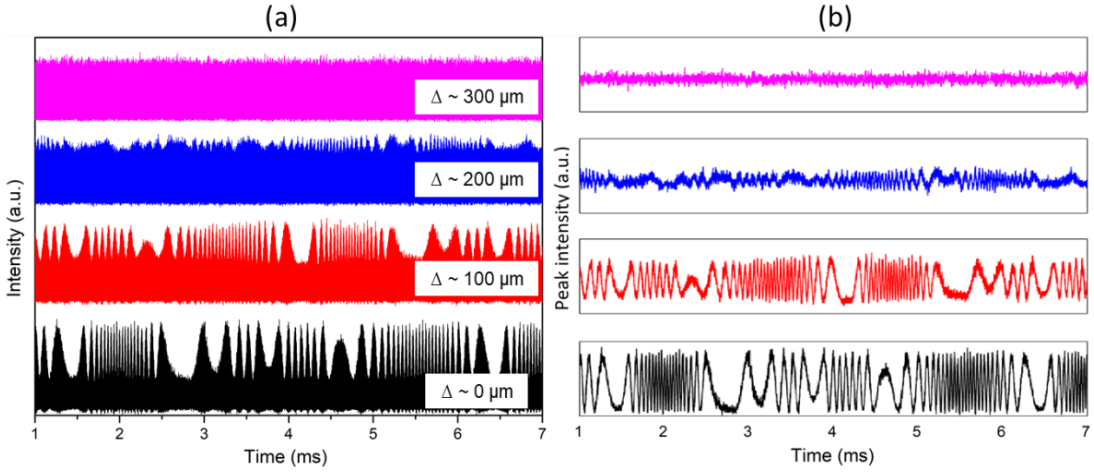

Figure 4.20: (a) Temporal evolution of the interferometry fringes of the 69 ns pulses at the pump power of 4.02 W, for different optical delays (ranging from 0 μm – 300 μm), at the output of MZI. (b) Intensity envelops of the interferometry fringes.

in real-time, and the fringes are still visible until the path difference reached about $\Delta \approx 300\ \mu m$. The studied pulses are not coherent, so they are not DSR pulses even if all their other characteristics seem to be as those of the DSR pulses.

4.4 Conclusion

In this chapter, I studied the temporal coherence of the DSR-like rectangular pulses in a passively mode-locked fiber laser, using a Mach-Zehnder interferometer. First of all, I used a distributed feed-back laser as a laser source in order to validate the well functioning of the MZI. Then, I reshaped the DFB laser to a rectangular pulsed DFB with direct modulation using a function generator. This attempt didn't work as the direct modulation affected the DFB functioning. However, as the MZI has been validated, I studied the coherence of the rectangular pulses generated by the fiber laser. In the first study, I used an all-fibered MZI, where the OPD tuning is limited by fiber splicing. The MZI is then optimized by inserting free-space collimators in one arm in order to easily

tune the OPD.

Consequently, I demonstrated that although the obtained rectangular pulses show most of the DSR pulse features, they are not necessarily DSR but may be packets of shorter pulses. With this method, I scan a short part of the rectangular pulse, so the coherence measurement is local. It is possible to adjust the delay Δ with the free-space collimators and scan different parts of the pulse as shown previously for different path difference Δ (≈ 0, ≈ 100, ≈ 200, and ≈ 300 μm). However, the studied pulses have a spatial extension of a few meters, and it is not possible to create such delays with collimators. To extend the study, other measurements are made by employing a long fiber coil as a dispersive medium. Thus the effect of the GVD could allow more global coherence characterization. By studying the shape evolution of the whole pulse after propagating along a fiber coil, it is possible, I attempt to discriminate between coherent and incoherent rectangular pulses. The results do not permit a precise conclusion, however, the technique represents a relevant perspective to explore. The results are shown in the appendix A. In the next chapter, I investigate a multiwavelength composite-state soliton regime.

Chapter 5

Multi-wavelength composite-state soliton generation in double-clad Er:Yb co-doped fiber laser

Multi-wavelength erbium-doped fiber lasers (MWFL) are of great interest for their various applications such as Wavelength Division Multiplexing (WDM) transmission systems [53, 54], fiber sensing [55, 56], signal processing [57], spectroscopy [58], and microwave generation [59]. However, since Er-doped fiber (EDF) is a gain medium that exhibits a homogeneous line broadening at room temperature, the EDF-based lasers often undergo strong mode competition tending to one wavelength oscillation and unstable multi-wavelength lasing. To solve this problem, many approaches have been proposed. In 1992, Park et al. demonstrated for the first time, a multiple wavelength operation in an Er-doped fiber laser, using a grating wavelength division multiplexer [60]. Other viable solutions include cooling the EDF to liquid nitrogen temperature [61, 62], using specially designed Er-doped two-core fiber to provide inhomogeneous gain through microscopic spatial hole burning [63], utilizing highly nonlinear fiber (HNLF) and high nonlinear photonic crystal fiber in the laser cavity [64–66], and using a frequency shifter or phase modulator [67–69]. Other methods consist of the use of optical feedback and nonlinear gain in optical fiber [70, 71], or using HNLF and Fabry-Perot filter for inhomogeneous loss mechanism

[72]. All these methods exploit the nonlinear filtering effects of the cavity thus enabling the multi-wavelength oscillation such as the generation of double-lobe wavelength oscillation [73]. Furthermore, by controlling the linear intracavity loss, a wide tunable erbium-doped fiber lasers (EDFL) covering (C+L)-band based on a C-band amplifier has been demonstrated [74]. Besides the applications of MWFL in terms of wavelength, pulsed MWFLs attract attention for the composite state soliton regime that they can generate. In particular, multi-wavelength pulsed EDFL can provide an excellent platform for the generation of composite-state soliton regimes with various stable coexisting states by manipulating the laser cavity parameters. For instance, the coexistence of chaotic and regular soliton structures in fiber lasers has been theoretically predicted [75]. Tang et al. investigated experimentally the coexistence of two types of soliton shape based on dispersion management in a near-zero dispersion regime [76]. Then, Wang reported on the coexistence of bright pulses and dark solitons in Er-doped fiber laser with strong normal cavity dispersion [77]. Moreover, different soliton patterns inside the same signal can simultaneously coexist. In Ref [78], the coexistence of alternate crystal and liquid soliton phases was experimentally observed. Meanwhile, in an ultra-large net anomalous dispersion EDFL, the demonstration of the coexistence of strong and weak pulses has been reported [79]. In addition, the simultaneous generation of harmonic soliton molecules with rectangular noise-like pulses and the coexistence of high repetition rate harmonic mode-locking with noise-like pulse have been demonstrated [80]. In 2018, the coexistence of dissipative soliton and stretched pulse was also observed in a dual-wavelength Tm-doped fiber laser [81]. Very recently, the emission of multi-state solitons (soliton singlets and molecules) in a dual-wavelength EDFL laser has been reported by Liu et al. [73]. All these works were carried out in lasers operating with single or dual-lobe wavelength.

This chapter addresses the generation of a multi-wavelength regime with composite-state solitons in double-clad Er:Yb co-doped fiber laser based on both nonlinear filtering and linear loss management of the cavity [82].

5.1 Experimental setup

The experimental setup of the studied regime is illustrated in figure 5.1. It is an all-fibered unidirectional ring (UR) laser cavity enabling the mode-locked laser using nonlinear polarization rotation (NPR) mechanism [83]. The NPR is configured by a set of a polarizer and two polarization controllers (PC1 and PC2). The cavity includes a C-band double-clad co-doped Er:Yb 30 dBm fiber amplifier (EYDFA) from Lumibird company (KPS-BT2-C-30-BO-FA). A polarization-insensitive isolator (PI-ISO) is used to ensure the unidirectional propagation of the light. The total cavity length is about 304 m (which corresponds to a round-trip time of 1.52 μs). It consists of a 5 m of EYDFA, with -0.021 ps^2/m second-order dispersion, and 299 m single-mode fiber (SMF28) including 285 m fiber coil and the fiber of other optical elements, with second-order dispersion of -0.022 ps^2/m. The net cavity dispersion is about -6.683 ps^2. The formed signal is then extracted by a 1×2 optical coupler (OC) from the output port with an extracting ratio of 10 %. The laser output measurements are simultaneously monitored by an optical spectrum analyzer (Anritsu MS9740A, 0.6 μm-1.7 μm) with the highest resolution of 0.03 nm, a 13-GHz oscilloscope (Agilent infiniium DSO8130B) combined with two 12-GHz photo-detectors (TTI, Model TIA61200 O/E Converter), a high power integrating sphere (Thorlabs S146C), and an electronic spectrum analyzer (Rohde & Schwarz FSP Spectrum Analyzer 9 kHz to 13.6 GHz). A manually optical tunable filter (OTF) with a filter bandwidth of 0.5 nm and tuning range from 1500 to 1630 nm (SANTEC OTF 320) is inserted at the output of the cavity for wavelength-resolved measurements.

5.2 Build-up of triple lobe spectrum

Using the above-mentioned experimental setup to obtain a multi-wavelength operation, the experiment is carefully conducted based on the fact that the long cavity (304 m) could support narrow artificial filtering that facilitates

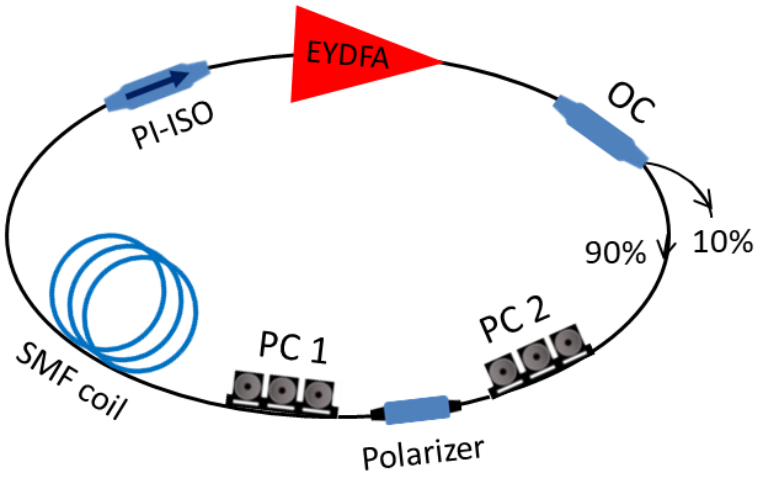

Figure 5.1: Experimental setup of an all-fibered unidirectional ring laser cavity: EYDFA, Er:Yb co-doped fiber amplifier; PI-ISO, polarization-independent isolator; SMF, single-mode fiber; PC, polarization controller; OC, optical coupler.

the multi-wavelength operation. In addition, the cavity loss is controlled to enhance the gain in L-band since the gain coefficient of EDF in the L-band is much lower than that in C-band [84–86]. Therefore, to have enough gain in both C- and L-bands, an optical coupler (OC) with a 10% extracting ratio is used in the laser cavity.

In the beginning, self-started mode-locking[87] was obtained at the pump power approaching 0.27 W. By appropriate adjustment of the PCs with further increasing the pump power from 0.27 W to 0.8 W, the spectrum has grown into a triple-lobe wavelength regime as depicted in figure 5.2a with a logarithmic scale and figure 5.2b in linear scale. Initially, at the pump power of 0.27 W, both the logarithmic and linear optical spectrums show two peaks located at 1567 nm and 1585 nm. These peaks are associated respectively with a continuous wave and soliton clusters with a narrow square shape as seen in the corresponding temporal trace (black curve in figure 5.2c). When the pump power is increased to 0.37 W, the triple-lobe wavelength regime starts to build up, where three distinct spectral lobes appear at ≈1567 nm, ≈1585 nm, and ≈1616 nm as depicted in figure 5.2a with a logarithmic scale. However, as the

wavelength lobe at 1616 nm is very weak, it cannot be seen on a linear scale (in figure 5.2b). The lobe centered at 1567 nm has evolved from a pure continuous wave (CW) to coexistence of CW and a soliton regime with Kelly sidebands, while the lobes centered at 1585 nm and 1616 nm are smoother. The so-called Kelly sidebands mainly occur in soliton mode-locked fiber lasers[88]. They are related to periodic instabilities due to the discrete and periodic loss and amplification in the laser cavity. By increasing the pump power to 0.6 W, the longest wavelength appears also in linear scale as represented by the blue curve in figure 5.2b. Finally, at the pump power of 0.8 W, the triple-lobe wavelength regime was completely formed, and different coexisting soliton patterns were observed on the oscilloscope. The three distinct lobes are well separated, and the wavelength separation between the shortest wavelength and the middle one is about 18 nm, while the separation between the middle and the longest one reaches 31 nm.

The physical process behind such spectrum dynamics is mainly attributed to the significant birefringence in the cavity which exhibits artificial spectral filtering, and to the intracavity linear loss that shifts the lasing to a longer wavelength (1616 nm). The oscillation threshold of about 0.27 W is reached first for wavelength-lobes at $\approx$1567 nm and $\approx$1585 nm due to compensation of the loss by the gain. The threshold level of about 0.37 W at $\approx$1616 nm is reached later because the gain in this spectral region is not enough at 0.27 W pump power. In the next section, the effect of the intracavity loss is investigated to understand its role in the multiwavelength generation.

5.3 Intracavity linear loss effect

To study the effect of intracavity linear loss and how it affects the regime, an optical attenuator was inserted in the cavity to introduce additional loss, Γ. This helps to control the number of wavelength lobes as shown in figure 5.3. Figures 5.3a and 5.3b represent the optical spectra at a given pump power, for different values of linear loss Γ, in logarithmic and linear scales, respectively.

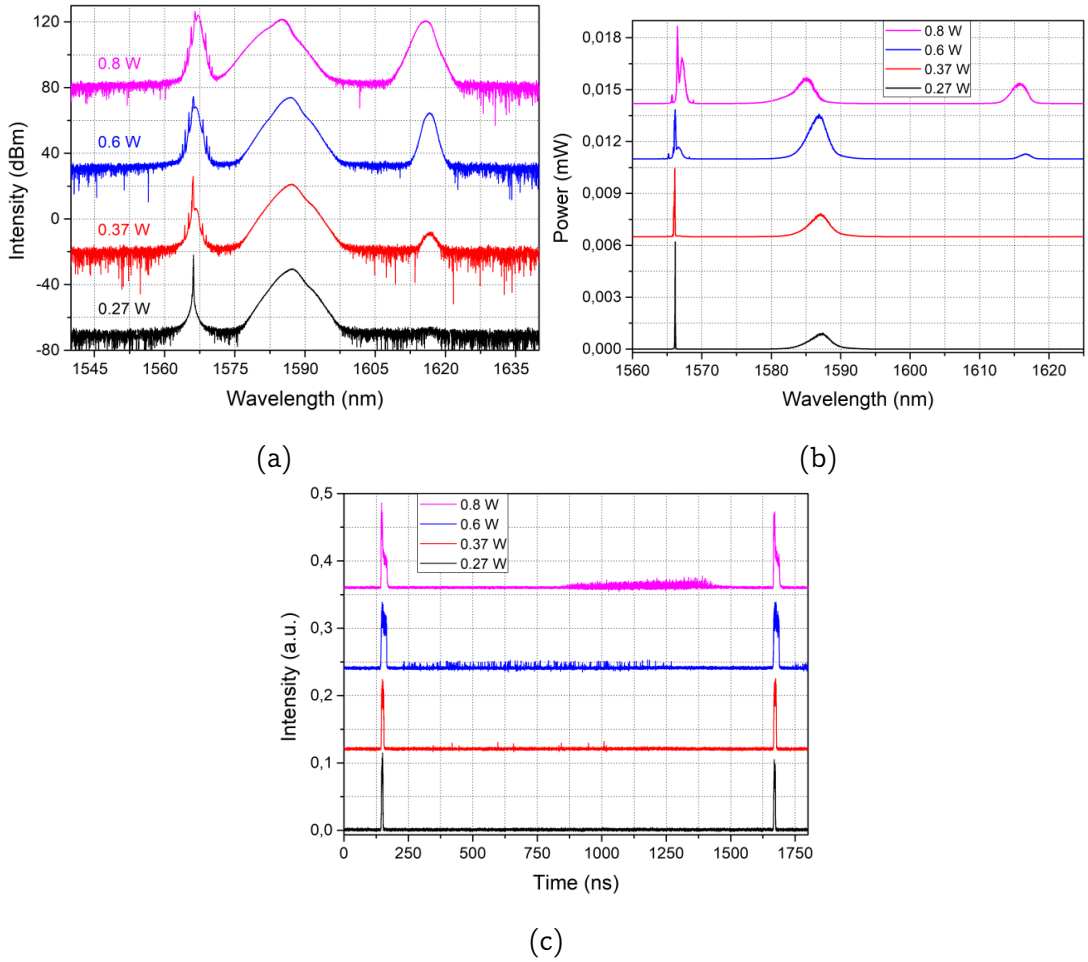

Figure 5.2: Evolution of the optical spectrum with a logarithmic scale (a), and a linear scale (b) at different values of pump power. (c) The corresponding oscilloscope trace.

For example, at $\Gamma = 0.3\ dB$, the spectrum depicted in the black curve exhibits three-wavelength lobes and the corresponding temporal trace in figure 5.3c represents three coexisting multi-soliton states. By introducing more loss in the cavity it is possible to suppress one of these wavelength lobes. Indeed, for $\Gamma = 0.5\ dB$ (red curve) as the loss is important; the longest wavelength in L-band is suppressed. In figure 5.3b where the spectrum is represented in linear scale, one can note in the red curve that the shortest wavelength lobe, centered at 1567 nm, is much more intense compared to that centered at 1585 nm. The corresponding temporal trace (cf. figure 5.3c) exhibits a larger soliton-like dispersive wave which almost fills the entire cavity. For linear loss $\Gamma = 0.4\ dB$, the

resulted signal is depicted in blue. The shortest wavelength was suppressed; the central and the longest wavelength lobes coexist in the cavity. The blue temporal trace in figure 5.3c shows a square soliton condensed phase with different intensity levels. The zoom-in, represented in figure 5.3d shows two connected squares; the highest one corresponds to the central lobe and the lowest corresponds to the wavelength-lobe centered at 1616 nm. One can note that the width of the first square increased comparing to the width of the red trace and this is compatible with the strength of the corresponding spectra (see central lobe in red and blue traces in figure 5.3b). This shows the contribution of each wavelength in the triple-wavelength spectrum as seen in the temporal trace of figure 5.3c. Finally, we can conclude from the experimental observations that when the linear cavity loss is relatively low, an oscillation wavelength can exist in L-band, in Er:Yb co-doped fiber laser. Also, the effect of the loss revealed a first approximation of the contribution of each wavelength. It seems that each lobe corresponds to a different temporal trace so that three different soliton states coexist in the cavity.

5.4 Pump power effect

In this section, the effect of the pump power on the characteristics of the presented laser regime has been investigated. Figures 5.4a and 5.4b illustrate the evolution of the spectrum, represented in both linear and logarithmic scales, respectively, for different values of the pump power. The corresponding temporal traces are presented in figure 5.4c, while the pulse width of the square pulses versus the pump power is depicted in figure 5.4d. When the pump power was increased from 0.8 W to 3.2 W, the spectrum presented in figure 5.4a reveals approximately the same shape and the triple wavelength lobes still coexist in the cavity. However, the linear scale representation (cf. figure 5.4b) reveals the changes more clearly while the pump power increases. The changes concern mainly the shortest (at 1567 nm) and longest (at 1616 nm) wavelength lobes which are getting more intense, while the central one (at 1585 nm) re-

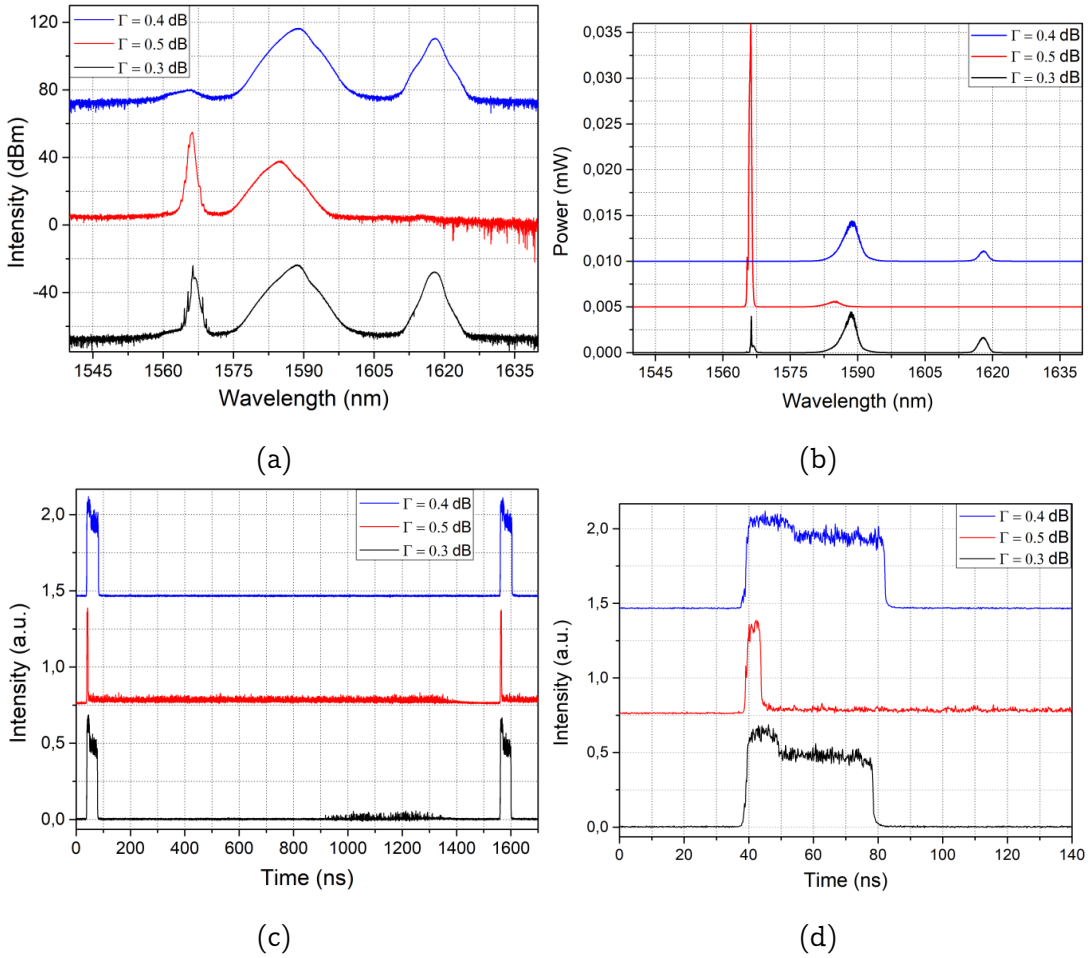

Figure 5.3: (a) Optical spectra at fixed pump power and for different intracavity loss in logarithmic scale and (b) in linear scale. (c) The corresponding temporal traces, with (d) a zoom in from 0 to 140 ns.

mains approximately at the same intensity level. At a pump power of 4.01 W, the spectrum located at 1567 nm becomes smoother with no sidebands and with important attenuation of the CW. The effect of the pump power is also visible on the corresponding temporal traces of figure 5.4c where the soliton bunch spreads over almost the whole cavity (cf. black, red, and blue curves) and the square pulses width changes. The variation of the square pulse width is quantified in figure 5.4d, where the pulse width has increased from 24.5 ns to 61.8 ns before 3.2 W, and then decreases to 32.8 ns at 4.01 W. Thus, the boost in energy reduces the square pulse duration and increases the number of pulses in the soliton bunch forming a high repetition rate harmonic of fine

soliton bunches with a period of ≈7.16 ns as shown in the inset of figure 5.4c. Figure 5.5 depicts the RF spectrum at the pump power of 4.01 W, in which

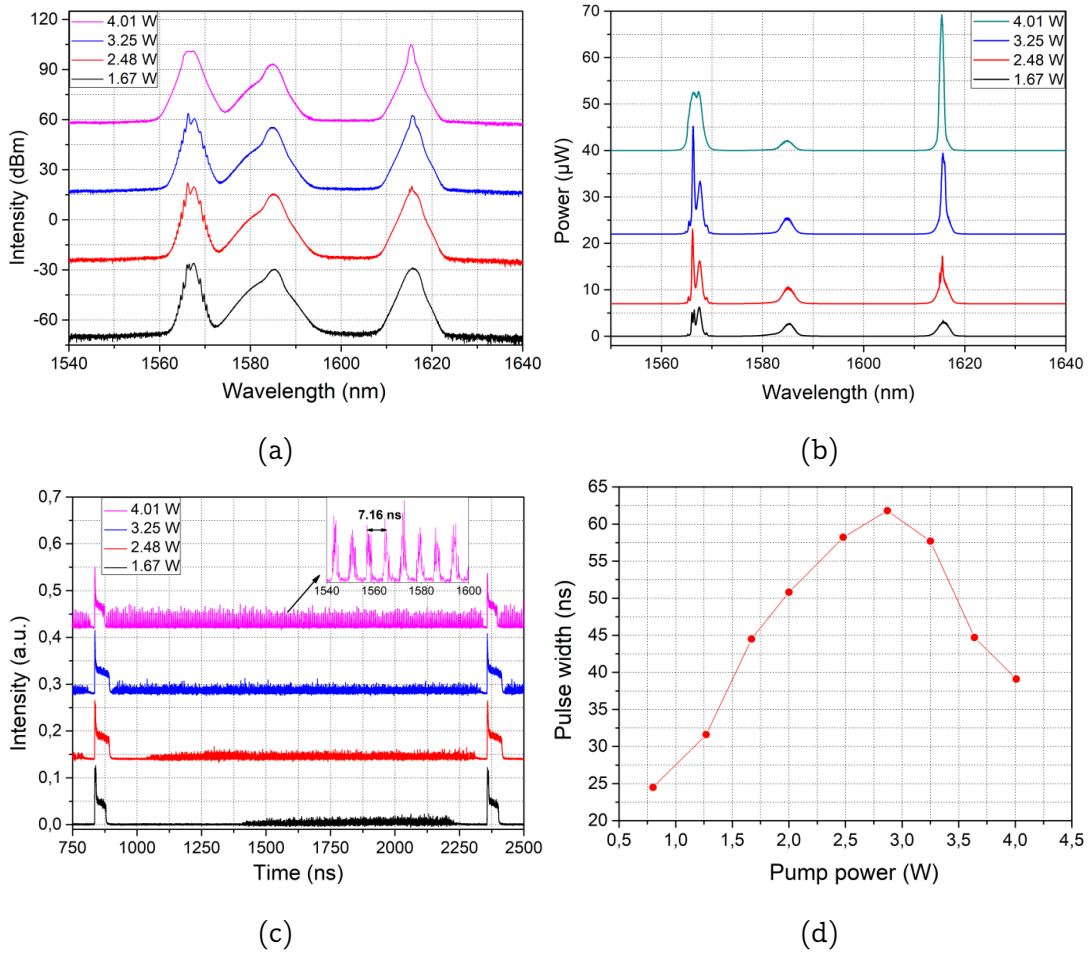

Figure 5.4: (a) Evolution of the spectrum in logarithmic scale and (b) in linear scale, (c) the corresponding oscilloscope trace and, (d) square pulse width, at different values of pump power.

the repetition frequency is ≈656.4 kHz corresponding to the fundamental repetition rate of the cavity. The signal-to-noise ratio (SNR) is ≈62 dB, which value reveals the good stability of the coexisting patterns. The inset of figure 5.5 depicts the RF signal envelope with a 250 MHz span. One can see that the envelope exhibits another frequency peak at ≈139.5 MHz, which corresponds to the repetition frequency of the high repetition rate harmonic pulses of the soliton bunches (cf. inset of figure 5.4c).

Finally, increasing the pump power has led to a slight wavelength shift of

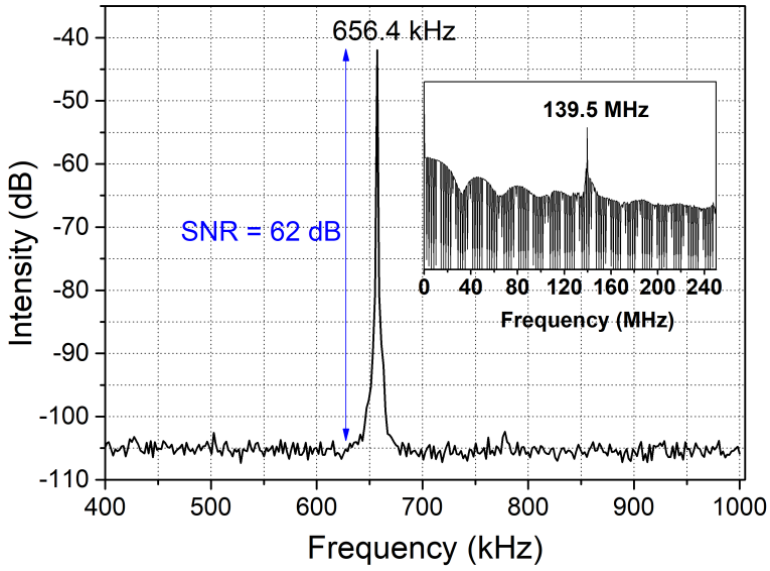

Figure 5.5: RF spectrum at the pump power of 4 W. Inset: RF spectrum over a 250 MHz span.

the central peaks of the lobes, and this can be explained by the variation of the gain-loss distribution[89]. Then, by increasing the pump power, despite few changes, the triple lobe regime is still stable and different soliton states coexist in the cavity. The contribution of each wavelength lobe in the coexisting soliton patterns is addressed in the next section.

5.5 Wavelength-resolved measurement

To further investigate the contribution of each wavelength in the spectrum, an optical tunable filter (OTF) inserted at the output of the laser cavity was used to conduct wavelength-resolved measurements. Figures 5.6 and 5.7 show the optical spectrum, and the corresponding filtered temporal traces of each wavelength lobe, at the pump power of 0.8 W and 4.01 W, respectively. Indeed, as the regime has slightly evolved with increasing the pump power, it is worth studying the contribution of each wavelength for a low and high value of the pump power. Let us consider the signal of figure 5.6, obtained at the pump power of 0.8 W. At the wavelength lobe centered at 1567 nm, an unresolved bunch of solitons is obtained, as presented by the black-curve trace in figure

5.6b. This appears more clearly in the zoom-in of the black trace (from 910 to 925 ns). The temporal traces of the middle wavelength lobe centered at 1585 nm, and the lobe centered at 1616 nm represented by the red and blue curves, respectively, both show a square condensed phase soliton with the same group velocity, which can be separated using an optical filter. In the left zoom in (from 30 to 100 ns) of figure 5.6b, the magenta curve representing the initial signal before filtering, one can note that the ensemble seems like staircase pulse with different intensity levels. After filtering, the red curve representing the lobe centered at 1585 nm seems to consist of the highest intensity part of the staircase pulse, and the low-intensity part is shared between both the lobes at 1585 nm and 1616 nm. Both signals are temporally superposed even if they correspond to different wavelengths. In general, pulse trains corresponding to different wavelengths should have different group velocities owing to the group velocity dispersion of the cavity, which results in different fundamental repetition frequencies on the RF spectrum[79]. However, our results demonstrate that the pulse ensembles are trapped together and coexist in the cavity; they co-propagate as a non-dispersive unit although they have different central wavelengths. This indicates that the pulse ensembles are group velocity locked.

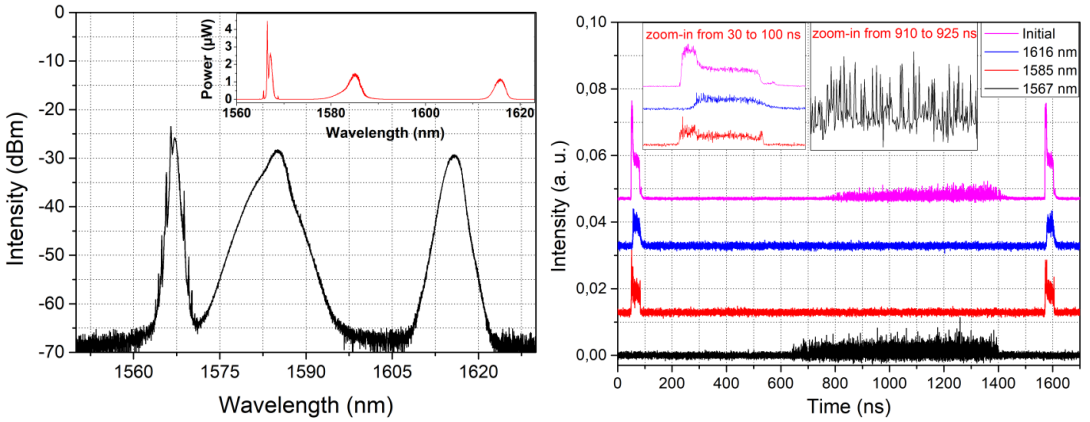

(a) (b)

Figure 5.6: Temporal trace of the initial and filtered signals at 0.8 W of pump power

Considering figure 5.7 which represents the signal filtering measurement at

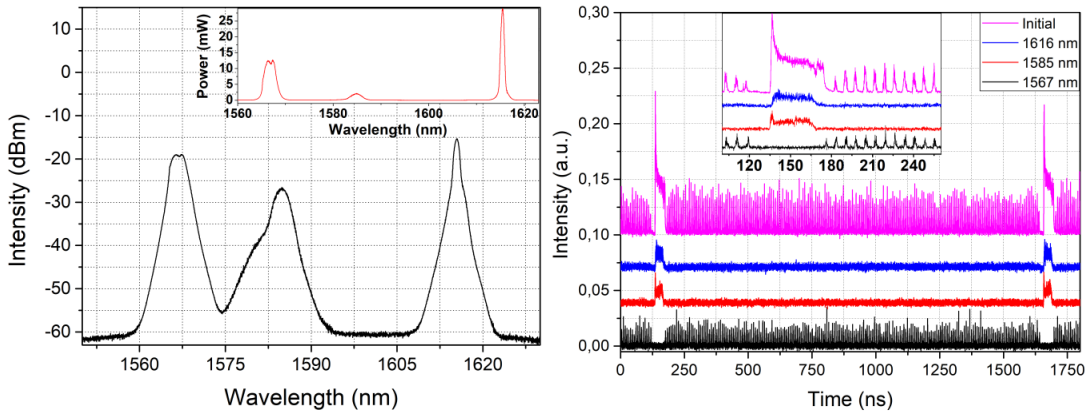

(a) (b)

Figure 5.7: Temporal trace of the initial and filtered signals at 4.02 W of pump power

the pump power of 4.02 W, one can conclude that despite the evolution of the signal for high pump power, the contribution of each wavelength is the same as in the case of the signal at low pump power described above. Finally, each wavelength lobe contributes to one soliton pattern in the temporal domain.

5.6 Harmonic generation

Harmonic mode-locked lasers are useful in a bunch of applications including high-speed optical communication systems. Passive harmonic mode-locked fiber lasers constitute an efficient alternative for such high repetition rate lasers, utilizing the nonlinear polarization technique, as the harmonic state arises spontaneously without additional apparatus to the laser cavity. It was observed experimentally for the first time in 1993 by Grudinin et al.[90] in Er-doped fiber laser, where it was reported that by adjusting the polarization controllers in the cavity and the circulating intracavity power, several stable harmonic operation frequencies ranging between 200 MHz and 1 GHz have been generated. In the studied triple-lobe wavelength regime, a harmonic state of the whole coexisting soliton patterns of the cavity can be generated by a fine adjustment of the PCs at a fixed pump power of 3.2 W. An order of 13th har-

monic has been reached. Figure 8 shows the optical spectra, the corresponding temporal traces of different harmonic orders . Their periods are ≈770 ns, ≈378 ns, and ≈189 ns, which represent the 2nd harmonic, 4th harmonic, and 8th harmonic, respectively, observed on the oscilloscope (cf. figure 5.8b). The switch from one harmonic to other can be performed by a further adjustment of PCs. Figure 5.9 shows optical spectra and temporal traces of other harmonic orders

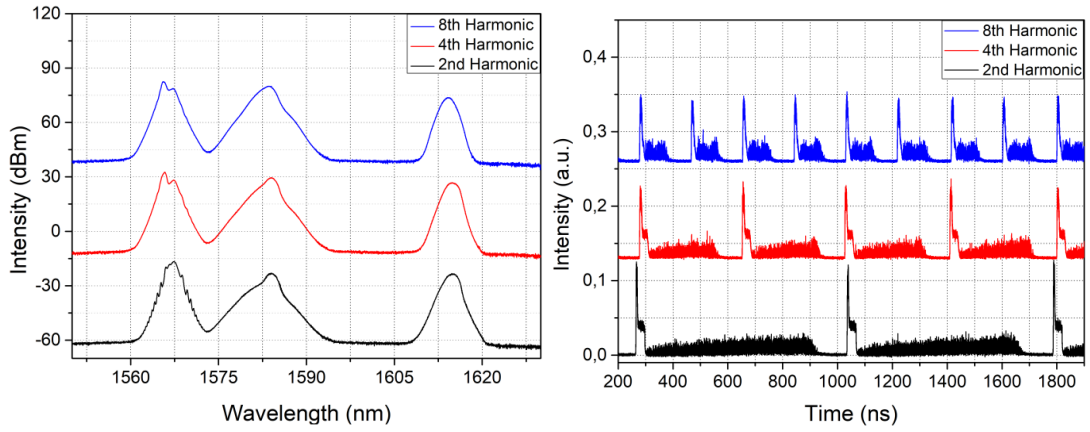

(a) (b)

Figure 5.8: Optical Spectra (a), and the corresponding temporal traces (b) of harmonic states at the pump power of 3.2 W.

such as 3rd, 5th, 9th, and 13th. For these two last harmonic orders, one can notice a timing jitter in the temporal trace in figure 5.9b as well as wavelength shifts as shown in figure 5.9a. The wavelength shift is due to the adjustment of the PCs since it modifies the characteristics of the nonlinear transmission curve of the artificial filtering. Multiple hypotheses have been suggested to explain the spontaneous arrangement of pulses as harmonic operation in passively mode-locked fiber lasers, including long-range soliton interaction due to acoustic waves emitted by the soliton pulses [], and the soliton self-frequency shift effect [].

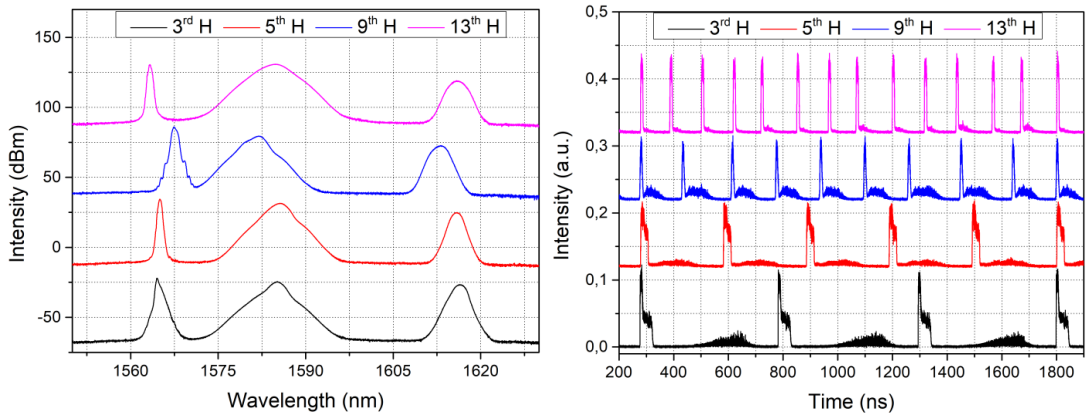

(a) (b)

Figure 5.9: Optical Spectra (a) and the corresponding temporal traces (b) of harmonic states at the pump power of 3.2 W.

5.7 Conclusion

We experimentally demonstrated the coexistence of different soliton states in a triple-wavelength mode-locked EDFL. The mode-locking is achieved through the nonlinear polarization rotation in a simple all-fiber ring cavity configuration. The spectrum exhibits three distinct well-separated spectral peaks centered at 1567 nm, 1585 nm, and 1616 nm. The triple wavelength oscillation can be attributed to the nonlinear filtering based on intensity-dependent polarization rotation and the linear loss of the cavity impacting the population inversion (gain). Utilizing an optical attenuator and an optical tunable filter, we confirmed that each soliton pattern corresponds to a specific spectral lobe, which can be separately controlled. This complex regime is operated at a fundamental repetition rate of 656.4 kHz. By carefully adjusting the PCs, the presented regime can evolve into different harmonic states. This work shows a novel operation regime, which could enrich the understanding of the composite state soliton dynamics and could be useful for various applications in wavelength division multiplexed transmission systems and optical signal processing. In the next chapter, I present the polarization-color domain wall regime, with two different wavelengths (color domains), coexisting with different polarization states (polarization domains).

Chapter 6

Polarization-color domain wall in fiber ring laser cavity

In physical systems, a domain wall (DW) refers to an interface separating two stable states. It is mainly due to a spontaneous symmetry breaking, to separate two distinct domains. This phenomenon manifests in a variety of fields, such as magnetism (where the domain wall represents the interface that separates domains with distinct magnetization in ferromagnetic materials) [91, 92], Bose-Einstein condensates [93], hydrodynamics [94], etc. DWs are also demonstrated in optical systems. They were first introduced in 1987 [95] when the authors theoretically predicted the existence of polarization domains in nonlinear optics. They reported that, when electromagnetic waves counter-propagate in a mirror-symmetry medium and by ignoring the optical Kerr self-effect, stable polarization states are formed. Hence, an arbitrary initial polarization evolves into a "domain structure". The study was experimentally confirmed, later on, by Pitois et al. [96]. The concept of domain wall solitons is introduced by Haelterman and Sheppard [97], where they demonstrated the existence of a novel type of vector dark solitary wave in Kerr media, consisting of localized structures that separate domains of orthogonal polarization states. These structures are then considered polarization domain walls (PDWs). Since then, PDWs have been the subject of several studies in the field of fiber lasers [98–105]. The phenomenon occurs generally in quasi-isotropic cavities (low

polarization-dependent losses) with high nonlinearity, and their generation is attributed mainly to the cross-coupling of the two polarization components through the optical Kerr nonlinearity [97].

In parallel, the theory of domain walls has also enabled the introduction of the concept of the so-called color domain walls (CDWs). Indeed, Haelterman and Badolo reported on dual-frequency wall solitary waves in single-mode fiber, which consist of localized structures separating two uniform fields of different frequencies [106]. In this context, Zhang et al [107] experimentally demonstrated a dual-wavelength domain wall type of dark soliton in a ring fiber laser. The authors show that this dark soliton is formed thanks to the cross-coupling between two different wavelength laser beams, and consists of a localized dip structure separating the two wavelength domains. In contrast with PDW, CDW occurs in a cavity with a polarizing element, and with high polarization-dependent losses. It has also been reported that highly nonlinear fiber (HNLF) is favorable for generating stable CDW pulses [100, 108, 109]. Recently, color domains have been demonstrated in a passively mode-locked fiber laser cavity where double and triple CDW occur [110], where the dynamics were associated to the cross-gain saturation between the spectral components. In another paper [100], it was reported that by using a Lyot filter in a Tm-doped fiber laser including HNLF, the generation of dual-wavelength operation could be facilitated. An interesting feature was the observation of CDW in which each optical component had a different polarization state like in PDW.

In this chapter, the generation of polarization-color domains in Er:Yb co-doped fiber laser is presented, where each color domain is associated with a different polarization state [111]. The chapter is organized as follows. In section 6.1, I present the experimental setup for the fiber laser cavity in the anomalous dispersion regime. Section 6.2 shows the generated pulse regime. Sections 6.3 and 6.4, are devoted to the wavelength, and polarization-resolved measurements, respectively.

6.1 Experimental setup

The laser cavity setup is shown in figure 6.1. It is a ring fiber laser including a double-clad co-doped Er:Yb fiber amplifier, in which the passive mode-locking is reached through nonlinear polarization evolution (NPE). The NPE is ensured by combining an inline polarizer with two polarization controllers (PC1 and PC2). The total cavity length is about 39 m, including 5 m double-clad fiber with -0.021 ps^2/m second-order dispersion, and 20 m HNLF with a dispersion parameter of 0.0 $\pm$ 1 $ps/(nm \cdot km)$. The nonlinear coefficient of the HNLF (NL-1550 POS-1016-A) is 13 $(W \cdot km)^{-1}$. The rest of the fiber in the cavity is a single-mode fiber (SMF) with second-order dispersion of -0.022 ps^2/m. The total net cavity dispersion is estimated to be -0.42 ps^2. The round-trip time is 195 ns corresponding to a fundamental cavity frequency of 5.1 MHz. A polarization-insensitive isolator (PI-ISO) is inserted to force the unidirectional propagation of the light. A 10 % output coupler (OC) is used to extract the signal from the cavity. The laser output characteristics are investigated using an optical spectrum analyzer, a 13-GHz oscilloscope combined with two 12-GHz photo-detectors, and a radio frequency (RF) spectrum analyzer.

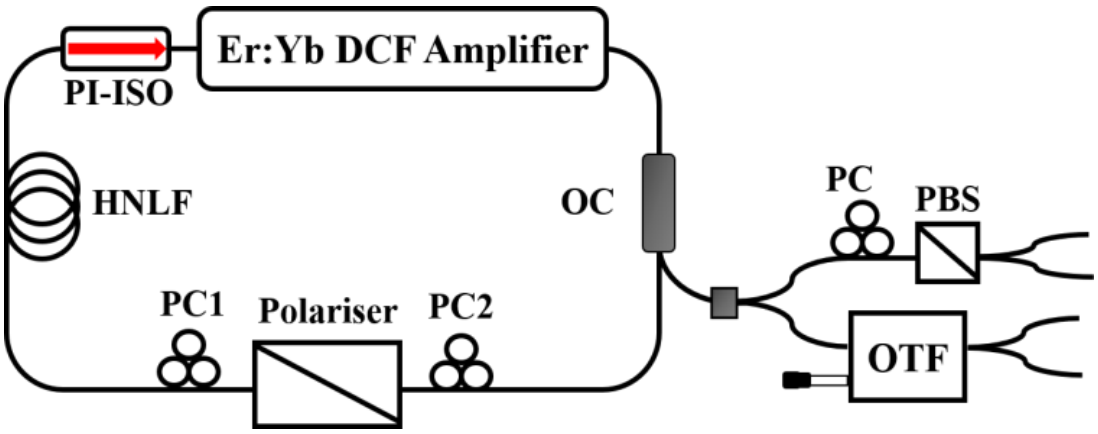

Figure 6.1: Experimental setup of the polarization-color domains: Er:Yb DCF amplifier (Erbium:Ytterbium codoped double-clad fiber amplifier), PI-ISO (isolator), PC (polarization controller), HNLF (highly nonlinear fiber), and OC (output coupler).

6.2 Dual-Wavelength generation regime

The birefringent spectral filtering effect combined with the NPE can be employed to achieve multiwavelength lasing output [112–114]. Indeed, as the artificial filter has narrow bandwidth within the effective gain bandwidth, a multi-wavelength operation is facilitated [112]. In our experiment, as 20 m of HNLF are inserted in the cavity, it is difficult to generate conventional solitons because of the high nonlinear phase accumulation within one cavity roundtrip. However, other nonlinear effects such as cross-coupling can be enhanced after the achievement of a dual-wavelength operation, which is favorable to the formation of stable domain walls [95]. In this section, I show the resulting dual-wavelength regime.

When the pump power is increased to 400 mW, continuous wave (CW) emission is achieved. Above this threshold, by slightly increasing the pump power and the orientation of the PC plates, we obtain the dual-wavelength operation. The resulting regime is shown in figure 2 for a pump power of 1.9 W. Figure 6.2a shows the optical spectrum of the laser emission, and shows two spectral lobes centered at ≈1547 nm and ≈1569 nm, with wavelength separation of ≈ 22 nm. The wavelength separation can also be determined by the intracavity birefringence expressed as $\Delta\lambda = \lambda^2/\Delta n \cdot L$ (where $\Delta n = \lambda/L_B$ is the average cavity fiber birefringence) [108]. In our case, we find a short average beating length $L_B = 60\ cm$ that is owing to the residual birefringence of SMF fiber with a beating length of a few meters [115, 116]. We assume that the natural birefringence of the HNLF and the double-clad fiber is higher than that of SMF fibers. The generation of well-separated dual wavelength is due to the combined effects of the equivalent Lyot filter and the control of the linear losses of the cavity, allowing the extension of the gain bandwidth.

The corresponding temporal trace is depicted in figure 6.2b, in which we observe a step-like pulse. We also note an intensity dip just after the step-like pulse, and the total duration of the pulse is about 190 ns, such that it occupies approximately the whole cavity whose roundtrip time is 195 ns. The

pulse repetition frequency shown in figure 6.2c is 5.1 MHz corresponding to the fundamental cavity frequency. The signal-to-noise ratio (SNR) is equal to 72 dB which demonstrates the high stability of the regime.

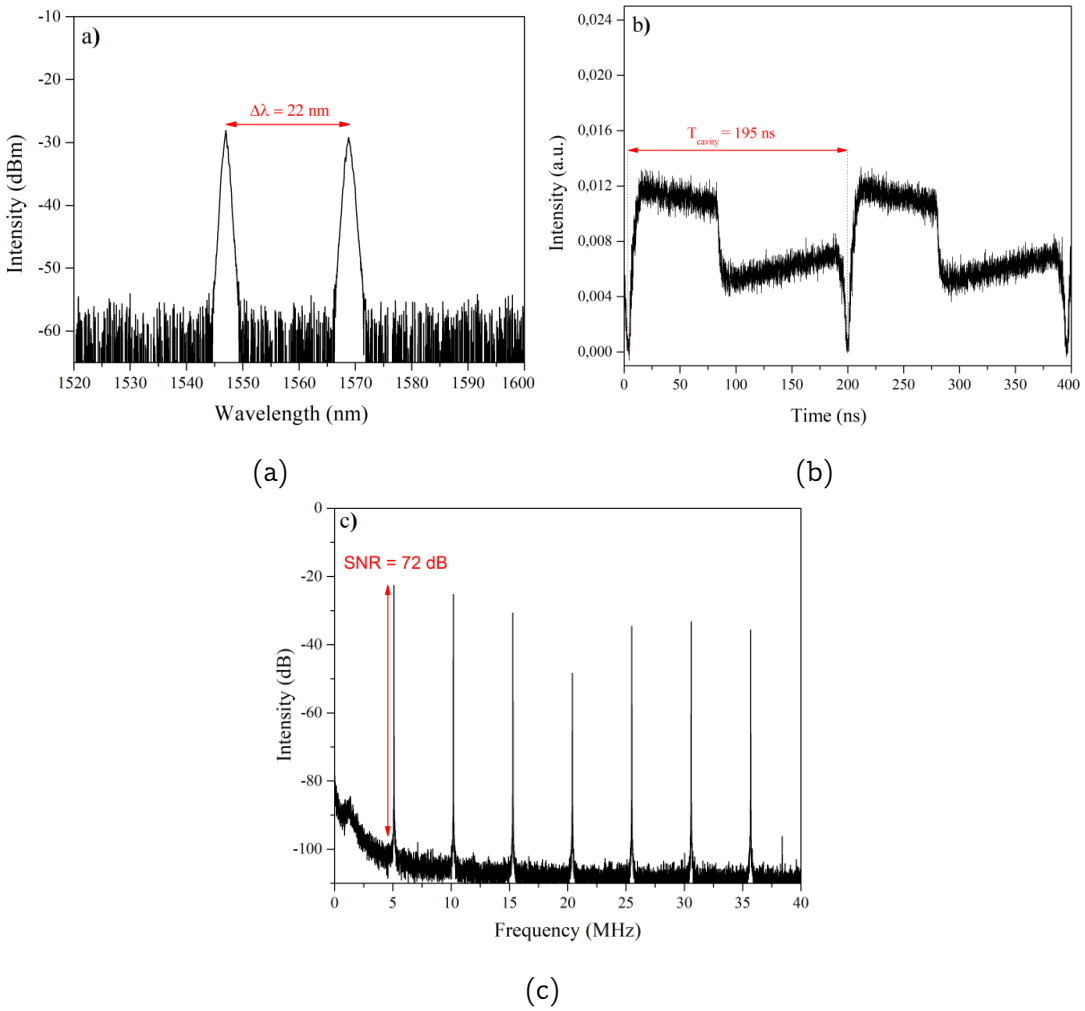

Figure 6.2: Optical characteristics of the dual-wavelength emission at the pump power of 1.9 W: (a) spectral profile, (b) the corresponding oscilloscope trace, and (c) radiofrequency spectrum.

In the next section, we investigate the obtained regime by resolving the contribution of each wavelength.

6.3 Wavelength-resolved measurement

To investigate the contribution of each wavelength lobe in the dual-wavelength spectrum, we perform a wavelength-resolved measurement with a tunable optical filter (SANTEC OTF-320) with a tuning range from 1500 nm to 1630 nm, and a resolution bandwidth of 0.5 nm. Figure 6.3, illustrates the temporal trace of both the initial pulse and the filtered output signals. We notice that the spectral components exhibit antiphase dynamics [117–119] and the laser emission is alternating between the two wavelengths centered at 1547 nm (red trace), and 1569 nm (green trace). These dynamics indicate that the total output signal is a combination of two wavelength domain-wall pulses that co-propagate as a non-dispersive unit (group velocity locked) at the fundamental repetition rate. To confirm the wavelength domain wall nature of the regime,

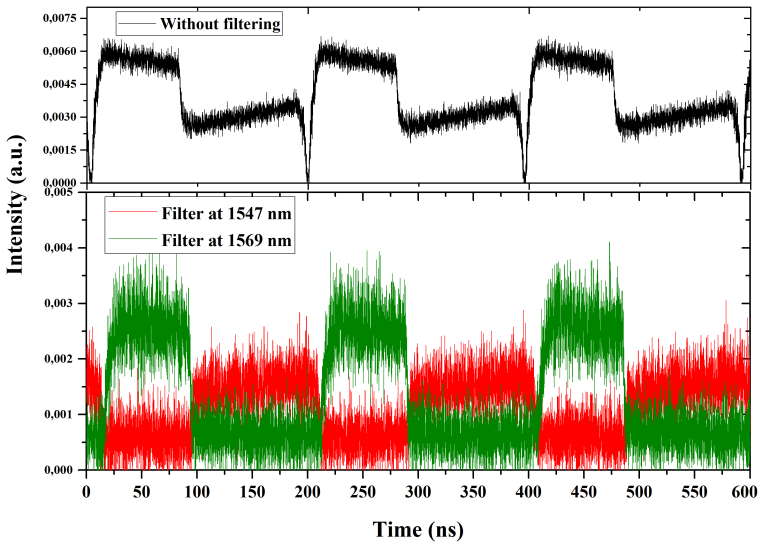

Figure 6.3: Temporal trace of the initial and filtered signal.

we study the evolution of the dip at the end of the cavity roundtrip while tuning the pump power. Figure 6.4 shows the evolution of the signal for different values of the pump power ranging from 1.7 to 2.4 W. Figure 6.4a depicts the evolution of the optical spectrum with the pump power, where we can note that the wavelength separation and the bandwidth of each one are both nearly constant with no significant wavelength shift. However, the temporal trace depicted in figure 6.4b is changed with increasing pump power, and the duty cycle

of each temporal component is modified. The duration of the square-shaped pulse associated with the longer wavelength (1569 nm) is reduced while the duration of the pulse associated with the shorter wavelength (1547 nm) is increased. Meanwhile, the dip-like at the end of the cavity roundtrip is stable regardless of the pump power as can be seen in figure 6.4b (with the help of the grid line at approximately 200 ns). In [110], it was demonstrated that the width of the dip evolved with the pump power and was interpreted as a recovery time for the gain because of the gain saturation. Here, the dynamic is controlled not only by the cross-gain saturation but also by cross-coupling through the optical Kerr effect, which could cause the absence of the dip evolution. This assumption is validated by an additional study based on a polarization-resolved experiment (in section 6.4).

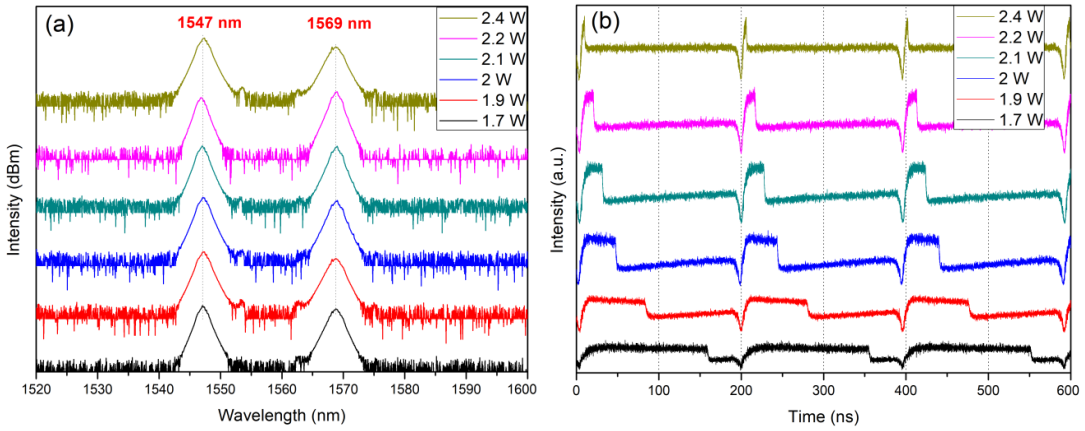

(a) (b)

Figure 6.4: Pulse characteristics for various pump power: (a) spectral evolution, and (b) temporal profile evolution.

Besides the effect of the pump power on the pulse characteristics, we observed that they can also be influenced by the orientation of the PC plates. Indeed, the rotations of the plates at a fixed pump power change the critical saturation power [120] which leads to an intensity variation of the domains. Consequently, the pulse duration and the duty factors of both domains could be tuned. Figure 6.5 depicts the measured optical spectra and the corresponding temporal profiles for different orientations of the PCs. As illustrated in

figure 6.5a, for each PC position, the central wavelengths are shifted, and the spectral separations are modified, which is due to the birefringent filter alteration. In the temporal profiles represented in figure 6.5b, the total pulse width remains unchanged whereas the width of each component is modified. Concerning the dip, we notice that its intensity depth varies with the pump power or the orientation of the PCs, however, its width remains almost unchanged, which is in agreement with polarization domain wall pulses [103, 121].

Finally, in this section, we confirm that the regime is a color domain wall. In the next section, we investigate the polarization state of each wavelength lobe contribution.

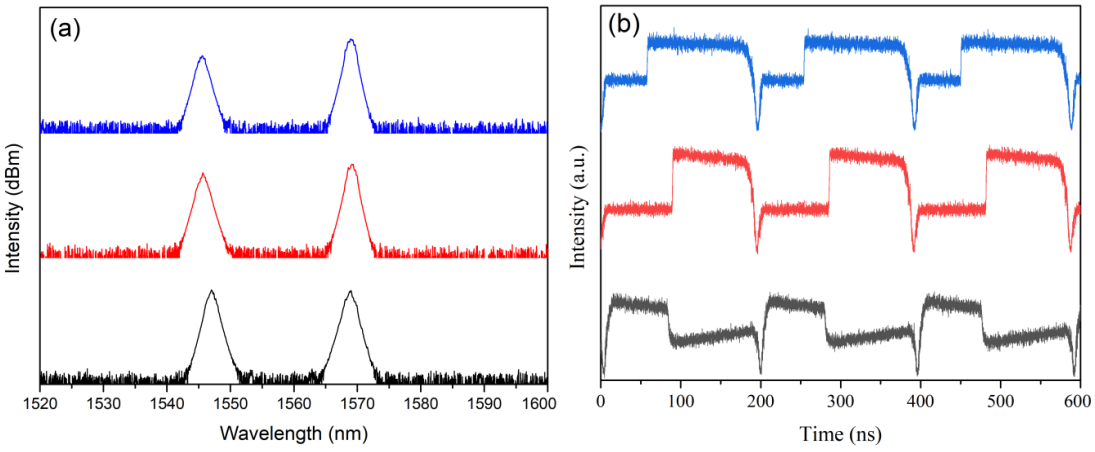

(a) (b)

Figure 6.5: Optical spectra (a) and oscilloscope profiles of the total intensity (b) at three different PC orientations.

6.4 Polarization-resolved measurement

To verify the existence of polarization domain walls, we perform a polarization-resolved measurement using a polarization beam-splitter (PBS) at the output of the laser cavity. When the output signal is split into its two orthogonal polarization components, we notice that the two polarization states have different output profiles in the lasing regime. This is an indication of the two-mode behavior of doped fiber lasers [117–119]. When the PC placed just before the PBS

(see figure 6.1) is adjusted, it is possible to separate the two modes that are amplified inside the cavity. As shown in figure 6.6, the optical spectrum of each polarization direction indicates that the two modes are orthogonal and linearly polarized, with spectral peaks centered on 1547 nm in the x-polarization and 1569 nm in the y-polarization. As can be seen in figure 6.6, each polarization component exhibits different spectral distributions and alternately almost separates the shorter and longer wavelength at the output of the PBS. The difference in the wavelength distribution indicates that the coupling between the two polarization components is incoherent [122].

Correspondingly, figure 6.7 shows the temporal profile of each polarization component. The total output signal is represented in a black trace. The two other pulses that are represented by blue and red traces correspond to y- and x-orthogonal polarization state, respectively. Each of the two orthogonal modes exhibits a different pulse width. These modes trap each other through Kerr non-linearity (cross-phase modulation) and propagate as one unit forming a domain wall[123].

Hence, PDWs are observed in a cavity with important polarization-dependent losses whereas their existence was predicted and observed in quasi-isotropic cavities. It is worth mentioning that if either the polarizer or the HNLF is removed from the laser cavity, the results cannot be reproduced. As there is a polarizing element in the laser cavity, we attribute the observation of domain-wall pulses to the combined effects of cross-gain saturation and cross-coupling through the optical Kerr effect induced by the high non-linearity of the HNLF.

6.5 Conclusion

In this chapter, we have reported the experimental observation of polarization-color domain-wall pulses in an Er-Yb co-doped fiber laser. In section 6.2, I presented the laser regime consisting of two spectral components and a step-like pulse that almost fills the whole laser cavity. The radio frequency trace

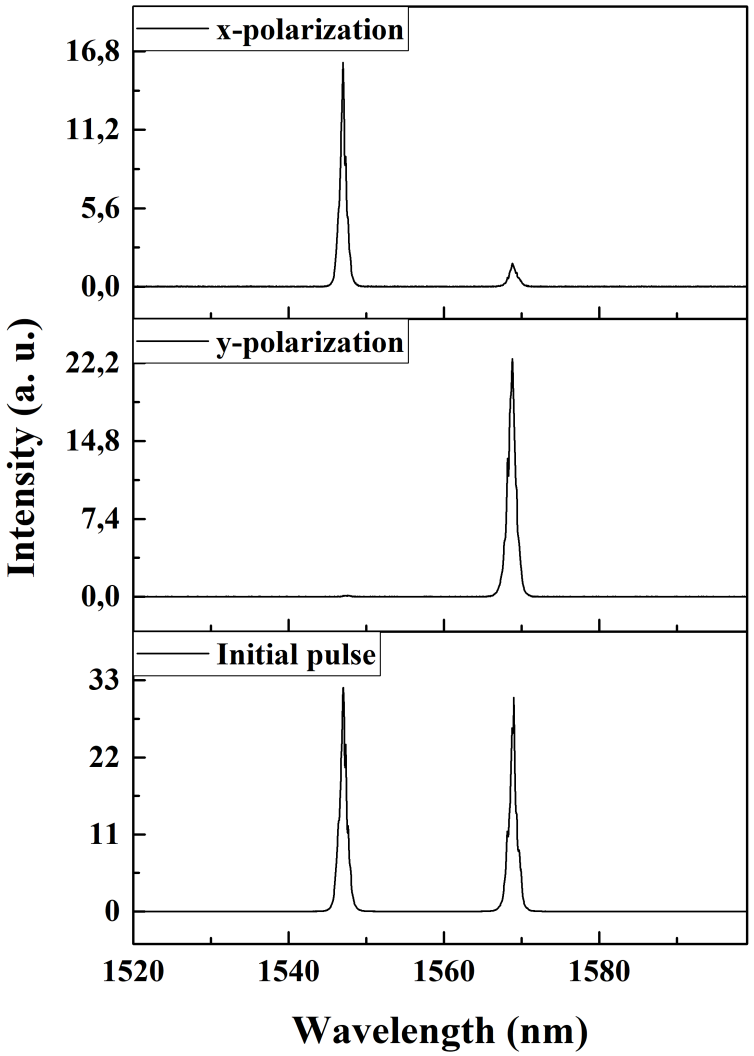

Figure 6.6: Spectral profile (linear unit) of the polarization-resolved experiment.

shows a stable signal with high SNR. In section 6.3, I presented the wavelength-resolved measurement that validates the existence of color domain operation where each wavelength contributes to a different temporal profile of the output signal. In section 6.4, the polarization-resolved measurement shows that each wavelength travels with a different polarization. Moreover, the observed dip at the end of the cavity round-trip is not affected by the pump power nor the orientation of the PCs indicating that the obtained results are polarization-color domains. We attribute the formation of this laser regime to the combined effects of cross-gain saturation and nonlinear cross-coupling through the optical

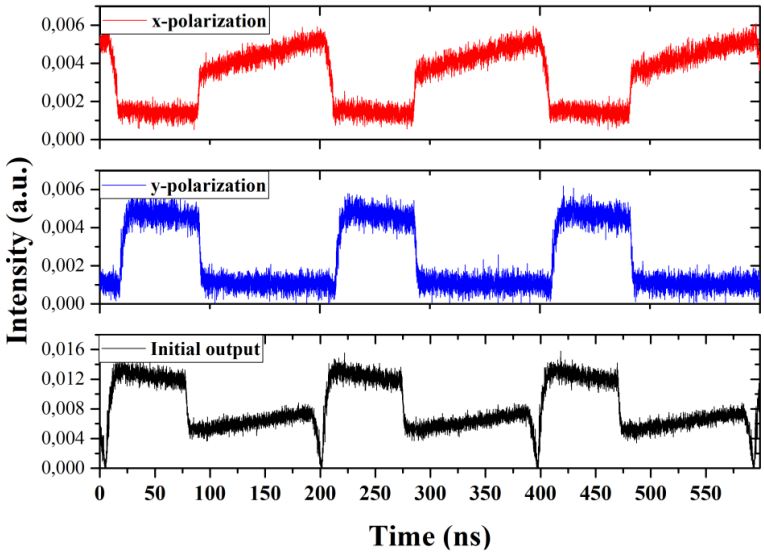

Figure 6.7: Oscilloscope trace of the polarization-resolved experiment.

Kerr effect.

Usually, PDW is not supported in cavities with strong polarization-dependent losses as is the case of our laser cavity. We assume that the distinct wavelengths associated with each polarization mode allow PDW to exist in a strongly dichroic cavity because of the cross-gain saturation. Also, the laser can operate in two distinct wavelengths because of the relatively important birefringence allowing to have a spectral separation of the equivalent Lyot filter falling in the gain bandwidth of the laser.

Chapter 7

Conclusion

The properties of the dissipative soliton resonance pulses have promising applications in various fields: telecommunications, medicine, engineering, and science. While DSRs were predicted theoretically and studied numerically their experimental verification is crucial. This thesis is dedicated to studying various DSR characteristics in rectangular pulses generated in Er:Yb fiber laser.

In the first chapter, I introduced the concept of dissipative soliton resonance through a review of theoretical and experimental reports on the phenomenon. Based on this review, it was evidenced that the question of the temporal coherence of these square pulses (potentially DSR pulses) is not rigorously studied. The autocorrelation trace of the pulse, which is usually provided by the authors, may not be sufficient to conclude whether the square pulse is coherent or not. On the other side, there have been many studies on the noise-like square pulses for which the characteristics are similar to those of the DSR pulses. So direct measurements of the temporal coherence of the experimental square pulses are required to distinguish DSR from noise-like pulses.

The thesis work is a continuation of the experimental study of laser cavities and pulse generation in my group, so in the first chapter, I reviewed the remarkable results already obtained: the generation of high-energy square pulses up to 10 μJ, high-harmonic square pulses using a ring fiber laser cavity, etc. To achieve reproducible results, the laser cavity needs to be stable during the experiment time, so the first step of the study was laser cavity optimizations

to search for a more stable regime. Also in this experiment, I tested a laser cavity with a very low net dispersion by using a dispersion-shifted fiber (DSF). The resulting regime seems to exhibit similar characteristics compared to that for higher net negative dispersion.

In the second chapter, I investigate the temporal coherence of the DSR-like rectangular pulses, using a Mach-Zehnder interferometer to circumvent the eventual limits of the autocorrelation apparatus. For the study, the Mach-Zehnder interferometer was built and verified with a distributed feed-back laser. In the first study, I used an all-fibered MZI, where the OPD tuning is limited by fiber splicing. Afterward, the MZI is optimized by inserting free-space collimators in one arm in order to easily tune the OPD.

I demonstrated that although the obtained rectangular pulses show most of the DSR pulse features, they are not necessarily DSR but they may be packets of shorter pulses. Due to technical limitations, I scan a short part of the rectangular pulse, so the coherence measurement is local.

In chapter 5 we experimentally demonstrated the coexistence of different soliton states in a triple-wavelength mode-locked EDFL. The mode-locking is achieved through the nonlinear polarization evolution in a simple all-fiber ring cavity configuration. The spectrum exhibits three distinct well-separated spectral peaks centered at 1567 nm, 1585 nm, and 1616 nm. The triple wavelength oscillation can be attributed to the nonlinear filtering based on intensity-dependent polarization rotation and the linear loss of the cavity impacting the population inversion (gain). Utilizing an optical attenuator and an optical tunable filter, we confirmed that each soliton pattern corresponds to a specific spectral lobe, which can be separately controlled. This complex regime is operated at a fundamental repetition rate of 656.4 kHz. By carefully adjusting the PCs, the presented regime can evolve into different harmonic states. This work shows a novel operation regime, which could enrich the understanding of the composite state soliton dynamics and could be useful for various applications in wavelength division multiplexed transmission systems and optical signal processing.

In chapter 6, we have reported the experimental observation of polarization-color domain-wall pulses in an Er-Yb co-doped fiber laser. I presented the laser regime consisting of two spectral components and a step-like pulse that almost fills the whole laser cavity. The radio frequency trace shows a stable signal with high SNR. I show the wavelength-resolved measurement that validates the existence of color domain operation where each wavelength contributes to a different temporal profile of the output signal. The polarization-resolved measurement shows that each wavelength travels with a different polarization. Moreover, the observed dip at the end of the cavity round-trip is not affected by the pump power nor the orientation of the PCs indicating that the obtained results are polarization-color domains. We attribute the formation of this laser regime to the combined effects of cross-gain saturation and nonlinear cross-coupling through the optical Kerr effect.

Usually, PDW is not supported in cavities with strong polarization-dependent losses as is the case of our laser cavity. We assume that the distinct wavelengths associated with each polarization mode allow PDW to exist in a strongly dichroic cavity because of the cross-gain saturation. Also, the laser can operate in two distinct wavelengths because of the relatively important birefringence allowing to have a spectral separation of the equivalent Lyot filter falling in the gain bandwidth of the laser.

The presented work is a step forward in the characterization and understanding of pulse generation in fiber laser cavities. The achieved results were presented at a number of conferences and published in articles and proceedings.

Appendices

Appendix A

Effect of the group-velocity dispersion on nanosecond rectangular pulses

In chapter 4, I studied the temporal coherence of the DSR-like rectangular pulses using a Mach-Zehnder interferometer (MZI) which permitted a local coherence measurement. Indeed, as the pulses are relatively large with durations ranging from a few ns to a few tens of ns, the coherence is studied on a short portion of the pulse using free space collimators mounted on translation stages. In this study, with the effect of the group velocity dispersion, I attempt to characterize the coherence of the rectangular pulses with a more global approach based on the temporal waveform evolution of the pulse after propagating through a relatively long single-mode fiber (SMF) coil (30 km and 60 km). For this, I start by presenting the experimental results. These latter are then compared with the simulation results, performing the propagation of highly-chirped coherent nanosecond rectangular pulses.

A.1 GVD effect on DSR-like rectangular pulses using 30 km of SMF

A.1.1 Experimental results

The laser cavity length is about 290 m corresponding to 1.45 μs of round trip time and a free spectral range of about 690 kHz. This regime is studied in Chapter 4, where I verified the DSR characteristics such as a linear increase of energy and pulse width with the pump power, a relatively constant peak power, and an invariant optical spectrum. The rectangular pulses are then launched into 30 km of SMF coil.

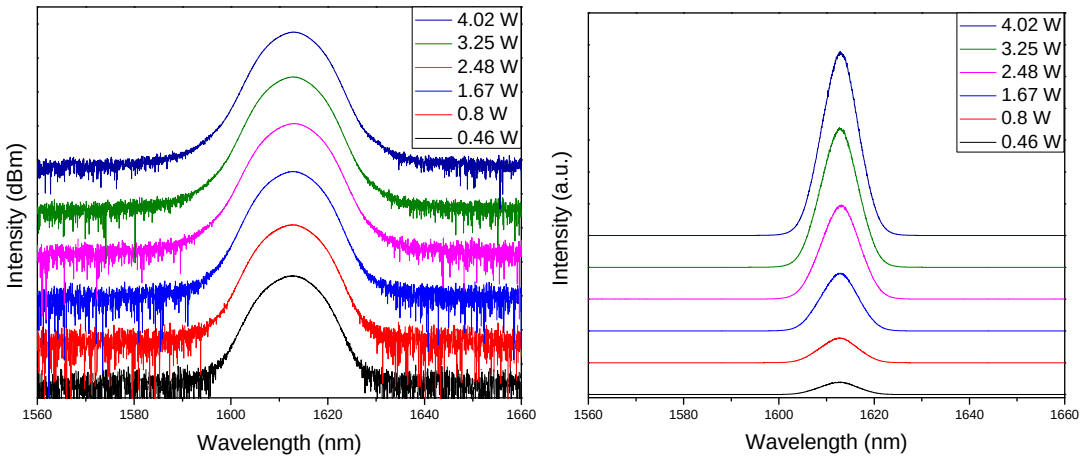

(a) (b)

Figure A.1: Optical spectra in logarithmic (a), and linear (b) scales, for different pump powers ranging from 0.46 W to 4.02 W

Figures A.1a and A.1b show the optical spectra of the regime in both logarithmic and linear representations, respectively, for different pump powers ranging from 0.46 W to 4.02 W. The spectral bandwidth is constant around 9 nm, and only the intensity is increased with increasing pump power as it is visible in the linear representation in figure A.1b. The corresponding temporal traces of the initial pulses at the laser output are shown in figure A.2a, and figure A.2b represents the corresponding temporal traces at the output of the SMF coil. We can see that the wings of the pulse propagating through 30 km of

the dispersive medium are stretched, and the pulse loses its rectangular shape. For pump powers of 0.46 W and 0.8 W, where the initial pulse widths are 6.5 ns and 12.2 ns, respectively, the temporal trace after propagation through the SMF coil mimics a Gaussian profile as the spectral waveform (see the spectrum of figure A.1b). For higher pump powers and larger pulses, the central part of the pulse remains flat. Nevertheless, the rise time of the initial rectangular pulses is around 0.1 ns while the rise time after the SMF coil is much larger as depicted in figure A.2c.

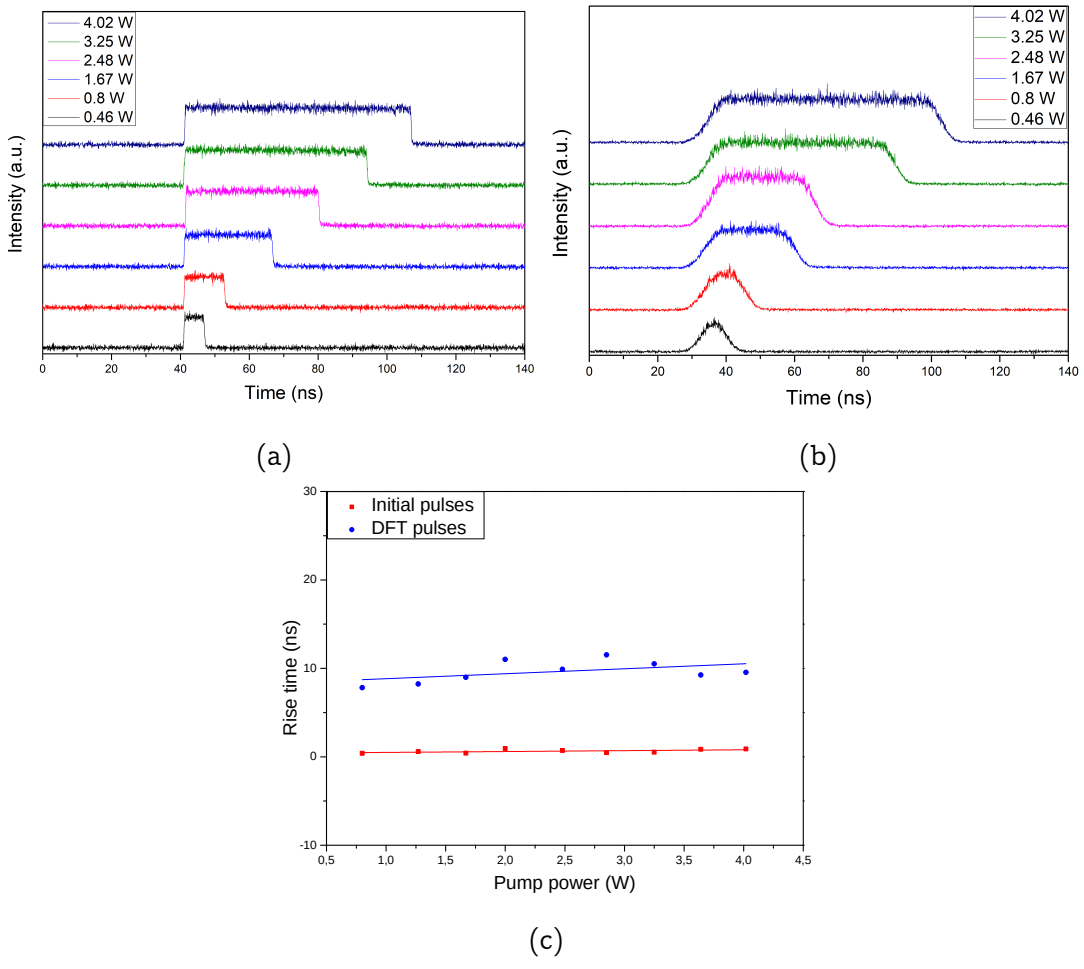

Figure A.2: Pulse temporal traces for different pump powers (a) at the reference output and (b) at the output of the SMF coil. (c) Rise-time of the initial pulses (red squares fitted with a linear red curve) and after the SMF coil (blue dots fitted with a linear blue curve).

Let us focus on the shortest initial pulse for a pump power of 0.46 W, which

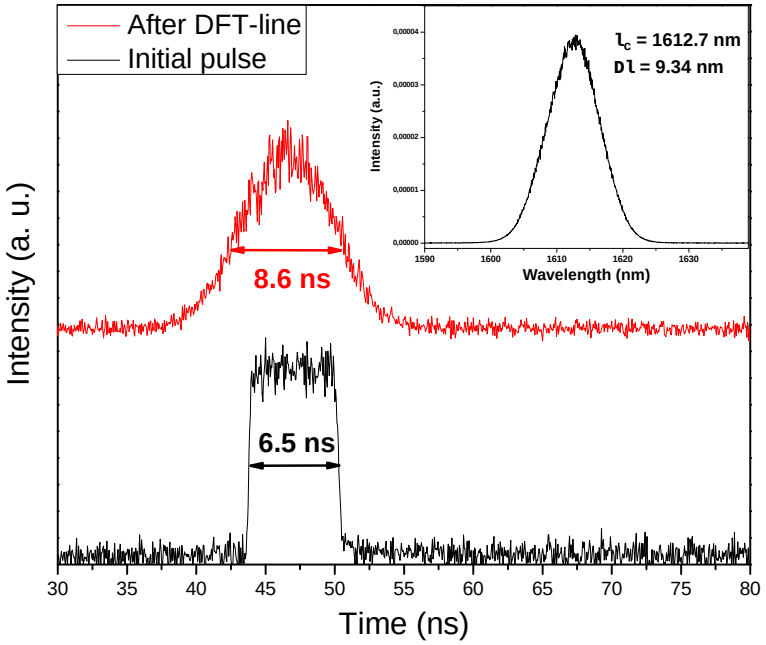

Figure A.3: Temporal trace of the initial rectangular pulse at the pump power of 0.46 W represented in black, and the corresponding temporal trace of the pulse at the output of the 30 km SMF coil. The inset figure represents the initial optical spectrum in a linear scale.

is depicted in figure A.3. The black curve represents the initial pulse with a pulse width of about 6.5 ns, and after traveling through the SMF coil, the pulse width is about 8.6 ns as represented by the red curve. Note that the pulse width at half maximum increased considerably and the pulse shape after fiber propagation changed from rectangular to Gaussian profile, mimicking the optical spectrum. In the next section, a comparison between the experimental result and simulation is performed.

A.1.2 Simulation results:

For further investigation of the GVD effect on the pulses, additional numerical simulations have been performed. In the study, I consider the optical fiber as a purely second-order dispersive medium. In addition, I consider the initial peak power of the pulse relatively low so that the nonlinear effects can be neglected. In the reference frame moving at the group velocity, the electric field envelope

at the abscissa z is related to the incident electric field envelope through the integral formula [124]:

$$A(z,t) = \sqrt{\frac{1}{2i\pi\beta_2 z}} \int A(0,t').exp\Big(\frac{-1}{2} i \frac{(t-t')^2}{\beta_2 z}\Big) dt' \tag{A.1}$$

where $A(0,t)$ is the initial pulse profile, and $A(z,t)$ is the pulse profile after propagation through the fiber of length z. The coefficient β_2 is the group velocity dispersion parameter. In these simulations, I consider a super-Gaussian pulse profile given by [124]:

$$A(0,t) = exp\Big(- \big(\frac{1+iC}{2}\big) \cdot \Big(\frac{t}{t_0}\Big)^{2m}\Big) \tag{A.2}$$

In this section, I study the propagation of a pulse with a pulse width of 6.5 ns through 30 km of single-mode fiber (SMF) and compare the simulation and experimental results, supposing that the pulse is coherent (with no fine structures within the rectangular envelope). In the simulations, I set the values of a few parameters, such as the super-gaussian order or the chirp parameter, based on experimental pulse characteristics.

A.1.2.a) Simulation parameters

Super-gaussian order, m:

The super-gaussian order has a key role in the shape-changing of the pulse during its propagation through a dispersive medium. The used super-gaussian order in my simulations is estimated based on the experimental pulse characteristics, using the formula[124]:

$$T_r = (ln9)\frac{T_0}{2m} \approx \frac{T_0}{m} \tag{A.3}$$

where T_r is the rise time and T_0 is the initial half pulse width. The table A.1 contains the different characteristic values of the experimental rectangular pulses from which I calculate the approximation value of m (here, I provide only the value for the shortest pulse). Thus, for the shortest pulse with a width of 6.5 ns, m is estimated to be about 12. In the simulations, I set m = 10.

Pump power	Initial pulse width, T	Rise time, T_r	$m \approx \frac{T}{2T_r}$
0.48 W	6.5 ns	0.261 ns	12.45

Table A.1: Estimation of the super-gaussian order m.

GVD parameter, β_2:

Based on the characteristics of the used SMF28 fiber (Corning), I use the dispersion value of $D = 22\ ps/(nm.km)$, which is the dispersion value for a wavelength around 1625 nm. Indeed, the central wavelength of experimental pulses is around 1612 nm. Thus, using the formula :

$$\beta_2 = -\frac{\lambda^2}{2\pi c} D \tag{A.4}$$

the GVD parameter is estimated to be $\beta_2 = -30.3\ ps^2/km$.

Initial chirp parameter, C

The chirp parameter is estimated based on the pulse width and the spectral bandwidth of the studied experimental pulses. First, I determine the pulse width at the Fourier limit through the relation

$$\Delta\nu\Delta\tau_0 = TBP \tag{A.5}$$

The time-bandwidth product $TBP = 0.441$ for a Gaussian pulse. I use this value to estimate the width of the transform-limited pulse :

$$\Delta\tau_0 = \frac{TBP}{\Delta\nu} = TBP\frac{\lambda^2}{c\Delta\lambda} \tag{A.6}$$

Where the central wavelength is $\lambda = 1612\ nm$, and the spectral bandwidth $\Delta\lambda = 9.34\ nm$. Thus $\Delta\tau_0 \approx 410\ fs$. In the presence of a chirp, the pulse width is related to the transform-limited pulse width by the relation

$$\Delta\tau = \sqrt{1 + C^2}\Delta\tau_0 \tag{A.7}$$

The parameter C is calculated to be $C \approx 16000$ for $\Delta\tau = 6.5\ ns$.

A.1.2.b) Simulation results

Experimentally, we note from figure A.3 that after propagating through the fiber, the pulse changes in shape from rectangular to Gaussian form. Moreover, the pulse broadens from 6.5 ns to 8.6 ns of FWHM. In the following figures, the same pulse width is simulated, and made to propagate through 30 km of fiber with different chirp parameter values. Figure A.4 shows the result for C = 0. This figure is plotted as a reference since we know that experimental pulses are chirped. The initial pulse in blue is superposed with the same pulse after 30 km of fiber in red, so the dispersion here has no effect. This is expected since the pulse is relatively large and with no chirp. Thus, 30 km of fiber is not enough to produce a visible impact on the pulse.

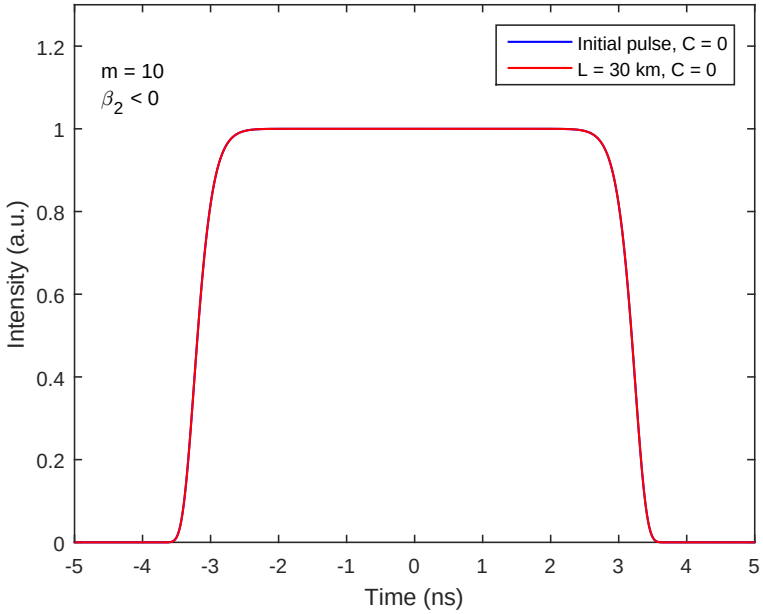

Figure A.4: Temporal trace of the initial rectangular pulse, with initial chirp parameter C=0, in blue. The red curve represents its propagation through 30 km of SMF28.

In figures A.5 and A.6, an initial chirp parameter is set to $C = +/-16000$ as estimated in the section above. In figure A.5a the chirp is set to be negative $C = -16000$, leading to a positive product $\beta_2 C > 0$. The impact is visible on the pulse after propagating through the fiber. We observe a narrowing of the FWHM, but the wings of the pulse spread out beyond the initial pulse.

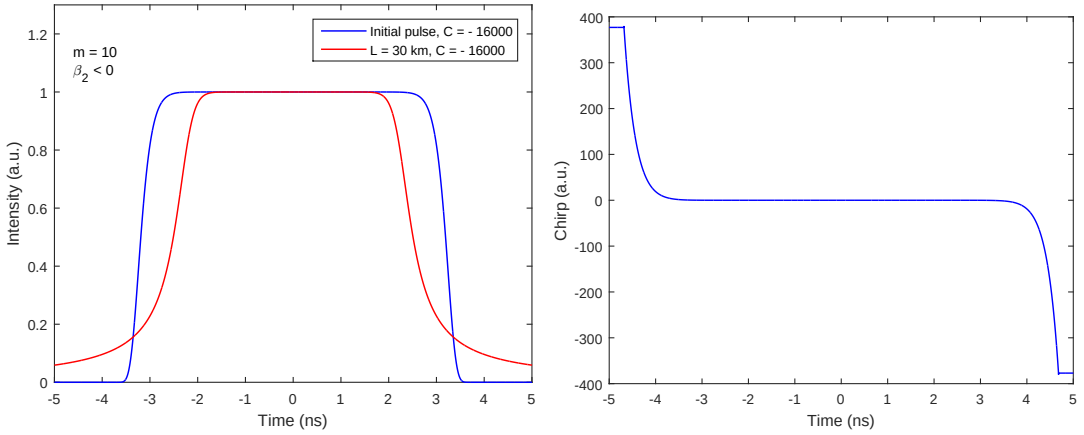

(a) (b)

Figure A.5: (a) Temporal trace of the initial rectangular pulse, with a negative initial chirp parameter $C = -16000$, in blue, and after propagating through 30 km of SMF28 in red. (b) The chirp of the initial pulse.

Contrarily, the FWHM increased in the experimental case. Also, note that the top of the pulse is still flat conversely to the experimental pulse. Figure A.5b represents the chirp of the initial pulse, which is weak on the central part of the pulse and large on the edges of the pulse. The next figure shows the result for a positive initial chirp parameter $C = 16000$, for which the product $\beta_2 C < 0$.

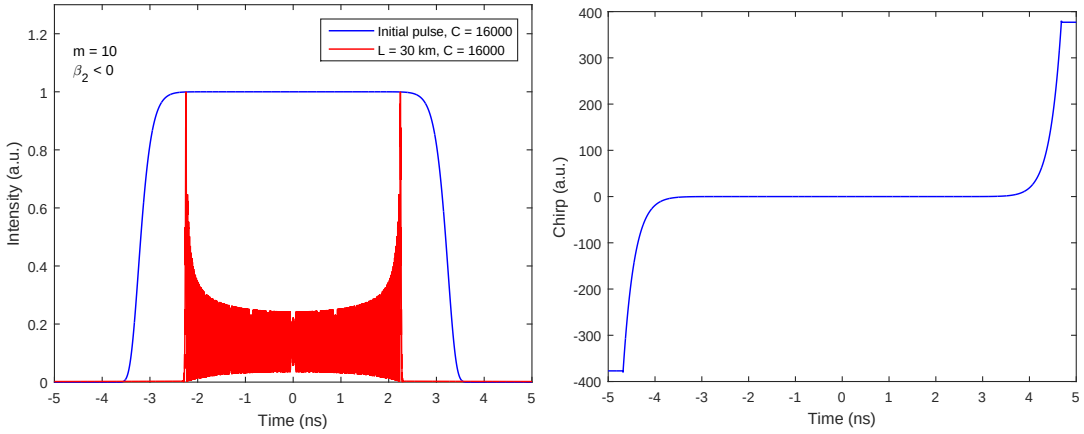

(a) (b)

Figure A.6: (a) Temporal trace of the initial rectangular pulse, with a positive initial chirp parameter $C = 16000$, in blue, and after propagating through 30 km of SMF28 in red. (b) The chirp of the initial pulse.

Figure A.6a displays an oscillatory temporal trace in red, with some intense wings at the edges of the pulse. In the case of a negative product $\beta_2 C < 0$, compression of the pulse occurs for a certain range of fiber length (dispersion). The oscillatory dynamics in the red curve correspond to a compression pattern and as the chirp of the pulse edges is larger than the central one, the wings of the pulse compress faster than the central part [125]. Consequently, the pulse evolves into a car-ear profile with many oscillation patterns. When the chirp would be compensated, the pulse shape becomes Gaussian.

A.1.3 Broadening factor

For complicated pulse shapes such as super-gaussian pulses, the FWHM is not a true measure of the pulse width [124]. Instead, it is more accurately described by the root-mean-square (RMS) width defined as:

$$\sigma = \left[\left\langle T^2 \right\rangle - \left\langle T \right\rangle^2\right]^{1/2} \tag{A.8}$$

where the angle brackets represent averaging over the intensity profile as :

$$\left\langle T^n \right\rangle = \frac{\int_{-\infty}^{+\infty} T^n |U(z,T)|^2 dT}{\int_{-\infty}^{+\infty} |U(z,T)|^2 dT} \tag{A.9}$$

The moments $\langle T \rangle$ and $\langle T^2 \rangle$ can be calculated analytically for some specific cases. Particularly, it is possible to evaluate the broadening factor σ/σ_0 for super-gaussian pulses using [124]:

$$\frac{\sigma}{\sigma_0} = \left[1 + \frac{\Gamma(1/2m)}{\Gamma(3/2m)} \frac{c\beta_2 z}{T_0^2} + m^2(1+C^2)\frac{\Gamma(2-1/2m)}{\Gamma(3/2m)} \left(\frac{\beta_2 z}{T_0^2}\right)\right]^{1/2} \tag{A.10}$$

Where $\Gamma(x)$ is the gamma function. In the following, I evaluate the broadening factor σ/σ_0 of the pulse for different chirp parameter values $C = 0, +/-16000$ using the equation Eq.A.10, and the broadening factor of the simulated pulses using the definition of the RMS given in Eq.A.8.

Figure A.7 shows the broadening factor, calculated from Eq.A.10, of the pulse versus the fiber length z, in an anomalous GVD regime, for different values of the chirp parameter C. For $C = 0$, the broadening factor $\frac{\sigma}{\sigma_0} = 1$,

which means that there is neither narrowing nor broadening of the pulse for the values of z within 40 km (maximum z-value in the plot). However, for a positive chirp parameter ($C = 16000$), the broadening factor is below 1 at the beginning and then increases rapidly, which is expected as $\beta_2 C < 0$. Finally, for a negative chirp ($C = -16000$), the broadening factor increases, which is also expected when $\beta_2 C > 0$.

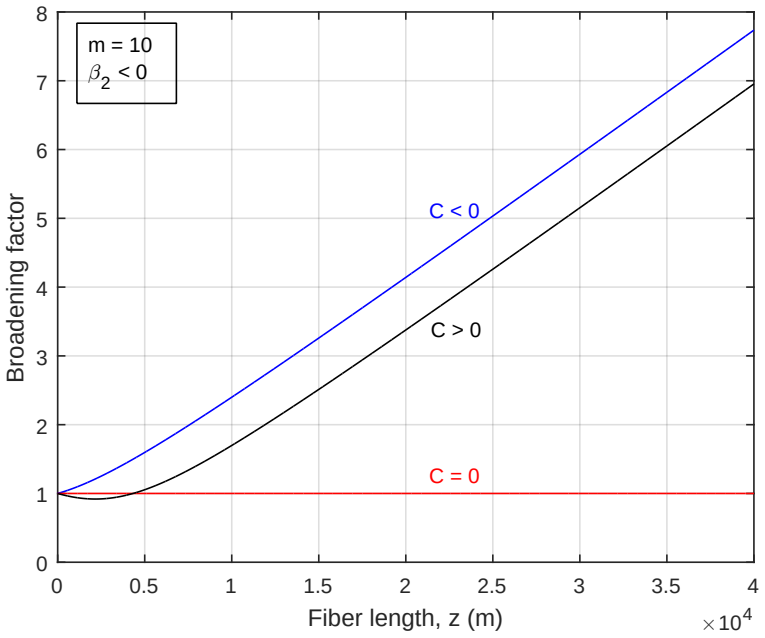

Figure A.7: Broadening factor as a function of the fiber length z, with anomalous-GVD parameter ($\beta_2 < 0$), for a super-gaussian pulse ($m = 10$) with different values of the chirp parameter: $C = 0$ in red, $C = +16000$ in black, and $C = -16000$ in blue.

The aim of the plots of figure A.7 is to compare the broadening factor at $z = 2.1\ km$ and $z = 30\ km$, with the broadening factor that I calculated from the simulations to validate the simulation results. The following table A.2 summarizes the calculated values from simulated pulses for $z = 2.1,\ 30\ km$, $m = 10$, and $\beta_2 = -30.3\ ps^2/km$. The values calculated from (Eq.A.10) and simulations are similar so the resulting simulated pulses after propagation in fiber, shown in figures A.5 and A.6, are correct. Note that even if at first sight, the propagated pulse of figure A.5a seems to be narrowed, RMS width shows that there is a broadening of the pulse as $\frac{\sigma}{\sigma_0} > 1$.

Broadening factor, $\frac{\sigma}{\sigma_0}$	At z=2.1 km		At z=30 km	
	From (Eq.A.10)	Simulations	From (Eq.A.10)	Simulations
C = -16000	1.2033	1.2033	5.9311	5.9142
C = 0	1	1	1	1
C = 16000	0.9190	0.9091	5.1534	5.1376

Table A.2: Broadening factor, $\frac{\sigma}{\sigma_0}$, at fiber length of z = 2.1 km and 30 km, for different values of the chirp parameter C = -16000; 0; +16000.

A.2 GVD effect on DSR-like rectangular pulses using 60 km of SMF

As the available fiber SMF fiber is limited to 30 km, I used an optical circulator to double the length and compare the GVD process on the DSR-like pulses with both 30km and 60 km. Moreover, the pulse studied here is slightly shorter than the pulse studied in the previous section.

A.2.1 Experimental setup

For further investigation of the GVD effect on the rectangular pulses, a new experimental setup has been implemented as shown in figure A.8. It is an extension of the SMF coil using an optical circulator. Indeed, using a circulator, the light entering port 1 exits from port 2 and then propagates through the 30 km of fiber. A 30% coupler is used to create a simple fiber loop mirror. The light entering the coupler is reflected back. One part exits and is combined with a photodetector to be analyzed by oscilloscope after propagating 30 km of fiber. Another part is reflected back to the fiber coil, enters from port 2 of the circulator, and exists from port 3. At the output of port 3, the light would have traveled 60 km of fiber, and the temporal trace of the signal is analyzed and compared with that at the output of 30 km of fiber.

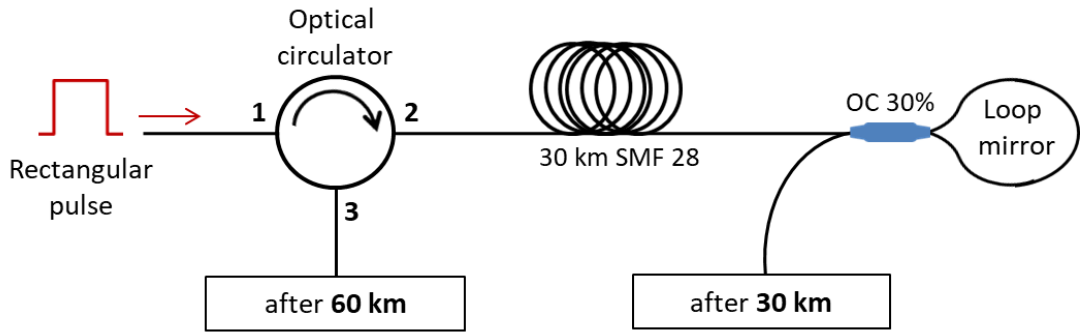

Figure A.8: Experimental setup. Optical circulator, OC: optical coupler, SMF 28: single-mode fiber.

A.2.2 Experimental results

The temporal trace of the pulse obtained for the pump power of 2.48 W is given in figure A.9a. There is one pulse per cavity round-trip, with a pulse width of 41.2 ns, as shown in the inset figure. The corresponding optical spectrum is centered at a wavelength of 1613 nm as shown in figure A.9b). The spectral bandwidth measured at -3 dB is about 9.31 nm. Figure A.9c represents the RF spectrum trace with a signal-to-noise ratio of 50 dB. The inset figure shows a characteristic RF spectrum for square pulses. The regime is stable for pump power ranging from 0.48 W to 3.64 W, without PC readjustment. Moreover, the temporal shape, as illustrated in figure A.10a, remains perfectly square without wave-breaking as a function of pump power. The optical spectrum also keeps its initial shape by holding the spectral bandwidth at -3 dB around 9.5 nm as shown in figure A.10b.

Figure A.11(a) shows the temporal trace of the initial rectangular pulses at the laser output. The corresponding optical spectra are represented in a linear scale in figure A.11(b). The linear representation of the optical spectrum at the reference permits a reliable comparison to the pulse temporal traces after propagation through the fiber. The temporal trace of the pulses after propagating 30 km and 60 km of fiber are represented in figures A.11(c) and A.11(d), respectively. As in the previous section, the rectangular pulses experienced a shape change by propagating through the SMF as depicted in both figures

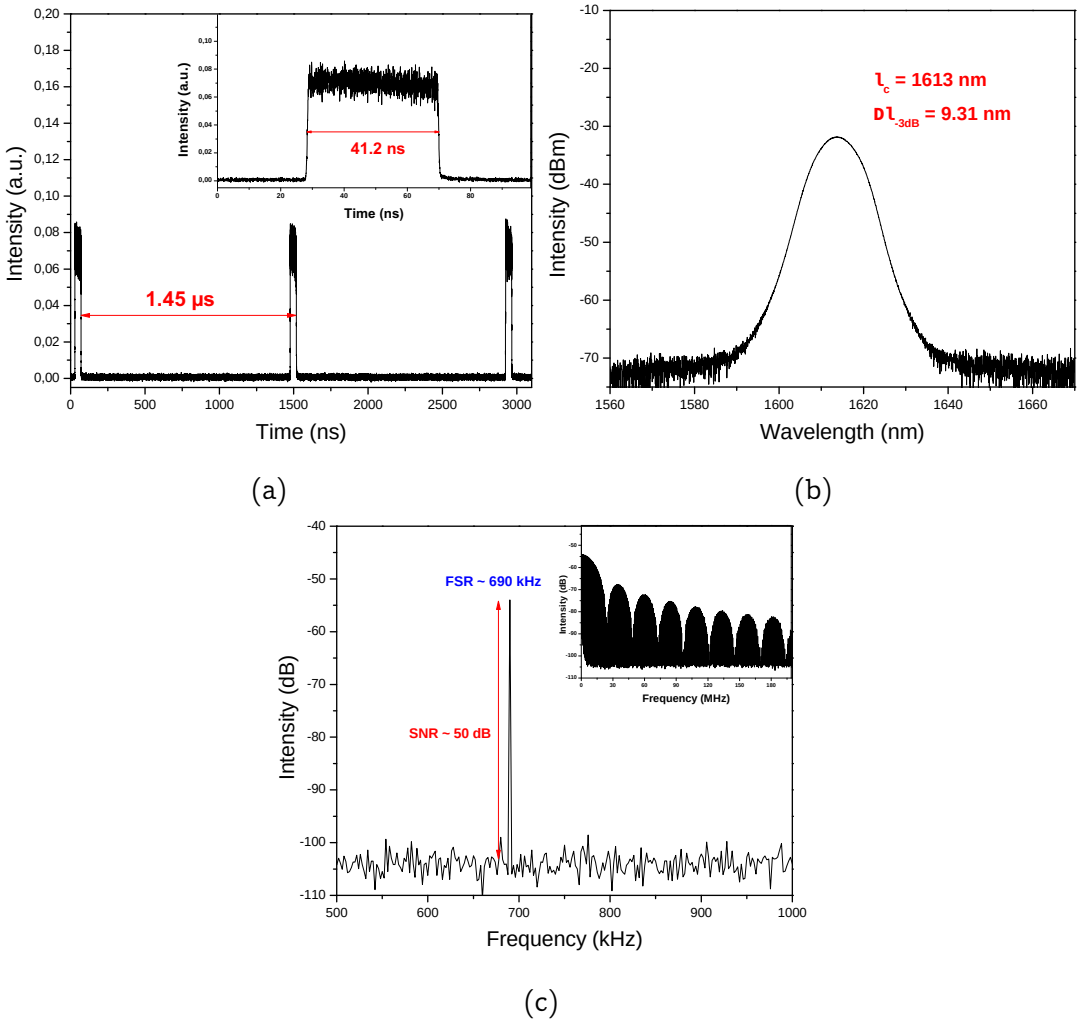

Figure A.9: (a) Temporal trace of rectangular pulses, (b) the corresponding optical spectrum, and (c) the radio-frequency trace.

A.11(a) and A.11(b) after 30 km and 60 km, respectively. One can note that at a pump power of 1.27 W for example, the pulse represented by a blue curve still has a flat top in figure A.11(c) after propagating through 30 km of fiber. In parallel, at the same pump power, as shown in figure A.11(b) after propagating through 60 km of fiber, the temporal profile mimics a Gaussian profile.

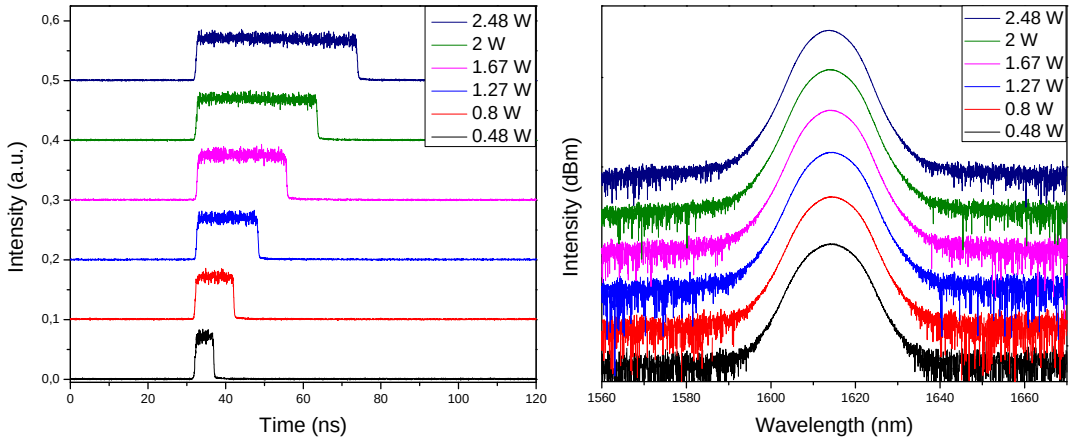

(a) (b)

Figure A.10: (a) Temporal trace of rectangular pulses for pump power ranging from 0.8 W to 4.02 W. (b) The corresponding optical spectrum for the same range of pump power.

Pump power $[W]$	Initial T_{pulse} [ns]	Initial $\Delta\lambda$ [nm]	30 km SMF		60 km SMF	
			$\Delta\tau_{meas}$ [ns]	$\Delta\lambda_{calc}$ [nm]	$\Delta\tau_{meas}$ [ns]	$\Delta\lambda_{calc}$ [nm]
0.48	4.75	10.5	5.33	10.46	9.64	9.45
0.8	9.75	10.16	7.52	14.75	9.88	9.69
1.27	15.64	9.94	13.02	25.53	15.37	15.07
1.67	23.03	9.72	19.77	38.76	19.02	18.65
2	30.91	9.52	27.55	54.02	25.36	24.86
2.48	41.24	9.31	37.88	74.27	35.5	34.80

Table A.3: Pulse duration of initial rectangular pulses at the output of the laser cavity and their evolution after propagating through the 30 km and 60 km of SMF coil.

Table A.3 summarizes the duration evolution of the pulses after propagating in the fiber coil. Figure A.12 represents the width of each pulse before and after propagation for each pump power. One can note that for the shortest pulse plotted in red, the pulse width increases from 4.75 ns to 5.33 ns at 30 km and continues to increase to 9.64 ns at 60 km of SMF28. For a larger pulse whose

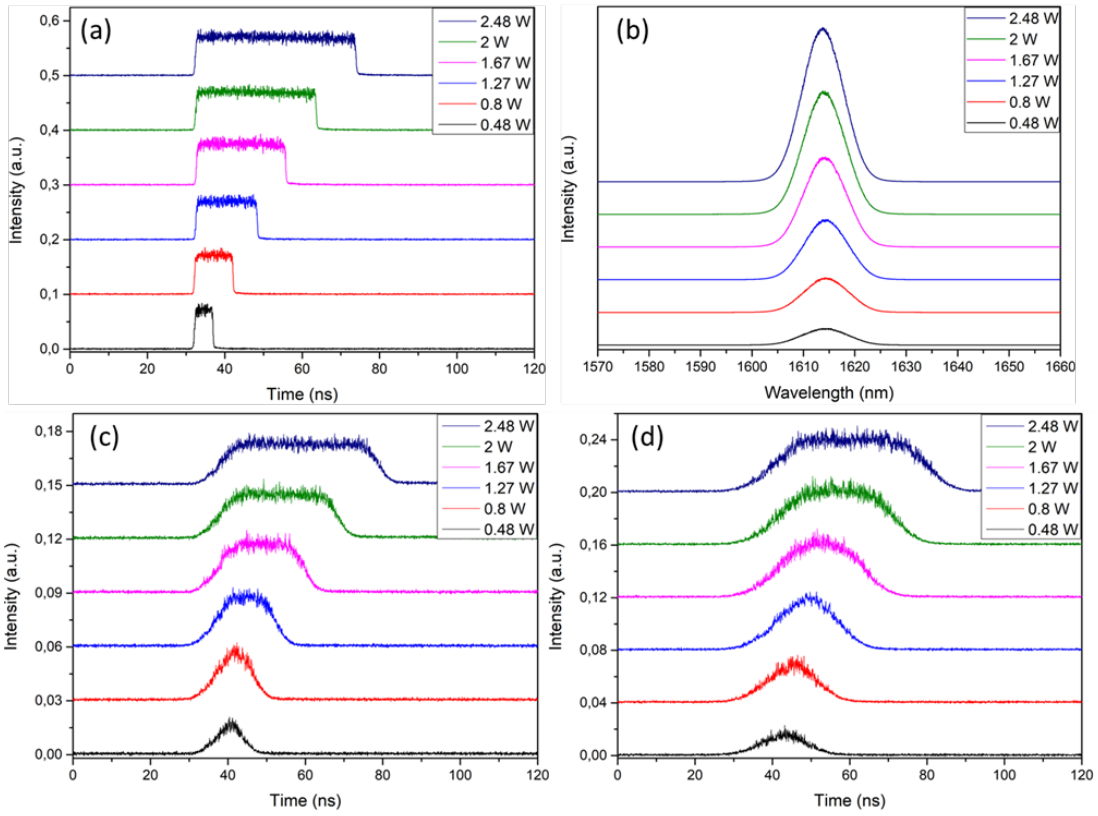

Figure A.11: (a) Temporal traces of the rectangular pulses for different pump powers, ranging from 0.48 W to 3.64 W, at the output of the laser. (b) The corresponding optical spectrum with a linear scale. (c) The temporal trace of the rectangular pulses at the output of 30 km of fiber and (d) at the output of 60 km of fiber.

initial width is 9.75 ns, represented in black, its width first decreased to 7.52 ns at 30 km to increase again to 9.88 ns at 60 km. The same tendency is observed for the third pulse in blue with an initial duration of 15.64 ns. The duration of larger pulses only decreases after propagation. For the shortest two pulses in red and black, we confirm the tendency of the pulse width to widen.

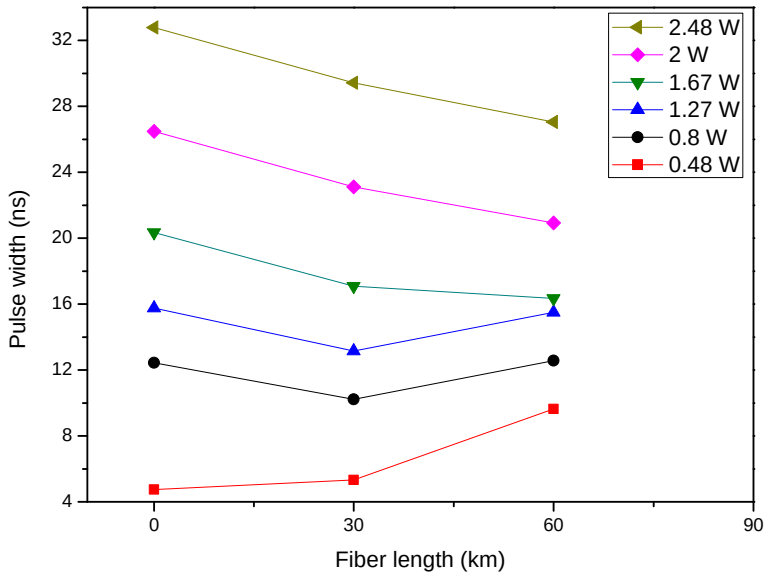

Figure A.12: The pulse width of the initial pulses and their duration after propagating through 30 km and then 60 km of SMF28, for the different pump power output pulses, ranging from 0.48 W to 2.48 W.

A.2.3 Simulation results

In the following, I make the same study as for the pulse with 6.5 ns duration. The results are shown in the following figures. Figure A.13a corresponds to the case of negative initial chirp parameter C = -13000. As for the case of the pulse studied in the previous section, the apparent FWHM is narrowed, however, the pulse exhibits widened wings. Figure A.13b displayed the results for a positive C = +13000, where the pulse narrows and exhibits many oscillations, with higher intensity at the edges of the pulse, which is, as discussed in the previous section, due to the higher chirp at the edges of the super-gaussian pulse. Besides the oscillations, we note that the pulse narrows and no wings are surpassing the initial pulse.

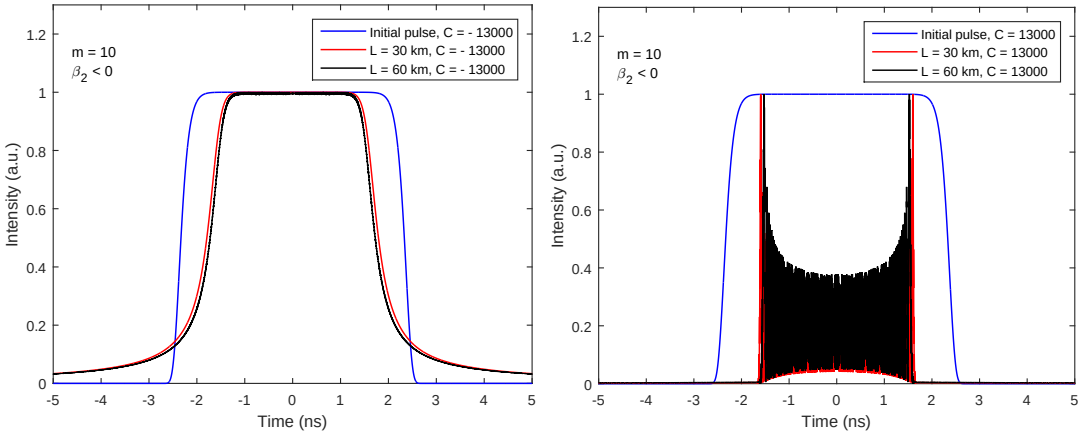

(a) (b)

Figure A.13: (a) Temporal trace of the initial rectangular pulse, with a negative initial chirp parameter C= -13000, in blue, and after propagating through 30 km and 60 km of SMF28 in red and black, respectively. (b) Same temporal traces for a positive C = +13000.

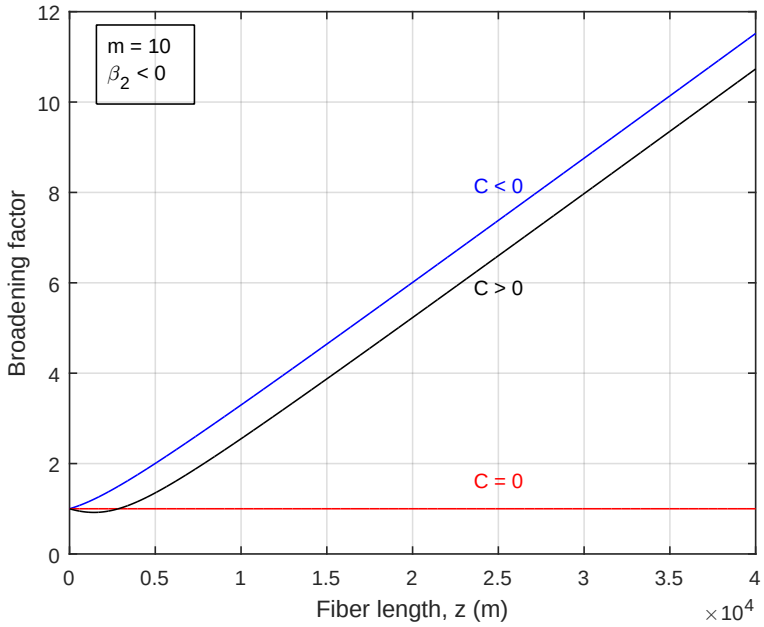

Figure A.14: Broadening factor as a function of the fiber length z, with anomalous-GVD parameter ($\beta_2 < 0$), for a super-gaussian pulse (m = 10) with different values of the chirp parameter: C = 0 in red, C= +13000 in black, and C= -13000 in blue.

Figure A.14 represents the broadening factor versus the fiber length. Once again I compare the broadening factor obtained analytically using the equation (Eq.A.10), with the broadening factor calculated from simulated pulses. The results are summarized in the following table A.4

Broadening	At z=2.1 km		At z=30 km		At z=60 km	
factor, $\frac{\sigma}{\sigma_0}$	Eq.A.10	Simul.	Eq.A.10	Simul.	Eq.A.10	Simul.
C = -13000	1.3408	1.3407	8.7577	8.7100	17.0471	15.6081
C = 0	1	1	1	1	1	1
C = 13000	0.9380	0.9380	7.9738	7.9282	16.2617	14.8515

Table A.4: Broadening factor, $\frac{\sigma}{\sigma_0}$, at fiber length of z = 2.1 km, 30 km, and 60 km, for different values of the chirp parameter C = -13000; 0; +13000.

The values from Eq.A.10 and simulations are similar even if for relatively high fiber length (here z = 60 km), there starts to be a small difference due to a weaker resolution in the simulation pulses. Nevertheless, the simulations are validated. Thus, comparing the experimental rectangular pulses to those obtained in simulations, it seems that the behavior is different, both in terms of shape and pulse width if the reasoning is based on the apparent FWHM.

A.3 Conclusion

Comparing the experimental pulses and simulation results, we can conclude that the behavior of the pulses after propagating 30 km of fiber is not similar, in both the shape and duration of the pulses. For both negative and positive chirps, the resulting pulses are different. To conclude, the experimental pulses seem to don't behave as a unique highly chirped super-gaussian pulse that should evolve after propagating through 30 km of SMF fiber. Thus, either the pulse is not unique but consists of an envelope of fine structures, or the simulation model is not complete and does not reflect the real experimental characteristics of the pulse. Another hypothesis is that the experimental pulse

may have experienced a smoothing from the acquisition system so the shape is altered. The study requires more investigation to get a satisfying conclusion, and one of the solutions may be the use of dispersion compensating fiber (DCF) with which the needed length would be less important than using SMF. Also, the model of simulations may be upgraded to better represent a real DSR pulse. It will be also interesting to simulate a packet of fine structures and see if the behavior after propagation in fiber would correspond to the experimental results.

Bibliography

[1] J. P. Gordon, H. J. Zeiger, and C. H. Townes. "The Maser—New Type of Microwave Amplifier, Frequency Standard, and Spectrometer". In: *Phys. Rev.* 99 (4 Aug. 1955), pp. 1264–1274. DOI: 10.1103/PhysRev.99.1264.

[2] A. L. Schawlow and C. H. Townes. "Infrared and Optical Masers". In: *Phys. Rev.* 112 (6 Dec. 1958), pp. 1940–1949. DOI: 10.1103/PhysRev.112.1940.

[3] T. H. MAIMAN. "Stimulated Optical Radiation in Ruby". In: *Nature* 187.4736 (Aug. 1960), pp. 493–494. DOI: 10.1038/187493a0.

[4] E. Snitzer. "Proposed Fiber Cavities for Optical Masers". In: *Journal of Applied Physics* 32.1 (1961), pp. 36–39. DOI: 10.1063/1.1735955.

[5] C. J. Koester and E. Snitzer. "Amplification in a Fiber Laser". In: *Appl. Opt.* 3.10 (Oct. 1964), pp. 1182–1186. DOI: 10.1364/AO.3.001182.

[6] J. E. Geusic, H. M. Marcos, and L. G. Van Uitert. "LASER OSCILLATIONS IN Nd-DOPED YTTRIUM ALUMINUM, YTTRIUM GALLIUM AND GADOLINIUM GARNETS". In: *Applied Physics Letters* 4.10 (1964), pp. 182–184. DOI: 10.1063/1.1753928.

[7] E. Snitzer and R. Woodcock. "Yb3+–Er3+ GLASS LASER". In: *Applied Physics Letters* 6.3 (1965), pp. 45–46. DOI: 10.1063/1.1754157.

[8] J. Stone and C. Burrus. "Neodymium-doped silica lasers in end-pumped fiber geometry". In: *Applied Physics Letters* 23.7 (1973), pp. 388–389. DOI: 10.1063/1.1654929.

[9] S. B. Poole, D. N. Payne, and M. Fermann. "Fabrication of low-loss optical fibres containing rare-earth ions". In: *Electronics Letters* 17.21 (1985), pp. 737–738.

[10] R. J. Mears, L. Reekie, I. M. Jauncey, and D. N. Payne. "Low-noise erbium-doped fibre amplifier operating at 1.54μm". In: *Electronics Letters* 23 (1987), pp. 1026–1028.

[11] A. A. Boni, D. I. Rosen, S. J. Davis, and L. A. Popper. "High-power laser applications to medicine". In: *Journal of Quantitative Spectroscopy and Radiative Transfer* 40.3 (1988). Special Issue on Quantitative Spectroscopy and Laser Diagnostics, pp. 449–467. DOI: https://doi.org/10.1016/0022-4073(88)90133-1.

[12] R. Waynant, I. Ilev, I. Gannot, J. Meyer, and C. Sirtori. "Mid-infrared laser applications in medicine and biology". English (US). In: *Philosophical transactions. Series A, Mathematical, physical, and engineering sciences* 359.1780 (Mar. 2001), pp. 635–644. DOI: 10.1098/rsta.2000.0747.

[13] Q. Peng, A. Juzeniene, J. Chen, L. O. Svaasand, T. Warloe, K.-E. Giercksky, et al. "Lasers in medicine". In: *Reports on Progress in Physics* 71.5 (Apr. 2008), p. 056701. DOI: 10.1088/0034-4885/71/5/056701.

[14] L. Dombrovsky, V. Timchenko, and G. Jackson MichaelandYeoh. "A combined transient thermal model for laser hyperthermia of tumors with embedded gold nanoshells". In: *International Journal of Heat and Mass Transfer* 54 (Dec. 2011), pp. 5459–5469. DOI: 10.1016/j.ijheatmasstransfer.2011.07.045.

[15] M.Eichhorn. "Pulsed 2 um fiber lasers for direct and pumping applications in defense and security," in: *Proc.SPIE 7836, Technologies for Optical Countermeasures VII,78360B* (2010).

[16] M. Silver, S. T. Lee, A. Borthwick, I. McRae, D. Jackson, and W. Alexander. "Compact, diode-pumped, solid-state lasers for next generation defense and security sensors," in: *Journal of Physics: Conference Series* 619.1 (May 2015), p. 012022. DOI: 10.1088/1742-6596/619/1/012022.

[17] F. Gagliano, R. Lumley, and L. Watkins. "Lasers in industry". In: *Proceedings of the IEEE* 57.2 (1969), pp. 114–147. DOI: 10.1109/PROC.1969.6908.

[18] D. Strickland and G. Mourou. "Compression of amplified chirped optical pulses". In: *Optics Communications* 56.3 (1985), pp. 219–221. DOI: https://doi.org/10.1016/0030-4018(85)90120-8.

[19] A. F. T. F. A. P. A. F. F. K. A. Apolonski. "Chirped-pulse oscillators:a route to high-power femtosecond pulses without external amplification". In: *Opt.Lett.* 29.12 (June 2004), pp. 1366–1368. DOI: 10.1364/OL.29.001366.

[20] K. Tamura, E. P. Ippen, H. A. Haus, and L. E. Nelson. "77-fs pulse generation from a stretched-pulse mode-locked all-fiber ring laser". In: *Opt. Lett.* 18.13 (July 1993), pp. 1080–1082. DOI: 10.1364/OL.18.001080.

[21] F. Ö. Ilday, J. R. Buckley, W. G. Clark, and F. W. Wise. "Self-Similar Evolution of Parabolic Pulses in a Laser". In: *Phys. Rev. Lett.* 92 (21 May 2004), p. 213902. DOI: 10.1103/PhysRevLett.92.213902.

[22] A. Chong, W. H. Renninger, and F. W. Wise. "Properties of normal dispersion femtosecond fiber lasers". In: *J.Opt.Soc.Am.B* 25.2 (Feb. 2008), pp. 140–148. DOI: 10.1364/JOSAB.25.000140.

[23] W. Chang, A. Ankiewicz, J. Soto-Crespo, and N. Akhmediev. "Dissipative soliton resonances". In: *Phys.Rev.A* 78 (2 Aug. 2008), p. 023830. DOI: 10.1103/PhysRevA.78.023830.

[24] W. Chang, J. Soto-Crespo, A. Ankiewicz, and N. Akhmediev. "Dissipative soliton resonances in the anomalous dispersion regime". In: *Phys.Rev.A* 79 (3 Mar. 2009), p. 033840. DOI: 10.1103/PhysRevA.79.033840.

[25] X. Liu. "Pulse evolution without wave breaking in a strongly-dissipative laser system". In: *Phys.Rev.A* 81 (5 May 2010), p. 053819. DOI: 10.1103/PhysRevA.81.053819.

[26] P. Grelu, W. Chang, A. Ankiewicz, J. M.Soto-Crespo, and N. Akhmediev. "Dissipative soliton resonance as a guideline for high-energy pulse laser oscillators". In: *J.Opt.Soc.Am.B* 27.11 (Nov. 2010), pp. 2336–2341. DOI: 10.1364/JOSAB.27.002336.

[27] E. Ding, P. Grelu, and J. Kutz. "Dissipative soliton resonance in a passively mode-locked fiber laser". In: *Opt. Lett.* 36.7 (Apr. 2011), pp. 1146–1148. DOI: 10.1364/OL.36.001146.

[28] F. Bahloul, G. Khmaies, M. Salhi, F. Sanchez, and R. Attia. "Control of the square pulse properties in figure-of-eight microstructured fiber laser". In: *Optical Engineering* 55 (Feb. 2016), p. 026102. DOI: 10.1117/1.OE.55.2.026102.

[29] A. Komarov, A. Dmitriev, K. Komarov, D. Meshcheriakov, and F. Sanchez. "Spectral-doublet rectangular pulses in passive mode-locked fiber lasers with anomalous dispersion". In: *Phys.Rev.A* 94 (4 Oct. 2016), p. 043827. DOI: 10.1103/PhysRevA.94.043827.

[30] C. Liu, Q. Wu, Y. Yao, C. W. Y. Gan, Y. Fu, Y. Yang, et al. "Numerical research on the dissipative-soliton-resonance peak power in normal-dispersion fiber lasers". In: 474 (2020), p. 126163. DOI: https://doi.org/10.1016/j.optcom.2020.126163.

[31] X. W. D. Y. T. H. Z. L. M. Zhao. "Dissipative soliton resonance in an all-normal dispersion erbium-doped fiber laser". In: *Opt. Express* 17.7 (Mar. 2009), pp. 5580–5584. DOI: 10.1364/OE.17.005580.

[32] R. Becheker, M. Tang, M. Touil, T. Robin, B. Cadier, M. Laroche, et al. "Dissipative soliton resonance in a mode-locked Nd-fiber laser operating at 927 nm". In: *Opt. Lett.* 44.22 (Nov. 2019), pp. 5497–5500. DOI: 10.1364/OL.44.005497.

[33] X. Li, X. Liu, X. Hu, L. Wang, H. Lu, Y. Wang, et al. "Long-cavity passively mode-locked fiber ring laser with high-energy rectangular-shape pulses in anomalous dispersion regime". In: *Opt. Lett.* 35.19 (Oct. 2010), pp. 3249–3251. DOI: 10.1364/OL.35.003249.

[34] J.-h. Yang, C.-y. Guo, S.-c. Ruan, D.-q. Ouyang, H.-q. Lin, Y.-m. Wu, et al. "Observation of Dissipative Soliton Resonance in a Net-Normal Dispersion Figure-of-eight Fiber Laser". In: *IEEE Photonics Journal* 5.3 (2013), pp. 1500806–1500806. DOI: 10.1109/JPHOT.2013.2265982.

[35] S.-K. Wang, Q.-Y. Ning, A.-P. Luo, Z.-B. Lin, Z.-C. Luo, and W.-C. Xu. "Dissipative soliton resonance in a passively mode-locked figure-eight fiber laser". In: *Opt. Express* 21.2 (Jan. 2013), pp. 2402–2407. DOI: 10.1364/OE.21.002402.

[36] N. Zhao, M. Liu, H. Liu, X.-W. Zheng, Q.-Y. Ning, A.-P. Luo, et al. "Dual-wavelength rectangular pulse Yb-doped fiber laser using a microfiber-based graphene saturable absorber". In: *Opt. Express* 22.9 (May 2014), pp. 10906–10913. DOI: 10.1364/OE.22.010906.

[37] K. Krzempek. "Dissipative soliton resonances in all-fiber Er-Yb double clad figure-8 laser". In: *Opt. Express* 23.24 (Nov. 2015), pp. 30651–30656. DOI: 10.1364/OE.23.030651.

[38] K. Krzempek, J. Sotor, and K. Abramski. "Compact all-fiber figure-9 dissipative soliton resonance mode-locked double-clad Er:Yb laser". In: *Opt. Lett.* 41.21 (Nov. 2016), pp. 4995–4998. DOI: 10.1364/OL.41.004995.

[39] G. Semaan, F. BenBraham, J. Fourmont, M. Salhi, F. Bahloul, and F. Sanchez. "10uJ dissipative soliton resonance square pulse in a dual amplifier figure of eight double clad Er:Yb mode-locked fiber laser". In: *Optics Letters* 41 (Oct. 2016), pp. 4767–4770. DOI: 10.1364/OL.41.004767.

[40] G. Semaan, A. Niang, M. Salhi, and F. Sanchez. "Harmonic dissipative soliton resonance square pulses in an anomalous dispersion passively mode-locked fiber ring laser". In: *Laser Physics Letters* 14.5 (Mar. 2017), p. 055401. DOI: 10.1088/1612-202X/aa6700.

[41] L. Mei, G. Chen, L. Xu, X. Zhang, C. Gu, B. Sun, et al. "Width and amplitude tunable square-wave pulse in dual-pump passively mode-locked fiber laser". In: *Opt. Lett.* 39.11 (June 2014), pp. 3235–3237. DOI: 10.1364/OL.39.003235.

[42] F. Bahloul, K. Guesmi, M. Salhi, F. Sanchez, and R. Attia. "Control of the square pulse properties in figure-of-eight microstructured fiber laser". In: *Optical Engineering* 55.2 (2016), p. 026102. DOI: 10.1117/1.OE.55.2.026102.

[43] V.J.Matsas, D.J.Richardson, T.P.Newson, and D.N.Payne. "Characterization of a self-starting, passively mode-locked fiber ring laser that exploits nonlinear polarization evolution". In: *Opt.Lett.* 18.5 (Mar. 1993), pp. 358–360. DOI: 10.1364/OL.18.000358.

[44] J. Liu, Y. Chen, P. Tang, C. Xu, C. Zhao, H. Zhang, et al. "Generation and evolution of mode-locked noise-like square-wave pulses in a large-anomalous-dispersion Er-doped ring fiber laser". In: *Opt. Express* 23.5 (Mar. 2015), pp. 6418–6427. DOI: 10.1364/OE.23.006418.

[45] Z. Dou, B. Zhang, S. Liu, P. Guo, and J. Hou. "Switchable noise-like square pulses generation at 1.61 m with a record output power". In: *Applied Physics Express* 13.5 (Apr. 2020), p. 052005. DOI: 10.35848/1882-0786/ab84bc.

[46] T. Dong, J. Lin, Y. Zhou, C. Gu, P. Yao, and L. Xu. "Noise-like square pulses in a linear-cavity NPR mode-locked Yb-doped fiber laser". In: *Optics Laser Technology* 136 (2021), p. 106740. DOI: https://doi.org/10.1016/j.optlastec.2020.106740.

[47] L. Duan, X. Liu, D. Mao, L. Wang, and G. Wang. "Experimental observation of dissipative soliton resonance in an anomalous dispersion fiber laser". In: *Opt. Express* 20.1 (Jan. 2012), pp. 265–270. DOI: 10.1364/OE.20.000265.

[48] M. Kemel, M. Salhi, C. Ciret, G. Semaan, A. Nady, and F. Sanchez. "Coherence characterization of nanosecond rectangular pulses in passively mode-locked fiber lasers". In: *OSA Continuum* 4.2 (Feb. 2021), pp. 279–289. DOI: 10.1364/OSAC.415474.

[49] M. Ito and T. Kimura. "Stationary and transient thermal properties of semiconductor laser diodes". In: *IEEE Journal of Quantum Electronics* 17.5 (1981), pp. 787–795. DOI: 10.1109/JQE.1981.1071174.

[50] S. Kobayashi, Y. Yamamoto, M. Ito, and T. Kimura. "Direct Frequency Modulation In AlGaAs Semiconductor Lasers". In: *IEEE Transactions on Microwave Theory and Techniques* 30.4 (1982), pp. 428–441. DOI: 10.1109/TMTT.1982.1131084.

[51] A. Zadok, H. Shalom, M. Tur, W. Cornwell, and I. Andonovic. "Spectral shift and broadening of DFB lasers under direct modulation". In: *Photonics Technology Letters, IEEE* 10 (Jan. 1999), pp. 1709–1711. DOI: 10.1109/68.730477.

[52] M. Haney and D. Psaltis. "Measurement of the temporal coherence properties of pulsed single-mode laser diodes". In: *Appl. Opt.* 24.13 (July 1985), pp. 1926–1932. DOI: 10.1364/AO.24.001926.

[53] A. E. H. Oehler, S. C. Zeller, K. J. Weingarten, and U. Keller. "Broad multiwavelength source with 50 GHz channel spacing for wavelength division multiplexing applications in the telecom C band". In: *Opt. Lett.* 33.18 (Sept. 2008), pp. 2158–2160. DOI: 10.1364/OL.33.002158.

[54] G. Ivanovs, V. Bobrovs, S. Olonkins, A. Alsevska, L. Gegere, R. Parts, et al. "Application of the erbium-doped fiber amplifier (ADFA) in wavelength division multiplexing (WDM) transmission systems". In: *Int. J. Phys. Sci.* 9(5).18 (Mar. 2014), pp. 95–101.

[55] S. Diaz, N. Fabian, A. Socorro Leránoz, and I. Matias. "Temperature Sensor Using a Multiwavelength Erbium-Doped Fiber Ring Laser". In: *Journal of Sensors* 2017 (July 2017), pp. 1–6. DOI: 10.1155/2017/8187451.

[56] S. Sarkar, M. Tarhani, M. Khosravi Eghbal, and M. Shadaram. "Discrimination between strain and temperature effects of a single fiber Bragg grating sensor using sidelobe power". In: *Journal of Applied Physics* 127.11 (2020), p. 114503. DOI: 10.1063/1.5139041.

[57] R. B. Chen, J. B. Wang, C. C. Su, H. W. Gu, C. Y. Li, H. H. Lu, et al. "Microwave Photonic Signal Processing Based on Tunable Multi-Wavelength Fiber Laser". In: *Advanced Photonics for Communications*. Optica Publishing Group, 2014, JT3A.2.

[58] B. Wang, G. Somesfalean, L. Mei, H. Zhou, C. Yan, and S. He. "Detection of gas concentration by correlation spectroscopy using a multi-wavelength fiber laser". In: *Progress in Electromagnetics Research* 114 (Jan. 2011), pp. 469–479. DOI: 10.2528/PIER11013106.

[59] Y. Yao, X. Chen, Y. Dai, and S. Xie. "Dual-wavelength erbium-doped fiber laser with a simple linear cavity and its application in microwave generation". In: *IEEE Photonics Technology Letters* 18.1 (2006), pp. 187–189. DOI: 10.1109/LPT.2005.861309.

[60] N. Park, J. Dawson, and K. Vahala. "Multiple wavelength operation of an erbium-doped fiber laser". In: *IEEE Photonics Technology Letters* 4.6 (1992), pp. 540–541. DOI: 10.1109/68.141960.

[61] K. Hotate. "Multiwavelength erbium-doped fibre laser using intracavity etalon and cooled by liquid nitrogen". English. In: *Electronics Letters* 32 (14 July 1996), 1298–1299(1).

[62] R. Hayashi, S. Yamashita, and T. Saida. "16-wavelength 10-GHz actively mode-locked fiber laser with demultiplexed outputs anchored on the ITU-T grid". In: *IEEE Photonics Technology Letters* 15.12 (2003), pp. 1692–1694. DOI: 10.1109/LPT.2003.819762.

[63] O. Graydon, W. Loh, R. Laming, and L. Dong. "Triple-frequency operation of an Er-doped twincore fiber loop laser". In: *IEEE Photonics Technology Letters* 8.1 (1996), pp. 63–65. DOI: 10.1109/68.475779.

[64] S. Yamashita and Y. Inoue. "Multiwavelength Er-doped fiber ring laser incorporating highly nonlinear fiber". In: *Conference on Lasers and Electro-Optics/International Quantum Electronics Conference and Photonic Applications Systems Technologies*. Optica Publishing Group, 2004, p. CMD6.

[65] X. Liu, X. Yang, F. Lu, J. Ng, X. Zhou, and C. Lu. "Stable and uniform dual-wavelength erbium-doped fiber laser based on fiber Bragg gratings and photonic crystal fiber". In: *Opt. Express* 13.1 (Jan. 2005), pp. 142–147. DOI: 10.1364/OPEX.13.000142.

[66] A. Zhang, H. Liu, M. Demokan, and H. Tam. "Stable and broad bandwidth multiwavelength fiber ring laser incorporating a highly nonlinear photonic crystal fiber". In: *IEEE Photonics Technology Letters* 17.12 (2005), pp. 2535–2537. DOI: 10.1109/LPT.2005.859542.

[67] A. Bellemare, M. Karasek, M. Rochette, S. LRochelle, and M. Tetu. "Room temperature multifrequency erbium-doped fiber lasers anchored on the ITU frequency grid". In: *Journal of Lightwave Technology* 18.6 (2000), pp. 825–831. DOI: 10.1109/50.848393.

[68] K. Zhou, D. Zhou, F. Dong, and N. Q. Ngo. "Room-temperature multiwavelength erbium-doped fiber ring laser employing sinusoidal phase-modulation feedback". In: *Opt. Lett.* 28.11 (June 2003), pp. 893–895. DOI: 10.1364/OL.28.000893.

[69] J. Yao, J. Yao, Z. Deng, and J. Liu. "Investigation of room-temperature multiwavelength fiber-ring laser that incorporates an SOA-based phase modulator in the laser cavity". In: *Journal of Lightwave Technology* 23.8 (2005), pp. 2484–2490. DOI: 10.1109/JLT.2005.850818.

[70] Y. Zhao, C. Shu, S. Li, H. Ding, and K. Chan. "Multiple wavelength operation of a unidirectional Er-doped fiber ring laser with optical feedback". In: *CLEO '97., Summaries of Papers Presented at the Conference on Lasers and Electro-Optics*. Vol. 11. 1997, pp. 396–396. DOI: 10.1109/CLEO.1997.603327.

[71] G. Cowle and D. Stepanov. "Multiple wavelength generation with Brillouin/erbium fiber lasers". In: *IEEE Photonics Technology Letters* 8.11 (1996), pp. 1465–1467. DOI: 10.1109/68.541551.

[72] S. Pan, C. Lou, and Y. Gao. "Multiwavelength erbium-doped fiber laser based on inhomogeneous loss mechanism by use of a highly nonlinear fiber and a Fabry-Perot filter". In: *Opt. Express* 14.3 (Feb. 2006), pp. 1113–1118. DOI: 10.1364/OE.14.001113.

[73] B. Liu, Y. Liu, Y. Luo, Y. Xiang, P. P. Shum, X. Tang, et al. "Coexistence of soliton singlets and molecules in a dual-wavelength mode-locked fiber laser". In: *Optics Communications* 457 (2020), p. 124700. DOI: https://doi.org/10.1016/j.optcom.2019.124700.

[74] Y. Meng, M. Salhi, A. Niang, K. Guesmi, G. Semaan, and F. Sanchez. "Mode-locked Er:Yb-doped double-clad fiber laser with 75-nm tuning range". In: *Opt. Lett.* 40.7 (Apr. 2015), pp. 1153–1156. DOI: 10.1364/OL.40.001153.

[75] N. Akhmediev, J. M. Soto-Crespo, and G. Town. "Pulsating solitons, chaotic solitons, period doubling, and pulse coexistence in mode-locked lasers: Complex Ginzburg-Landau equation approach". In: *Phys. Rev. E* 63 (5 Apr. 2001), p. 056602. DOI: 10.1103/PhysRevE.63.056602.

[76] D. Tang, L. Zhao, G. Xie, and L. Qian. "Coexistence and competition between different soliton-shaping mechanisms in a laser". In: *Phys. Rev. A* 75 (June 2007), p. 063810. DOI: 10.1103/PhysRevA.75.063810.

[77] L. Wang. "Coexistence and evolution of bright pulses and dark solitons in a fiber laser". In: *Optics Communications* 297 (2013), pp. 129–132. DOI: https://doi.org/10.1016/j.optcom.2013.02.009.

[78] F. Amrani, M. Salhi, H. Leblond, A. Haboucha, and F. Sanchez. "Intricate solitons state in passively mode-locked fiber lasers". In: *Opt. Express* 19.14 (July 2011), pp. 13134–13139. DOI: 10.1364/OE.19.013134.

[79] X. Liu. "Coexistence of strong and weak pulses in a fiber laser with largely anomalous dispersion". In: *Opt. Express* 19.7 (Mar. 2011), pp. 5874–5887. DOI: 10.1364/OE.19.005874.

[80] Y. Wang, J. Li, E. Zhang, K. Mo, Y. Wang, F. Liu, et al. "Coexistence of noise-like pulse and high repetition rate harmonic mode-locking in a dual-wavelength mode-locked Tm-doped fiber laser". In: *Opt. Express* 25.15 (July 2017), pp. 17192–17200. DOI: 10.1364/OE.25.017192.

[81] Y. Wang, J. Li, L. Hong, G. Li, F. Liu, X. Zhou, et al. "Coexistence of dissipative soliton and stretched pulse in dual-wavelength mode-locked Tm-doped fiber laser with strong third-order dispersion". In: *Opt. Express* 26.14 (July 2018), pp. 18190–18201. DOI: 10.1364/OE.26.018190.

[82] M. Kemel, A. Nady, G. Semaan, M. Salhi, and F. Sanchez. "Triple-lobe wavelength fiber laser with a composite-state soliton regime". In: *Optics & Laser Technology* 133 (2021), p. 106519. DOI: https://doi.org/10.1016/j.optlastec.2020.106519.

[83] M. Horowitz and Y. Silberberg. "Nonlinear filtering by use of intensity-dependent polarization rotation in birefringent fibers". In: *Opt. Lett.* 22.23 (Dec. 1997), pp. 1760–1762. DOI: 10.1364/OL.22.001760.

[84] X. Dong, P. Shum, N. Q. Ngo, H.-Y. Tam, and X. Dong. "Output Power Characteristics of Tunable Erbium-Doped Fiber Ring Lasers". In: *J. Lightwave Technol.* 23.3 (Mar. 2005), p. 1334.

[85] K. Guesmi, Y. Meng, A. Niang, P. Mouchel, M. Salhi, F. Bahloul, et al. "1.6 μm emission based on linear loss control in a Er:Yb doped double-clad fiber laser". In: *Opt. Lett.* 39.22 (Nov. 2014), pp. 6383–6386. DOI: 10.1364/OL.39.006383.

[86] Y. Meng, G. Semaan, M. Kemel, M. Salhi, A. Komarov, and F. Sanchez. "Color domains in fiber lasers". In: *Opt. Lett.* 43.20 (Oct. 2018), pp. 5054–5057. DOI: 10.1364/OL.43.005054.

[87] V. J. Matsas, D. J. Richardson, T. P. Newson, and D. N. Payne. "Characterization of a self-starting, passively mode-locked fiber ring laser that exploits nonlinear polarization evolution". In: *Opt. Lett.* 18.5 (Mar. 1993), pp. 358–360. DOI: 10.1364/OL.18.000358.

[88] S. Kelly. "Characteristic sideband instability of periodically amplified average soliton". English. In: *Electronics Letters* 28 (8 Apr. 1992), 806–807(1).

[89] X.-H. Li, Y.-G. Wang, Y.-S. Wang, X.-H. Hu, W. Zhao, X.-L. Liu, et al. "Wavelength-Switchable and Wavelength-Tunable All-Normal-Dispersion Mode-Locked Yb-Doped Fiber Laser Based on Single-Walled Carbon Nanotube Wall Paper Absorber". In: *IEEE Photonics Journal* 4.1 (2012), pp. 234–241. DOI: 10.1109/JPHOT.2012.2183862.

[90] A. Grudinin, D. Richardson, and D. Payne. "Passive harmonic mode-locking of a fibre soliton ring laser". In: *Electronics Letters* 29.21 (1993), pp. 1860–1861.

[91] P. Weiss. "L'hypothèse du champ moléculaire et la propriété ferromagnétique". In: *J. Phys. Theor. Appl.* 6.1 (1907), pp. 661–690. DOI: 10.1051/jphystap:019070060066100.

[92] D. Parpia, B. Tanner, and D. Lord. "Direct optical observation of ferromagnetic domains". In: *Nature* 303 (1983), pp. 684–685. DOI: https://doi.org/10.1038/303684a0.

[93] S. Coen and M. Haelterman. "Domain Wall Solitons in Binary Mixtures of Bose-Einstein Condensates". In: *Phys. Rev. Lett.* 87 (14 Sept. 2001), p. 140401. DOI: 10.1103/PhysRevLett.87.140401.

[94] F. Tsitoura, U. Gietz, A. Chabchoub, and N. Hoffmann. "Phase Domain Walls in Weakly Nonlinear Deep Water Surface Gravity Waves". In: *Phys. Rev. Lett.* 120 (22 June 2018), p. 224102. DOI: 10.1103/PhysRevLett.120.224102.

[95] Z. V. E. and M. A. V. "Polarization domains in nonlinear optics". In: *JEPT Letters* 45 (6 1987), pp. 279–282.

[96] S. Pitois, G. Millot, and S. Wabnitz. "Polarization Domain Wall Solitons with Counterpropagating Laser Beams". In: *Conference on Lasers and Electro-Optics-Europe*. Optica Publishing Group, 1998, CThH43.

[97] M. Haelterman and A. P. Sheppard. "Polarization domain walls in diffractive or dispersive Kerr media". In: *Opt. Lett.* 19.2 (Jan. 1994), pp. 96–98. DOI: 10.1364/OL.19.000096.

[98] X. Li, S. Zhang, H. Han, M. Han, H. Zhang, L. Zhao, et al. "Different polarization dynamic states in a vector Yb-doped fiber laser". In: *Opt. Express* 23.8 (Apr. 2015), pp. 10747–10755. DOI: 10.1364/OE.23.010747.

[99] J. Liu, X. Li, S. Zhang, H. Zhang, P. Yan, M. Han, et al. "Polarization domain wall pulses in a microfiber-based topological insulator fiber laser". In: *Scientific Reports* 6.1 (July 2016), p. 29128. DOI: 10.1038/srep29128.

[100] P. Wang, K. Zhao, X. Xiao, and C. Yang. "Pulse dynamics of dual-wavelength dissipative soliton resonances and domain wall solitons in a Tm fiber laser with fiber-based Lyot filter". In: *Opt. Express* 25.24 (Nov. 2017), pp. 30708–30719. DOI: 10.1364/OE.25.030708.

[101] C. Lecaplain, P. Grelu, and S. Wabnitz. "Polarization-domain-wall complexes in fiber lasers". In: *J. Opt. Soc. Am. B* 30.1 (Jan. 2013), pp. 211–218. DOI: 10.1364/JOSAB.30.000211.

[102] H. Zhang, D. Y. Tang, L. M. Zhao, and X. Wu. "Observation of polarization domain wall solitons in weakly birefringent cavity fiber lasers". In: *Phys. Rev. B* 80 (5 Aug. 2009), p. 052302. DOI: 10.1103/PhysRevB.80.052302.

[103] C. Lecaplain, P. Grelu, and S. Wabnitz. "Dynamics of the transition from polarization disorder to antiphase polarization domains in vector fiber lasers". In: *Phys. Rev. A* 89 (6 June 2014), p. 063812. DOI: 10.1103/PhysRevA.89.063812.

[104] M. Gilles, P.-Y. Bony, J. Garnier, A. Picozzi, M. Guasoni, and . Fatome. "Polarization domain walls in optical fibres as topological bits for data transmission". In: *Nature Photonics* 11.2 (Feb. 2017), pp. 102–107. DOI: 10.1038/nphoton.2016.262.

[105] B. Garbin, J. Fatome, G.-L. Oppo, M. Erkintalo, S. G. Murdoch, and S. Coen. "Dissipative Polarization Domain Walls in a Passive Coherently Driven Kerr Resonator". In: *Phys. Rev. Lett.* 126 (2 Jan. 2021), p. 023904. DOI: 10.1103/PhysRevLett.126.023904.

[106] M. Haelterman and M. Badolo. "Dual-frequency wall solitary waves for nonreturn-to-zero signal transmission in W-type single-mode fibers". In: *Opt. Lett.* 20.22 (Nov. 1995), pp. 2285–2287. DOI: 10.1364/OL.20.002285.

[107] H. Zhang, D. Tang, L. Zhao, and X. Wu. "Dual-wavelength domain wall solitons in a fiber ring laser". In: *Opt. Express* 19.4 (Feb. 2011), pp. 3525–3530. DOI: 10.1364/OE.19.003525.

[108] Z.-B. Lin, A.-P. Luo, S.-K. Wang, H.-Y. Wang, W.-J. Cao, Z.-C. Luo, et al. "Generation of dual-wavelength domain-wall rectangular-shape pulses in HNLF-based fiber ring laser". In: *Optics & Laser Technology* 44.7 (2012), pp. 2260–2264. DOI: https://doi.org/10.1016/j.optlastec.2012.02.029.

[109] L. Zhi-Chao, L. Zhen-Bin, L. Jin-Yu, Z. Peng-Fei, N. Qiu-Yi, X. Xiao-Bo, et al. "Generation of high-energy dual-wavelength domain wall pulse with low repetition rate in an HNLF-based fiber ring laser". In: *Chinese Physics B* 23.6 (Apr. 2014), p. 064203. DOI: 10.1088/1674-1056/23/6/064203.

[110] Y. Meng, G. Semaan, M. Kemel, M. Salhi, A. Komarov, and F. Sanchez. "Color domains in fiber lasers". In: *Opt. Lett.* 43.20 (Oct. 2018), pp. 5054–5057. DOI: 10.1364/OL.43.005054.

[111] A. Nady, G. Semaan, M. Kemel, M. Salhi, and F. Sanchez. "Polarization-Color Domain Walls in Fiber Ring Lasers". In: *Journal of Lightwave Technology* 38.24 (2020), pp. 6905–6910. DOI: 10.1109/JLT.2020.3021183.

[112] Z.-C. Luo, A.-P. Luo, W.-C. Xu, H.-S. Yin, J.-R. Liu, Q. Ye, et al. "Tunable Multiwavelength Passively Mode-Locked Fiber Ring Laser Using Intracavity Birefringence-Induced Comb Filter". In: *IEEE Photonics Journal* 2.4 (2010), pp. 571–577. DOI: 10.1109/JPHOT.2010.2051023.

[113] B. Liu, Y. Liu, Y. Luo, Y. Xiang, P. P. Shum, X. Tang, et al. "Coexistence of soliton singlets and molecules in a dual-wavelength mode-locked fiber laser". In: *Optics Communications* 457 (2020), p. 124700. DOI: https://doi.org/10.1016/j.optcom.2019.124700.

[114] V. J. Matsas, T. P. Newson, D. J. Richardson, and D. N. Payne. "Selfstarting passively mode-locked fibre ring soliton laser exploiting nonlinear polarisation rotation". In: *Electronics Letters* 28 (1992), pp. 1391–1393.

[115] E. A. Kuzin, J. M. E. Ayala, B. I. Escamilla, and J. W. Haus. "Measurements of beat length in short low-birefringence fibers". In: *Opt. Lett.* 26.15 (Aug. 2001), pp. 1134–1136. DOI: 10.1364/OL.26.001134.

[116] T. Chartier, A. Hideur, C. Özkul, F. Sanchez, and G. M. Stéphan. "Measurement of the elliptical birefringence of single-mode optical fibers". In: *Appl. Opt.* 40.30 (Oct. 2001), pp. 5343–5353. DOI: 10.1364/AO.40.005343.

[117] S. Bielawski, D. Derozier, and P. Glorieux. "Antiphase dynamics and polarization effects in the Nd-doped fiber laser". In: *Phys. Rev. A* 46 (5 Sept. 1992), pp. 2811–2822. DOI: 10.1103/PhysRevA.46.2811.

[118] L. B. Patrice, C. Jaouen, P. François, J. Bayon, F. Sanchez, P. Besnard, et al. "Antiphase dynamics and chaos in self-pulsing erbium-doped fiber lasers". In: *Optics letters* 18 (Nov. 1993), pp. 1890–2. DOI: 10.1364/OL.18.001890.

[119] F. Sanchez, M. LeFlohic, G. Stephan, P. LeBoudec, and P.-L. Francois. "Quasi-periodic route to chaos in erbium-doped fiber laser". In: *IEEE Journal of Quantum Electronics* 31.3 (1995), pp. 481–488. DOI: 10.1109/3.364403.

[120] Y. Jeong, L. A. Vazquez-Zuniga, S. Lee, and Y. Kwon. "On the formation of noise-like pulses in fiber ring cavity configurations". In: *Optical Fiber Technology* 20.6 (2014). Short Pulse Fiber Lasers, pp. 575–592. DOI: https://doi.org/10.1016/j.yofte.2014.07.004.

[121] S. Wabnitz. "Cross-Polarization Modulation Domain Wall Solitons for WDM Signals in Birefringent Optical Fibers". In: *IEEE Photonics Technology Letters* 21.13 (2009), pp. 875–877. DOI: 10.1109/LPT.2009.2019848.

[122] H. Zhang, D. Y. Tang, L. M. Zhao, and R. J. Knize. "Vector dark domain wall solitons in a fiber ring laser". In: *Opt. Express* 18.5 (Mar. 2010), pp. 4428–4433. DOI: 10.1364/OE.18.004428.

[123] C. R. Menyuk. "Stability of solitons in birefringent optical fibers. II. Arbitrary amplitudes". In: *J. Opt. Soc. Am. B* 5.2 (Feb. 1988), pp. 392–402. DOI: 10.1364/JOSAB.5.000392.

[124] G. P. Agrawal. *Nonlinear Fiber Optics*. Academic, New York, 1995.

[125] D. Li, L. li, J. Zhou, L. Zhao, D. Tang, and D. Shen. "Characterization and compression of dissipative-soliton-resonance pulses in fiber lasers". In: *Scientific Reports* 6 (Jan. 2016). DOI: 10.1038/srep23631.

List of Figures

2.1 Illustration of the optical fiber cross-section and the refractive index change along the radial distance 6
2.2 Guidance of a light beam in a step-index optical fiber via total internal reflection at the core-cladding interface. 6
2.3 Energy level diagram of Er-Yb-doped laser. 14
2.4 Schema of the fiber laser cavity passively mode-locked through nonlinear polarization evolution 15

3.1 Experimental configuration of dual-pump figure-8 fiber laser . . 22
3.2 Temporal profile of the generated square-wave pulses with a pump power of A2 fixed at 1.8 W and A1 tuned from 0.5 W to 3 W. 23
3.3 Temporal trace of the generated Square-wave pulses with a pump power of A1 fixed at 3 W and A2 tuned from 120 mW to 1.7 W. 24
3.4 Variation of (a) the pulse peak power (b) the pulse energy (c) and the pulse duration as a function of the pump power of the amplifier A1. 26
3.5 Variation of (a) the pulse peak power (b) the pulse energy (c) and the pulse duration as a function of the pump power of A2. 27
3.6 Variation as a function of L2 position of (a) energy and (b) pulse duration for different values of total cavity dispersion. 28
3.7 Variation of (a) pulse-width (b) and pulse energy as a function of the cavity dispersion for different values of the central coupling ratio k 28
3.8 Experimental setup of the ring cavity. 30

3.9 Harmonic mode-locked DSR square pulses train of different orders achieved by adjusting the PC. Each color is assigned to different pumping power (red for 1.18 W, blue for 1.6 W, and green for 2.2 W). 31

3.10 Experimental setup. EYDFA: Erbium-Ytterbium co-doped fiber Amplifier, OC: optical coupler, PC1,2: polarization controller, PI-ISO: polarization-insensitive isolator. 33

3.11 (a) Temporal trace of rectangular pulses, (b) the corresponding optical spectrum, and (c) the radio-frequency trace, at the pump power of 5.06 W. 34

3.12 (a) Temporal trace of rectangular pulses for pump power ranging from 2.26 W to 5.21 W. (b) The corresponding optical spectra for the same range of pump power in dBm scale (and in linear scale represented in the inset figure). 35

3.13 Characteristics of rectangular pulses. Evolution of the (a) pulse width (red stars linearly fitted by red curve), the peak power (blue dots fitted by linear blue curve), and (b) the pulse energy (red dots with a linear fit curve) with pump power ranging from 2.26 W to 5.21 W. 35

3.14 Temporal trace of rectangular pulses (a), the corresponding optical spectrum (b), and the radio-frequency trace (c). 37

3.15 (a) Temporal trace of rectangular pulses for pump power ranging from 2.26 W to 5.21 W. (b) The corresponding optical spectra for the same range of pump power in dBm, and in linear scale represented in the inset. 38

3.16 Characteristics of rectangular pulses. Evolution of the (a) pulse width (red stars linearly fitted by red curve), the peak power (blue dots fitted by linear blue curve), and (b) the pulse energy (red dots with a linear fit curve) with pump power ranging from 2.26 W to 5.21 W. 38

3.17 Temporal trace of rectangular pulses (a), the corresponding optical spectrum (b), and the radio-frequency trace (c). 39

3.18 (a) Temporal trace of rectangular pulses for pump power ranging from 0.8 W to 4.02 W. (b) The corresponding optical spectrum for the same range of pump power. (c) 3-dB bandwidth of the spectrum as a function of pump power. 40

3.19 Characteristics of rectangular pulses. Evolution of the (a) pulse width (red stars linearly fitted by red curve), the peak power (blue dots fitted by linear blue curve), and (b) the pulse energy (black dots with a linear fit curve) with pump power ranging from 0.8 to 4.02 W. 41

4.1 Schema of Mach-Zehnder interferometer. BS: beam splitter, M: mirror, D: photo-detector 46

4.2 All-fibered MZI experimental setup 48

4.3 (a) Optical spectrum trace of the DFB laser source. (b) Temporal trace of interferometric fringes of the DFB laser at the output of the MZI. 49

4.4 Schematic temporal evolution of the pulse intensity and the envelope, in case of (a) coherent pulses and (b) incoherent pulses. 50

4.5 (a)Temporal trace of the modulated DFB laser at the output of the laser, and (b) the corresponding optical spectrum trace, for different modulation frequencies: 0.5 kHz, 10 kHz, 40 kHz, and 50 kHz. 52

4.6 Temporal trace of the modulated DFB laser at the output of the MZI (a), and the corresponding optical spectra (b), for different modulation frequencies: 0.5 kHz, 10 kHz, 40 kHz, and 50 kHz. 53

4.7 Temporal trace of the modulated DFB laser at the output of the laser (a), and the corresponding optical spectrum trace (b), for modulation frequencies of 10 kHz, and 50 kHz. 54

4.8 Temporal trace of the modulated DFB laser at the output of the MZI (a), and the corresponding optical spectrum trace (b), for modulation frequencies of 10 kHz, and 50 kHz. 54

4.9 Experimental setup. EYDFA, Erbium-Ytterbium co-doped fiber Amplifier; OC, optical coupler; PC, polarization controller; SMF, single-mode fiber; PI-ISO, polarization-insensitive isolator; PZT, Piezoelectric translator; MZI, Mach-Zehnder interferometer 56

4.10 (a) Temporal trace of rectangular pulses, (b) the corresponding optical spectrum, at the pump power of 5.06 W. 56

4.11 (a) Temporal trace of the initial pulse at the output of the laser for a pump power of 5.06 W, and (b) the corresponding temporal trace at the output of the MZI in which this pulse interferes with itself with 2 m of path difference (corresponding to 10 ns time delay). 57

4.12 MZI result at the pump power of 5.06 W. (a) Temporal trace of several pulses along 4 ms, at the output of the MZI. (b) The corresponding temporal envelope consists of the top intensity of each interfering part of the pulse. 58

4.13 Temporal trace of rectangular pulses (a), and the corresponding optical spectrum (b). 59

4.14 (a) Temporal trace of the initial pulse at the output of the laser for a pump power of 5.06 W, and (b) the corresponding temporal trace at the output of the MZI in which this pulse interferes with itself with 2 m of path difference (corresponding to 10 ns time delay). 59

4.15 (a) Temporal traces of the rectangular pulses at the output of the MZI (b) a zoom-in on the square pulses, (c) the temporal envelope consisting of the top intensity of each interfering part of the pulse.. 60

4.16 MZI. OC: optical coupler, PZT: Piezoelectric translator, L1,2: lens, TS: translation stage. 62

4.17 (a) Temporal trace of rectangular pulses, and (b) the corresponding optical spectrum at the pump power of 1.67 W. 63

4.18 (a) Temporal evolution of the interferometry fringes of the 26.5 ns pulses at the pump power of 1.67 W, for different optical delays (ranging from 0 μm – 300 μm), at the output of MZI. (b) The corresponding peak intensity evolution. 64

4.19 Temporal trace of rectangular pulses at the pump power of 4.02 W. 64

4.20 (a) Temporal evolution of the interferometry fringes of the 69 ns pulses at the pump power of 4.02 W, for different optical delays (ranging from 0 μm – 300 μm), at the output of MZI. (b) Intensity envelops of the interferometry fringes. 65

5.1 Experimental setup of an all-fibered unidirectional ring laser cavity: EYDFA, Er:Yb co-doped fiber amplifier; PI-ISO, polarization-independent isolator; SMF, single-mode fiber; PC, polarization controller; OC, optical coupler. 70

5.2 Evolution of the optical spectrum with a logarithmic scale (a), and a linear scale (b) at different values of pump power. (c) The corresponding oscilloscope trace. 72

5.3 (a) Optical spectra at fixed pump power and for different intracavity loss in logarithmic scale and (b) in linear scale. (c) The corresponding temporal traces, with (d) a zoom in from 0 to 140 ns. 74

5.4 (a) Evolution of the spectrum in logarithmic scale and (b) in linear scale, (c) the corresponding oscilloscope trace and, (d) square pulse width, at different values of pump power. 75

5.5 RF spectrum at the pump power of 4 W. Inset: RF spectrum over a 250 MHz span. 76

5.6 Temporal trace of the initial and filtered signals at 0.8 W of pump power 77

5.7 Temporal trace of the initial and filtered signals at 4.02 W of pump power 78

5.8 Optical Spectra (a), and the corresponding temporal traces (b) of harmonic states at the pump power of 3.2 W. 79

5.9 Optical Spectra (a) and the corresponding temporal traces (b) of harmonic states at the pump power of 3.2 W. 80

6.1 Experimental setup of the polarization-color domains: Er:Yb DCF amplifier (Erbium:Ytterbium codoped double-clad fiber amplifier), PI-ISO (isolator), PC (polarization controller), HNLF (highly nonlinear fiber), and OC (output coupler). . . . 83

6.2 Optical characteristics of the dual-wavelength emission at the pump power of 1.9 W: (a) spectral profile, (b) the corresponding oscilloscope trace, and (c) radiofrequency spectrum. 85

6.3 Temporal trace of the initial and filtered signal. 86

6.4 Pulse characteristics for various pump power: (a) spectral evolution, and (b) temporal profile evolution. 87

6.5 Optical spectra (a) and oscilloscope profiles of the total intensity (b) at three different PC orientations. 88

6.6 Spectral profile (linear unit) of the polarization-resolved experiment. 90

6.7 Oscilloscope trace of the polarization-resolved experiment. . . . 91

A.1 Optical spectra in logarithmic (a), and linear (b) scales, for different pump powers ranging from 0.46 W to 4.02 W 97

A.2 Pulse temporal traces for different pump powers (a) at the reference output and (b) at the output of the SMF coil. (c) Rise-time of the initial pulses (red squares fitted with a linear red curve) and after the SMF coil (blue dots fitted with a linear blue curve). 98

A.3 Temporal trace of the initial rectangular pulse at the pump power of 0.46 W represented in black, and the corresponding temporal trace of the pulse at the output of the 30 km SMF coil. The inset figure represents the initial optical spectrum in a linear scale. 99

A.4 Temporal trace of the initial rectangular pulse, with initial chirp parameter C=0, in blue. The red curve represents its propagation through 30 km of SMF28. 102

A.5 (a) Temporal trace of the initial rectangular pulse, with a negative initial chirp parameter $C = -16000$, in blue, and after propagating through 30 km of SMF28 in red. (b) The chirp of the initial pulse. 103

A.6 (a) Temporal trace of the initial rectangular pulse, with a positive initial chirp parameter $C = 16000$, in blue, and after propagating through 30 km of SMF28 in red. (b) The chirp of the initial pulse. 103

A.7 Broadening factor as a function of the fiber length z, with anomalous-GVD parameter ($\beta_2 < 0$), for a super-gaussian pulse ($m = 10$) with different values of the chirp parameter: $C = 0$ in red, $C = +16000$ in black, and $C = -16000$ in blue. 105

A.8 Experimental setup. Optical circulator, OC: optical coupler, SMF 28: single-mode fiber. 107

A.9 (a) Temporal trace of rectangular pulses, (b) the corresponding optical spectrum, and (c) the radio-frequency trace. 108

A.10 (a) Temporal trace of rectangular pulses for pump power ranging from 0.8 W to 4.02 W. (b) The corresponding optical spectrum for the same range of pump power. 109

A.11 (a) Temporal traces of the rectangular pulses for different pump powers, ranging from 0.48 W to 3.64 W, at the output of the laser. (b) The corresponding optical spectrum with a linear scale. (c) The temporal trace of the rectangular pulses at the output of 30 km of fiber and (d) at the output of 60 km of fiber. 110

A.12 The pulse width of the initial pulses and their duration after propagating through 30 km and then 60 km of SMF28, for the different pump power output pulses, ranging from 0.48 W to 2.48 W. 111

A.13 (a) Temporal trace of the initial rectangular pulse, with a negative initial chirp parameter C= -13000, in blue, and after propagating through 30 km and 60 km of SMF28 in red and black, respectively. (b) Same temporal traces for a positive C = +13000.112

A.14 Broadening factor as a function of the fiber length z, with anomalous-GVD parameter ($\beta_2 < 0$), for a super-gaussian pulse (m = 10) with different values of the chirp parameter: C = 0 in red, C= +13000 in black, and C= -13000 in blue. 112

List of Tables

A.1 Estimation of the super-gaussian order m. 101

A.2 Broadening factor, $\frac{\sigma}{\sigma_0}$, at fiber length of z = 2.1 km and 30 km, for different values of the chirp parameter C = -16000; 0; +16000. 106

A.3 Pulse duration of initial rectangular pulses at the output of the laser cavity and their evolution after propagating through the 30 km and 60 km of SMF coil. 109

A.4 Broadening factor, $\frac{\sigma}{\sigma_0}$, at fiber length of z = 2.1 km, 30 km, and 60 km, for different values of the chirp parameter C = -13000; 0; +13000. 113

Publications

Book chapter:

1. Kemel M., Salhi M., Ciret C., Semaan G., and Sanchez F., *« Coherence Characterization of DSR-like Square Pulses in Passively Mode-locked Fiber Lasers »*. Chapter 14 (pp. 575-591) in Advances in Optics, Reviews Book Series volume 5, Sergey Y. Yurish Ed., IFSA (International Frequency Sensor Association) Publishing 2021 (ISBN: 978-84-09-34834-3).

Articles:

1. Kemel M., Mouchel P., Semaan G., Salhi M., Le Flohic M., Sanchez F., *« Deterioration of Graphene Nanocoated Optical Taper Saturable Absorber at High Power »*. Sensors & Transducers, Vol. 233, Issue 5, pp. 1-5. (2019).

2. Kemel M., Nady A., Semaan G., Salhi M., Sanchez F., *« Triple-lobe wavelength fiber laser with a composite-state soliton regime »*. Optics & Laser Technology, Vol. 133, 106519, ISSN 0030-3992. (2021).

3. Kemel M., Salhi M., Ciret C., Semaan G., Nady A, Sanchez F., *« Coherence characterization of nanosecond rectangular pulses in passively mode-locked fiber lasers »*. OSA Continuum 4, 279-289. (2021).

4. Semaan G., Komarov A., Niang A., Meng Y., Kemel M., Salhi M., Sanchez F., *« Theoretical and experimental analysis of staircase pulses in passive mode-locked fiber lasers »*, Phys. Rev. A, 98, 033819. (2018).

5. Meng Y., Semaan G., Kemel M., Salhi M., Komarov A., Sanchez F., *« Color domains in fiber lasers »*. Opt.Lett.43,5054-5057. (2018).

6. Mouchel P., Kemel M., Semaan G., Salhi M., Flohic M., Sanchez F., *« Limitations of graphene nanocoated optical tapers for high power nonlinear applications »*. Optical Materials: X, 1, 100003. (2018).

7. Semaan G., Nady A., Niang A., Kemel M., Salhi M., Sanchez F., *« Square Pulse Switchable Operations in L-band Fiber Ring Laser »*. Romanian Journal of Physics. 65. 501. (2020).

8. Nady A., Semaan G., Kemel M., Salhi M., Sanchez F., *« Polarization-Color Domain Walls in Fiber Ring Lasers »*. Journal of Lightwave Technology, vol. 38, no. 24, pp. 6905-6910. (2020).

9. Meng Y., Zhang D., Semaan G., Kemel M., Nady A., Salhi M., Komarov A., Sanchez F., *« Optical domains in fiber lasers »*. Journal of Optics, 23, 035502. (2021).

10. Salhi M., Kemel M., Nady A., Semaan G., Sanchez F., *« Complex soliton patterns formation in a multi-wavelength Er-doped fiber laser »*. Journal of Physics Conference Series. 1919. 012004. (2021).

Conferences:

1. Kemel M., Ben Braham F., Komarov A., Semaan G., Salhi M., Sanchez F., *« Generation of high energy microsecond pulses from a hybrid regime of oscillation in a fiber laser »*. Journée de l'Ecole doctorale 3M 2018-Le Mans, (JED Le Mans 2018).

2. Kemel M., Ben Braham F., Komarov A., Semaan G., Salhi M., Sanchez F., *« Génération d'Impulsions Energétiques dans un Laser à Fibre Verrouillé en Phase »*. Journées Nationales d'Optique Guidée (JNOG), (OPTIQUE Toulouse 2018).

3. Kemel M., Mouchel P., Semaan G., Salhi M., Le Flohic M., Sanchez F., *« High-power limitations of graphene nanocoated optical taper saturable absorbers »*. Journée de l'Ecole doctorale 3M 2019-Brest (JED Brest 2019).

4. Kemel M., Mouchel P., Semaan G., Salhi M., Le Flohic M., Sanchez F., *« High-power Limitations of Graphene Nanocoated Optical Taper Saturable Absorbers »*. 2nd International Conference on Optics, Photonics and Lasers (OPAL'2019), Amsterdam, Netherlands, 24-26 April 2019.

5. Kemel M., Semaan G., Salhi M., Sanchez F., *« Coherence Measurement of Square-Pulses in Passively Mode-Locked Fiber Laser »*. 21st International Conference on Transparent Optical Networks (ICTON 2019), Angers, France, 9-13 July 2019. Invited conference.

6. Kemel M., Salhi M., Ciret C., Semaan G., Nady A., Sanchez F., *« Characterization of square-pulses in passively mode-locked fiber laser (Dissipative soliton resonance) »*. 9th EPS-QEOD Europhoton Conference (Europhoton 2020). Virtual conference, 30 August- 4 September 2020.

7. Kemel M., Salhi M., Ciret C., Semaan G., Nady A., Sanchez F., *« Coherence study of DSR-like pulses in passively mode-locked fiber lasers »*. Conference on Lasers and Electro-Optics Europe and European Quantum Electronics Conference, (CLEO-Europe/EQEC 2021). Virtual conference, 21-25 June 2021.

8. Salhi M., Semaan G., Kemel M., Niang A., and Sanchez F., *« Verrouillage de modes harmonique en régime de résonance des solitons dissipatifs (DSR) dans les lasers à fibre dopée erbium »*, TELECOM'2019 & 11èmes JFMMA, Saïda, Maroc, 12-14 Juin 2019.

9. Semaan G., Meng Y., Kemel M., Salhi M., Komarov A., Sanchez F., *« Color domains in passively mode-locked fiber laser »*. Advanced Solid-State Lasers ASSL 2019, Vienna Austria, 29 September – 3 October 2019.

10. Mouchel P., Kemel M., Semaan G., Salhi M., Le Flohic M., Sanchez F., *« High-Power Limitations of Graphene Nanocoated Optical Taper Saturable Absorbers »*. Conference on Lasers and Electro-Optics Europe and European Quantum Electronics Conference (CLEO-Europe/EQEC 2019), Munich, Germany, 23-27 June 2019.

11. Semaan G., Komarov A., Kemel M., Nady A., Salhi M., Sanchez F., *« Generation of staircase pulses in fiber lasers »*. International Conference on Optics, Photonics and Lasers (OPAL'2020), 21-23 October 2020.

12. Nady A., Kemel M., Semaan G., Salhi M., Sanchez F., *« MultiState Solitons in Multi Wavelength Er-Doped Fiber Laser »*. International Conference on Transparent Optical Networks (ICTON 2020). Virtual conference, 19-23 July 2020. Invited conference.

13. Sanchez F., Kemel M., Nady A., Semaan G., Salhi M., and Komarov A., *« On the coherence of dissipative soliton resonance square pulses ».* Internationnal Workshop on Fiber Lasers, Novosibirsk, Russia, virtual conference, 20-24 September 2020. Invited conference.

14. Salhi M., Kemel M., Nady A., Semaan G., and Sanchez F., *« Complex soliton patterns formation in a multi-wavelength Er-doped fiber laser ».* Photon 2020, virtual conference, 1 – 4 September 2020.

15. Semaan S., Komarov A., Kemel M., Nady A., Salhi M., and Sanchez F., *« Generation of staircase pulses in fiber lasers ».* Frontiers in Optics 2020, virtual conference, 13 – 17 September 2020.

16. Nady A., Kemel M., Semaan G., Salhi M., Sanchez F., *« Polarization-domain-wall in a dual-color mode-locked fiber laser »*. Europhoton 2020, Virtual conference, 30 August – 4 September 2020.

17. Semaan S., Nady A., Kemel M., Salhi M., and Sanchez F., « Square pulse switched operations in long L-band fiber laser », Advanced Photonics Congress, Maastricht, Netherlands, 24 – 28 July 2022.

UNIVERSITE MATIERE BRETAGNE MOLECULES LOIRE ET MATERIAUX

université angers

Titre : Etude d'impulsions rectangulaires dans une cavité laser à fibre co-dopée Er : Yb

Mots clés : Résonance de solitons dissipatifs, Interféromètre de Mach-Zehnder, dispersion de la vitesse de groupe, parois de domaines en longueur d'onde, parois de domaines en polarisation.

Résumé : Dans ce manuscrit, je présente mon étude expérimentale de différents types d'impulsions rectangulaires générées dans une cavité laser à fibre co-dopée à l'Erbium et à l'Ytterbium.

En premier lieu, j'étudie les impulsions rectangulaires dans la configuration laser à résonance de solitons dissipatifs. Je caractérise leur cohérence temporelle en utilisant deux méthodes différentes. La première est basée sur l'interféromètre de Mach-Zehnder et la deuxième sur l'effet de la dispersion de la vitesse de groupe. Dans cette étude, je montre que le type d'impulsions rectangulaires étudiées n'est pas automatiquement de nature DSR même si ces impulsions remplissent la plupart des critères du DSR.

Une autre étude est consacrée à la génération d'un regime laser à trois longueurs d'onde correspondant à différentes impulsions rectangulaires, qui coexistent dans la cavité laser. Le regime de fonctionnement est associé aux parois de domaines en longueur d'ondes.

Pour finir, je présente des impulsions réctangulaires qui sont à la fois des parois de domaines en longueur d'onde et en polarisation. En effet, nous montrons une émission laser de deux longueurs d'onde bien séparées et chacune de ces deux longueurs d'onde est associé à un état de polarisation different.

Title : Study of rectangular pulses in Er :Yb co-doped fiber laser

Keywords : Dissipative soliton resonance, Mach-Zehnder interferometer, group velocity dispersion, color domain wall, polarization domain wall.

Abstract : In this manuscript, I present my experimental investigation of different types of rectangular-shaped pulses generated in Erbium :Ytterbium co-doped fiber laser cavity.

First of all, I study rectangular pulses in the dissipative soliton resonance laser configuration. I characterize their temporal coherence using two different methods, the first is based on Mach-Zehnder interferometer (MZI) and the second one on the effect of the group velocity dispersion. With this study I show that the type of the generated rectangular pulses are not automatically of DSR type even if they fulfill most of the DSR characteristics.

Another study is devoted to three-wavelength generation corresponding to different rectangular domain pulses, which coexist in the laser cavity. The operating regime is associated with color domain wall.

Finally, I present rectangular pulses which are simultanuously polarization and color domain wall. Indeed, a dual wavelength laser emission is shown to be color domain, and each color domain is associated with a different polarization state.